

Technische Universität München

Fakultät für Luftfahrt, Raumfahrt und Geodäsie

Lehrstuhl für Astronomische und Physikalische Geodäsie

Enhanced methodologies of least-squares collocation for the realization of height systems

Martin Lothar Willberg

Vollständiger Abdruck der von der Fakultät für Luftfahrt, Raumfahrt und Geodäsie der Technischen Universität München zur Erlangung des akademischen Grades eines

Doktor-Ingenieurs (Dr.-Ing.)

genehmigten Dissertation.

Vorsitzender: Prof. Dr.-Ing. habil. Thomas Wunderlich

Prüfer der Dissertation: 1. Prof. Dr.techn. Roland Pail
2. apl. Prof. Dr.-Ing. Michael Schmidt
3. Assoc. Prof. Dr. Jonas Ågren

Die Dissertation wurde am 30.07.2020 bei der Technischen Universität München eingereicht und durch die Fakultät für Luftfahrt, Raumfahrt und Geodäsie am 11.09.2020 angenommen.

Zusammenfassung

Ein globales physikalisches Referenzsystem ist essentiell, um dynamische Erdprozesse, wie Meeresspiegelvariationen oder Massenbewegungen zu verstehen und zuverlässig zu modellieren. Für die entsprechende Realisierung in einem Internationalen Höhenreferenzrahmen ("International Height Reference Frame", IHRF) müssen dafür zunächst global verteilte Referenzstationen definiert werden. Anschließend können deren Potentialwerte oder physikalische Höhen durch regionale Schwerefeldmodellierung mit hoher Genauigkeit bestimmt werden. Diese Modellierung, eine Kombination von global konsistenten Satelliten- oder Schwerefeldmodellen mit lokalen Gravimetriemessungen, wird aktuell von mehreren Arbeitsgruppen der "International Association of Geodesy" (IAG) vorangetrieben. Diese Dissertation präsentiert die "Residual Least-Squares Collocation" (RLSC) als eine neue Methode der regionalen Schwerefeldmodellierung und evaluiert deren Vorteile für die Berechnung von Schwerefeldfunktionalen an Referenzstationen des IHRFs.

Die RLSC ist eine Erweiterung der klassischen "Least-Squares Collocation" (LSC) und enthält zwei essenzielle Veränderungen: Erstens verwendet die RLSC per Definition nur Residuen eines "remove-compute-restore" Ansatzes und nutzt dabei individuelle Fehlerkovarianzmatrizen für die Beschreibung aller Inputgrößen. Zweitens ist die RLSC in der Lage, die volle Varianz- und Kovarianzinformation eines hochauflösenden, globalen Schwerefeldmodells zu nutzen, um das anisotrope und ortsabhängige Schwerefeld der Erde zu modellieren. Beide Veränderungen führen zu einer realistischeren Genauigkeitsangabe der Ausgabefunktionale, was diese Dissertation an einer synthetischen Testumgebung und einer Kombination von Schwerefelddaten aus Satellitenmissionen, terrestrischen und flugzeuggetragenen Messungen demonstriert. Zusätzlich wird die stochastische Modellierung dieser Dissertation noch durch die Vermeidung einer üblichen Vereinfachung in der flugzeugbasierten Gravimetrie verbessert: Zum ersten Mal werden Korrelationen eines Tiefpassfilters nach Gauß zur Beseitigung von hochfrequentem Rauschen direkt in eine LSC-basierte Berechnung eingebaut. Diese Ansätze zur Verbesserung der Genauigkeitsangabe können einen wichtigen Vorteil für die Definition eines Internationalen Höhenreferenzsystems ("International Height Reference System", IHRS) darstellen. Aufgrund der global variierenden Datenqualität und häufigen Datenrestriktionen ist es unmöglich, eine einheitliche Genauigkeit für alle Stationen des IHRFs zu erreichen. Dementsprechend sollen Potentialwerte und physikalische Höhen an den entsprechenden Referenzstationen möglichst realistische Genauigkeitsangaben erhalten.

Die Ergebnisse der RLSC werden im Rahmen einer internationalen Arbeitsgruppe, des sogenannten 1 cm Geoid-Experiments, einem Vergleichstest mit 14 teilnehmenden Gruppen, validiert. In

den Rocky Mountains in Colorado zeigen Höhenanomalien der RLSC eine sehr gute Übereinstimmung mit dem Mittelwert aller Lösungen, was die hohe Leistungsfähigkeit und die Stabilität der vorgestellten Methode unter den anspruchsvollen Bedingungen einer Hochgebirgsregion demonstriert. Diese Dissertation analysiert und quantifiziert die verbleibenden Fehler des 1 cm Geoid-Experiments, die sich zum Beispiel aus der Qualität der topographischen Reduktion, dem Effekt der relativen Gewichtung zwischen unterschiedlichen Datensätzen oder systematischen Fehlern in den Inputbeobachtungen ergeben. Zusammenfassend stellt die RLSC damit eine hervorragende Erweiterung der LSC-Methoden dar und bietet insbesondere durch die realistischere Genauigkeitsangabe einen entscheidenden Vorteil.

Abstract

A global physical reference system is essential for modeling and understanding dynamic Earth processes like sea level variations or mass distributions. For the realization in an International Height Reference Frame (IHRF), globally distributed reference stations need to be defined. By applying regional gravity field determination, globally consistent satellite or gravity models can be combined with local gravity field measurements to calculate potential values and physical heights at reference stations of the IHRF with high accuracy, as is currently planned by working groups of the International Association of Geodesy (IAG). This dissertation derives 'Residual Least-Squares Collocation' (RLSC) as a new method for regional gravity field determination, and evaluates its advantages for the calculation of gravity-derived quantities at IHRF reference stations. The RLSC method is an enhancement of Least-Squares Collocation (LSC), which includes two main modifications. First, RLSC uses by definition only residuals from a remove-compute-restore approach, and applies individual error covariance matrices for every input quantity. Second, RLSC is able to include full variance-covariance information of a high-resolution global gravity field model that allows an anisotropic and location-dependent modeling of the Earth's gravity field. Both adaptations lead to a more realistic accuracy estimation of the output quantities, which this work presents for a synthetic test case and a combination of satellite, terrestrial and airborne gravity information. Additionally, stochastic modeling in this thesis is improved by avoiding a common simplification in airborne gravimetry. For the first time, the correlations from a Gaussian low-pass filter to remove high-frequency noise are considered directly in a LSC-based calculation method. These aspects of improved accuracy estimation can provide an important benefit for the definition of the International Height Reference System (IHRF). Due to globally varying gravity data quality and common data restrictions, it is impossible to reach homogeneous accuracies for all IHRF stations. Accordingly, potential values and physical heights at IHRF stations should be accompanied with realistic accuracy estimates. Within an international IAG working group, the RLSC results are validated in the frame of the 1 cm geoid experiment, a regional gravity field inter-comparison exercise with 14 participating groups. In the Rocky Mountains of Colorado, height anomalies from RLSC show a very good agreement with the mean value of all solutions, which demonstrates the robustness and very good performance of RLSC in the challenging scenario of a mountainous region. This thesis analyzes and quantifies the remaining errors in the 1 cm geoid experiment, which result, for example, from the quality of topographic reductions, the effect of relative weighting among different data sets and systematic errors in the observations. All in all, RLSC is an excellent addition to already existing LSC methods, and provides a main advantage by giving more realistic accuracy estimates.

Contents

Abbreviations	VIII
1 Preamble	1
1.1 Motivation and scope	1
1.2 Structure and research questions	4
2 Gravity field and height systems	11
2.1 Global gravity field determination	11
2.2 Heights and height systems	13
2.3 International Height Reference System	16
2.4 Regional gravity field determination	17
2.5 Evaluation, summary and research questions	21
3 Residual least-squares collocation	23
3.1 Introduction to RLSC	23
3.2 Covariance functions in RLSC	26
3.3 Application of covariance functions	28
3.4 Evaluation, summary and research questions	30
4 The 1 cm geoid experiment	33
4.1 IAG working group 2.2.2	33
4.2 Application of low-pass filters in airborne gravimetry	35
4.3 Validation of RLSC in Colorado	35
4.4 Comparisons to a mean reference	37
4.5 Quality assessment from GSVS17 measurements	39
4.6 Co-author publication: <i>Liu et al. (2020b)</i>	40
4.7 Co-author publication: <i>Wang et al. (in review)</i>	41
4.8 Evaluation, summary and research questions	43
5 Discussion	45
5.1 Future aspects of the 1 cm geoid experiment	45
5.2 RLSC for the calculation of IHRF stations	46
5.3 The gravity models XGM2019e and EGM2020	48
5.4 Improvement of the GRAV-D processing	49

6 Conclusions and outlook	51
Bibliography	60
Acknowledgments	61
A Appendix	63
P.1 Publication I	63
P.2 Publication II	73
P.3 Publication III	77
P.4 Publication IV	99

Abbreviations

DGFI	'Deutsches Geodätisches Forschungsinstitut'; German Geodetic Research Institute
dV EII Earth2014	Model of the topography-induced gravitational potential, derived from Earth2014, an 1 arc-minute global shape, topography, bedrock and ice model
ECF	Empirical Covariance Function
EGM2008	Earth Gravitational Model 2008
EGM2020	Earth Gravitational Model 2020
ERTM2160	Earth Residual Terrain Modelled-gravity field with the spatial scales equivalent to spherical-harmonic coefficients up to degree 2160 removed
EVRS	European Vertical Reference System
GGM	Global Geopotential Model or Global Gravity field Model
GGOS	Global Geodetic Observing System
GGRF	Global Geodetic Reference Frame
GNSS	Global Navigation Satellite System
GOCE	Gravity field and steady-state Ocean Circulation Explorer
GOCO05C	Combined gravity model of GOCO group (version 5)
GOCO05S	Satellite-only model of GOCO group (version 5)
GOCO06S	Satellite-only model of GOCO group (version 6)
GRACE	Gravity Recovery And Climate Experiment
GRAV-D	Gravity for the Redefinition of the American Vertical Datum
GRS80	Geodetic Reference System 1980
GSVS17	Geoid Slope Validation Survey 2017
HSU	Height System Unification
IAG	International Association of Geodesy
IAPG	Institute of Astronomical and Physical Geodesy
IASPEI	International Association of Seismology and Physics of the Earth's Interior
IHRF	International Height Reference Frame
IHRS	International Height Reference System
ITRF	International Terrestrial Reference Frame

ITRS	International Terrestrial Reference System
JWG	Joint Working Group
LSC	Least-Squares Collocation
MCF	Model Covariance Function
MDT	Mean Dynamic ocean Topography
NAVD88	North American Vertical Datum of 1988
NGA	National Geospatial-Intelligence Agency
NGS	National Geodetic Survey
RCR	Remove-Compute-Restore
RLSC	Residual Least-Squares Collocation
RMS	Root Mean Square
RSPG	Reference Systems in Physical Geodesy
SD	Standard Deviation
SH	Spherical Harmonic
SHS	Spherical Harmonic Synthesis
SRBF	Spherical Radial Basis Functions
XGM2016	eXperimental Gravity field Model 2016
XGM2018	eXperimental Gravity field Model 2018
XGM2019	eXperimental Gravity field Model 2019
XGM2019e	eXperimental Gravity field Model 2019 extended with topographic information

Chapter 1

Preamble

1.1 Motivation and scope

The International Terrestrial Reference System (ITRS, *Petit & Luzum, 2010*) defines a global, unified reference system for geometric measurements. It is realized by reference stations around the world and fulfills the main criteria of a geodetic reference frame: (1) it is consistent and reliable around the world, (2) it provides long-term stability, and (3) its millimeter accuracy is smaller than the magnitude of most effects, which are described with it (*Sánchez, 2012*). While this International Terrestrial Reference Frame (ITRF) enables the monitoring of the System Earth geometrically, a corresponding physical reference frame is still missing. However, a global physical reference frame is essential to understand and to model dynamic Earth processes (e.g., sea level variations, mass redistributions). Furthermore, it is needed to define physical heights accurately and in a globally consistent way (*Gruber et al., 2014*). Accordingly, the definition of an International Height Reference System (IHRS, *Ihde et al., 2017*) and the establishment of the International Height Reference Frame (IHRF), as an integral part of a Global Geodetic Reference Frame (GGRF), have been main objectives of the International Association of Geodesy (IAG) for several years now.

In 2010, the Global Geodetic Observing System (GGOS, *Kutterer, 2012*) Theme 1 'Unified Height System' was set up in order to combine existing activities and initiatives with a similar purpose (*Sánchez, 2012*). Since that time, the issue of a unified height system is permanently addressed in different working groups of IAG. Within the IAG period from 2015 to 2019, for example, 'the 1 cm geoid experiment' started as Joint Working Group (JWG) 2.2.2. It validates and compares different regional gravity calculation methods, which might be used for the calculation of IHRF stations at the end, and its main results are summarized in *Wang et al.* (in review) and *Sánchez et al.* (in review). The latest version of the IHRS definition and its current status are given in *Ihde et al. (2017)* and *Sánchez & Sideris (2017)*. Earlier publications about a unified height system or physical reference frame are numerous, but often using different terms: 'a world vertical network' is proposed by *Colombo (1980)*, a 'vertical datum definition' by *Rummel & Teunissen (1988)*, a 'global vertical datum' by *Balasubramania (1994)*, a 'global unification of height systems' by *Rummel (2001)* and a 'global unified height reference system' by *Ihde & Sánchez (2005)*.

Huge improvements towards the IHRF definition have been brought by gravity satellite missions, mainly GRACE (Gravity Recovery And Climate Experiment, *Tapley et al.* 2004) and GOCE (Gravity field and steady-state Ocean Circulation Explorer, *Drinkwater et al.* 2003). They provide the static gravity field of the Earth with an accuracy of 1-2 cm at spatial scales of 100 km and longer (*Brockmann et al.*, 2014; *Gruber et al.*, 2012). Accordingly, publications within the last decade agree, that Height System Unification (HSU) will be based upon the globally consistent, long-wavelength part of the gravity field, which is derived from satellite missions (*Rülke et al.*, 2012; *Rummel*, 2012; *Gerlach et al.*, 2013; *Gruber et al.*, 2014). However, gravity signals with shorter wavelengths cannot be observed by satellite missions due to the gravity signal attenuation with the satellite's distance from the Earth's surface, and have to be added from different sources. In most cases, gravity observations from terrestrial, airborne and shipborne campaigns, satellite altimetry and topographic forward modeling (*Rexer et al.*, 2016; *Hirt & Rexer*, 2015) are combined, according to availability, in order to calculate the gravity signal beyond satellite resolution (e.g., *Pavlis et al.* 2012). High-resolution Global Geopotential Models (GGM) combine available gravity data sources around the world and can be synthesized at arbitrary point positions in terms of different gravity functionals. Accordingly, a high-resolution GGM is the easiest possibility to calculate gravity functionals at an IHRF station, but its accuracy depends on the availability and quality of the corresponding gravity data within the GGM. In areas with sparse data distribution, the omission error of the high-resolution GGM could increase significantly, and correspondingly propagates to the IHRF. Furthermore, the reliability of high-resolution GGMs is decreased due to the often unknown quality of the models and the restricted access to the original gravity data bases. Accordingly, *Ihde et al.* (2017) prefer to realize IHRF stations by a satellite-only GGM, which is refined regionally by satellite altimetry and regional gravity observations. This challenge of optimally combining different data sets for a local territory is an often discussed topic in the geodetic community, and generally called regional gravity field determination.

A variety of different methods can be applied for regional gravity field determination, from which this work here focuses mainly on Least-Squares Collocation (LSC). LSC is a statistical least-squares optimization. Accordingly, it is the only method that provides a statistical minimization of residuals by applying a parameter estimation with covariance matrices (*Tscherning*, 2015). Additionally, it is selected in this thesis for its advanced stochastic modeling and its ability to calculate a full covariance information of the output functional. In general, LSC is one of the most common and oldest methods for regional gravity field determination. It was first mentioned in *Krarup* (1969), and then further developed in *Moritz* (1980), which provides one of the most detailed and consistent LSC descriptions. However, the description in *Moritz* (1980) was almost 30 years before the first calculation of a high-resolution GGM and is not intended for their inclusion into LSC. Furthermore, it uses isotropic covariance matrices to describe a non-isotropic gravity field, which cannot yield optimal results (*Tscherning*, 1999).

This work develops Residual Least-Squares Collocation (RLSC) as a new method for regional gravity field determination. It describes the definition and application of RLSC, which adapts the

LSC concept by *Moritz* (1980) in such a way, that it allows the consistent inclusion of high-resolution GGMs and an extended error formulation. In comparison to previous approaches of LSC (e.g., *Forsberg & Tscherning* 1981; *Moritz* 1980; *Hofmann-Wellenhopf & Moritz* 2006; *Rieser* 2015), this residual least-squares collocation brings the following benefits:

- 1) Inclusion of non-isotropic and non-homogeneous covariance matrices, which describe the accuracy information of a high-resolution GGM and allow a more realistic modeling of the Earth's gravity field.
- 2) The mathematical formalism is expanded to a consistent inclusion of a remove-compute-restore concept, which describes every input quantity with corresponding accuracy information and uses only error covariance matrices.
- 3) The method is able to provide a realistic formal error estimate, since it includes all related error components.

It should be noted that some LSC approaches already introduce accuracy information from a satellite-only model (e.g., *Haagmans & van Gelderen* 1991; *Pail et al.* 2010; *Sansò & Sideris* 2013), and therefore also include all related error components (item 3) in a different realization than RLSC. *Ihde et al.* (2017) mentioned the unknown reliability of high-resolution GGMs as the main reason to neglect them for the calculation of IHRF stations, and use satellite-only GGMs instead. However, with the XGM models (e.g., XGM2016, *Pail et al.*, 2018) we have a combined GGM with a significantly improved error modeling. Furthermore, RLSC is able to consider quality and correlations of the XGM by including its corresponding covariance functions. Accordingly, RLSC could improve the calculation of IHRF stations, while providing a more realistic error estimation at the same time. This sets the scope of this work, when reduced to a single sentence, as the following:

The dissertation shall explain and demonstrate the advantages of residual least-squares collocation for regional gravity field modeling, and how these are beneficial for the establishment of an IHRS.

Therefore, the work envisions to satisfy the following main objectives:

- O1 - To understand the main challenges of height system unification, and the benefits that are provided by a global high-resolution GGM.
- O2 - To derive the mathematical concept for RLSC, to explain the reason for adapting the LSC approach by *Moritz* (1980), and to work out the differences between the two methods.
- O3 - To apply RLSC for a combination of high-resolution GGM, terrestrial and airborne gravimetry, and to verify its results by internal and external validations.

In the next section, the structure of this thesis is described in detail, whereby the contribution of different chapters is characterized and their connections outlined.

1.2 Structure and research questions

This thesis is a paper-based dissertation, which means, that the main results of this work are already published in peer-reviewed journals. Three corresponding first author publications are reprinted in Appendix A, while the original article of one co-authored publication is available as open access. Appendix A additionally includes a declaration of the own contribution for all four publications, and a respective short summary. In the following, these publications are referred to as P-I to P-IV. The scope of this work is to connect them in a scientific context and evaluate their individual and combined benefit for the geodetic community. In order to characterize the main contribution of each publication to the research objectives (Sect. 1.1), this chapter defines two research questions for each publication, which are answered in the corresponding section of this thesis. It is important to understand, that the publications are all self-contained studies. They individually consist of a problem definition, a method description, research results and a conclusion. However, in the combined analysis of this work, the publications are also part of a mainly linear structure, which can be interpreted as theory (P-I, P-II), methodology (P-III) and application (P-IV). This structure is also represented in the chapters of this work, whereby each publication is assigned to one main chapter (Fig. 1.1). In the following, the content of the different chapters is described first, then the contribution of each publication is explained together with the corresponding research questions.

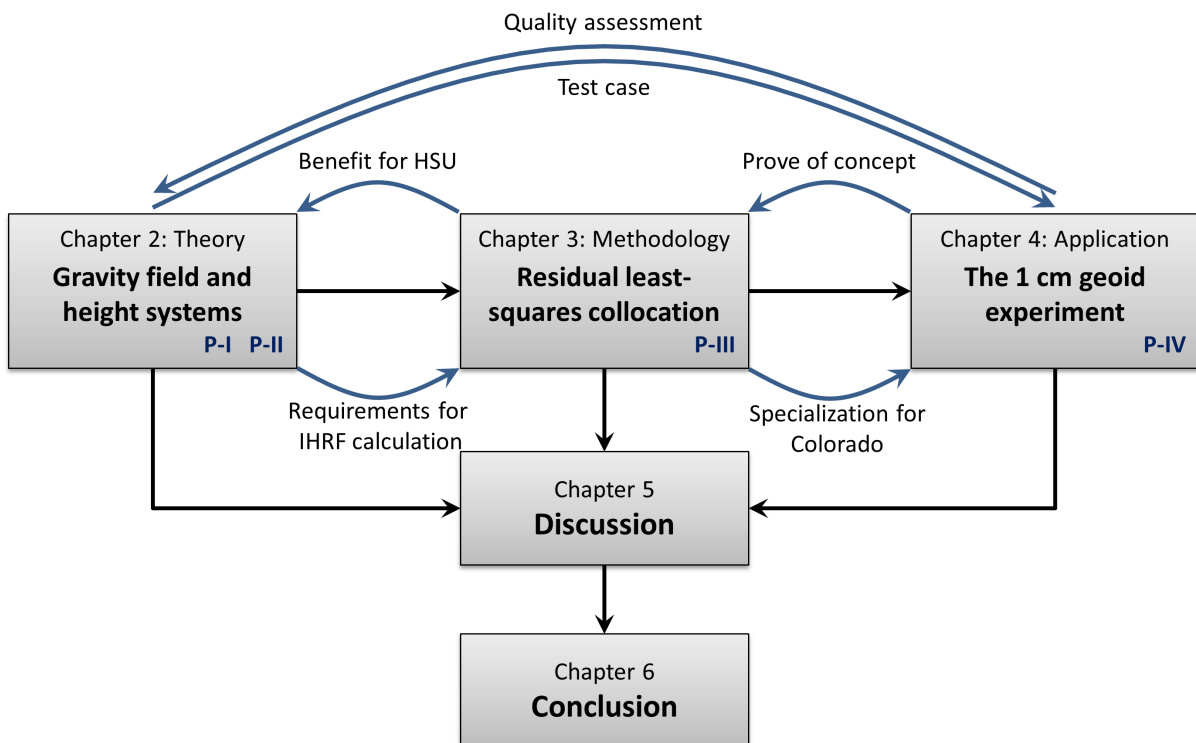


Fig. 1.1 – Structure of this cumulative thesis, which marks the connection between different chapters in black color, and the connection between the publications P-I to P-IV by blue arrows.

Chap. 2 ('Gravity field and height systems') describes the theoretic background of this work by providing basic principles of gravity field modeling, potential theory and height systems. It derives the mathematical background for spherical harmonic synthesis from the formulation by *Hofmann-Wellenhof & Moritz* (2006), which provides the possibility to synthesize arbitrary gravity functionals from a GGM. The chapter explains different heights and height systems as well as the IHRS definition. Thereby, the IHRS is discussed in more detail than in Sect. 1.1 by setting requirements for its introduction and presenting its current status. Finally, the benefits of different gravity data sets are explained, their possibilities for combination are explained and different approaches for regional gravity field modeling are outlined. In summary, Chap. 2 defines the problem of different height systems and the resulting challenges for a HSU. Regarding the overall structure (Fig. 1.1), Chap. 2 sets the requirements for the IHRF calculation, which will be addressed by RLSC (Chap. 3). Furthermore, the work towards HSU leads to the establishment of 'the 1 cm geoid experiment' as test case for regional gravity field modeling (Chap. 4).

Accordingly, in Chap. 3 ('Residual least-squares collocation') the basics of RLSC are explained and its differences to other LSC approaches are demonstrated. Although it should be noted that the detailed derivation of RLSC is presented in P-III, Chap. 3 explains the corresponding main advantages in detail. Furthermore, it focuses on the calculation of covariance functions, which are the key factor for collocation. Thereby, Chap. 3 explains the differences in covariance functions between P-III and P-IV, as they use different reference surfaces. RLSC fits into the overall framework of this thesis (Fig. 1.1), as it provides several benefits for the challenges of HSU (Chap. 2) when compared to other methods for regional gravity field determination. Chap. 3 describes the methodology of RLSC, which is applied in Chap. 4 for a case study in Colorado.

Chap. 4 ('The 1 cm geoid experiment') describes the background and the goals of JWG 2.2.2 and the so-called 'the 1 cm geoid experiment'. Furthermore, it explains the challenge of using noisy airborne gravity observations. Comparisons within 'the 1 cm geoid experiment' validate the RLSC results, and demonstrate that RLSC is able to provide an excellent and robust solution in a challenging test case. All submitted solutions are evaluated for their error contribution, which includes, for example, inconsistencies and relative weighting between different data sets, measurement errors, and method-specific differences among various approaches. Advantages and disadvantages of different validation methods are analyzed in detail, whereby the work focuses on the comparison of individual approaches to a joint mean value. Additionally, high-quality measurements from GNSS (Global Navigation Satellite System) and spirit leveling are considered for the discussion. Finally, Chap. 4 highlights the author's contribution to other publications in the context of 'the 1 cm geoid experiment'. The application of RLSC in 'the 1 cm geoid experiment' proves the concept that was derived in Chap. 3. Furthermore, Chap. 4 provides a quality assessment of regional gravity field determination that can support the introduction of an IHRS (Chap. 2).

A combined analysis of all four publications and the previous chapters follows in Chap. 5. It focuses on the continuation of 'the 1 cm geoid experiment', and summarizes the benefits of RLSC for HSU. Furthermore, it discusses gravity data and GGM improvements as method-independent

approaches for the enhancement of regional gravity field determination. Finally, a conclusion and an outlook are presented in Chap. 6.

Two research questions are defined for each of the publications in order to clarify their main contribution to the research objectives (O1-O3). The answers to these research questions are given in detail in the corresponding chapter and are furthermore summarized at the end of each chapter. The publications P-I and P-II have some overlap in terms of their contribution, since both of them apply GNSS/leveling, explain the role of GGMs in a HSU and give insights about the quality of GGMs. Nevertheless, their research questions are separated to define a main contribution to each publication, while the discussion in Sect. 2.5 combines the corresponding answers. An additional summary about each individual publications is included at the end of this chapter, while the corresponding abstracts are also separately presented in Appendix A.

P-I focuses on challenges of HSU in general, and gives a concrete example for the mainland of Greece and its islands. In it, the problem of different height systems and reference surfaces is explained in detail. It evaluates three different geoid models for their capability in terms of HSU, whereby it sets a special focus on the omission error and a quality assessment. The research questions for P-I are:

Q1 - What is the benefit of introducing a unified height system based on a GGM?

Q2 - How can the omission error be handled in HSU, and why is it an essential limitation in the process?

P-II contains a quality assessment of various GGMs, which is an important evaluation for all sections of this work. It analyzes signal and error content for a combination of high-resolution GGMs with topographic gravity information, and gives geoid accuracies that can be reached by this. In the frame of this comparison, P-II particularly highlights the benefit of the GOCE mission. The research questions of P-II are defined as:

Q3 - How is GNSS/leveling used for the evaluation of GGMs?

Q4 - What accuracies can be reached by regional geoid determination from high-resolution GGMs that are combined with topography-induced gravity information?

P-III formulates the concept for RLSC as an adaption to the LSC formulation by *Moritz* (1980). It explains how covariance matrices from high-resolution GGMs can be exploited in RLSC, and why this formulation, which uses accuracy information for every input quantity, is beneficial. P-III closely links and compares the RLSC approach to other formulations of LSC (e.g., *Forsberg & Tscherning* 1981; *Haagmans & van Gelderen* 1991; *Pail et al.* 2010; *Sansò & Sideris* 2013; *Rieser* 2015). Lastly, P-III uses a synthetic closed loop environment to quantify the differences between LSC and RLSC, and shall answer the following research questions:

Q5 - How is the RLSC method derived mathematically?

Q6 - What is the benefit of RLSC and what are the differences to other LSC formulations?

P-IV applies RLSC for a combination of satellite, terrestrial and airborne gravimetry in order to calculate the height anomaly in Colorado and New Mexico. For the validation of these calculations, it compares the height anomaly with 13 independently calculated results from the same area, which are available from 'the 1 cm geoid experiment'. P-IV also derives a concept for the handling of noisy airborne gravity observations in RLSC, and answers the following research questions:

Q7 - Why are low-pass filters applied in airborne gravimetry and how can the filter process be included into the RLSC formalism?

Q8 - What is the performance of RLSC in comparison to other independent solutions from the 1 cm geoid experiment?

The next two pages give a general overview of the publications this work is based on (P-I to P-IV). They include title, contributors and publisher for each of the publications, as well as a short summary of the corresponding content.

P-I **Analysis of GOCE Omission Error and its Contribution to Vertical Datum
Offsets in Greece and its Islands**

Martin Willberg, Thomas Gruber, Georgios S. Vergos
in: International Association of Geodesy Symposia 148

This publication analyzes different geoid models in Greece and its islands for their signal content, their omission error, and their applicability for a height system unification. The three evaluated geoid models are a satellite-only GGM (GOCO05S) up to spherical harmonic degree 200, an extended satellite model as combination of GOCO05S, EGM08 and topography-induced gravity information, and a local geoid model. The study compares these geoid models with available GNSS/leveling observations, and concludes that the globally unified GOCO05S is not sufficient for a height system unification due to the omission error. The other two models show comparable results in the error analysis. Our findings in the studied test area indicate, that the high-resolution GGM (with topographic corrections) performs almost as well as a local geoid model for describing the regional characteristics of the Earth's gravity field.

P-II **Signal and Error Assessment of GOCE-based High Resolution Gravity Field
Models**

Thomas Gruber, Martin Willberg
in: Journal of Geodetic Science

In this publication, the quality of high-resolution GGMs is assessed in terms of the improvement from GOCE, the signal content and the error level. Therefore, six GGMs are analyzed for their signal degree variances and furthermore compared to geoid heights from GNSS/leveling. The terrestrial data quality that is incorporated in the high-resolution GGMs is of significant importance for their overall performance. In a comparison of recent models to EGM2008, approximately 80% of the improvement are traced back to the GOCE mission, while the remaining 20% result from terrestrial data improvements. The calculation of geoid height differences and geoid slope differences are tools to evaluate GGMs, but also to draw conclusions about the quality of leveling observations and GNSS heights. Furthermore, they allow the analysis of possible error sources or even systematic errors in the data.

P-III **Residual least-squares collocation: use of covariance matrices from high-resolution global geopotential models**

Martin Willberg, Philipp Zingerle, Roland Pail

in: Journal of Geodesy

This publication presents an enhanced formulation of least-squares collocation. This residual least-squares collocation uses covariance matrices from a high-resolution global geopotential model (XGM2016) in order to describe the gravity field as anisotropic and location-dependent quantity. This is advantageous compared to the two customary methods, which derive covariance matrices either from signal degree variances or empirical covariance fitting. Furthermore, RLSC (1) implicitly includes a remove-compute-restore concept, (2) models input quantities with error covariance matrices instead of signal covariance matrices, and (3) is able to derive realistic error estimates since it involves all components in terms of the stochastic modeling. In a synthetic closed loop environment the method is tested and compared to a standard LSC approach. Thereby, RLSC demonstrates better performance in general with particular advantages in areas with sparse terrestrial gravity observations. Furthermore, RLSC provides improved uncertainty estimates.

P-IV **Integration of airborne gravimetry data filtering into residual least-squares collocation - example from the 1 cm geoid experiment**

Martin Willberg, Philipp Zingerle, Roland Pail

in: Journal of Geodesy

This paper applies RLSC to calculate height anomalies within the 1 cm geoid experiment, a regional geoid modeling inter-comparison exercise. This allows an evaluation of RLSC with 13 independent solutions from various regional modeling approaches. The comparison indicates, that the result from RLSC is among the best solutions and even shows the smallest standard deviation to a joint mean value. Furthermore, this publication establishes a method to include a low-pass filter for airborne gravimetry consistently into the functional and stochastic model of RLSC, which further improves accuracy estimates by considering the correlations from the filter process. We demonstrate the necessity to remove this high-frequency noise from the airborne gravity observations in this area, and realize it with a Gaussian low-pass filter, which is applied to both, observations and covariance matrices.

Chapter 2

Gravity field and height systems

2.1 Global gravity field determination

This section gives fundamentals of potential theory and spherical harmonic series expansion according to *Hofmann-Wellenhof & Moritz (2006)*, and can be found in much greater detail there, since the presented work only focuses on selected aspects. The Earth's gravity potential W is a sum of the gravitational potential V and the centrifugal potential Φ

$$W = V + \Phi . \quad (2.1)$$

It can be approximated with the normal gravity potential U , which is derived from the definition of a reference ellipsoid, e.g., the Geodetic Reference System 1980 (GRS80, *Moritz 2000*). Accordingly, the difference

$$T = W - U , \quad (2.2)$$

leaves a relatively small residual part and is denoted as disturbing potential or anomalous potential. In order to describe the disturbing potential T with a (solid) Spherical Harmonic (SH) expansion, we start with the general expression for surface spherical harmonics $Y_n(\vartheta, \lambda)$ in spherical coordinates (radius r , geocentric co-latitude ϑ , and geocentric longitude λ)

$$Y_n(\vartheta, \lambda) = \sum_{m=0}^n \left[\left(a_{nm} \cos m\lambda + b_{nm} \sin m\lambda \right) P_{nm}(\cos \vartheta) \right] , \quad (2.3)$$

where a_{nm} and b_{nm} are arbitrary constants, n is the SH degree, m the SH order, and P_{nm} the Legendre function. According to Laplace's equation the disturbing potential T is a harmonic func-

tion outside the Earth's masses. Therefore, it can be described with (Laplace's) surface spherical harmonics as (Torge, 2003)

$$T_n(\vartheta, \lambda) = \frac{GM}{R} \sum_{m=0}^n \left[\left(\Delta C_{nm} \cos m\lambda + \Delta S_{nm} \sin m\lambda \right) P_{nm}(\cos \vartheta) \right], \quad (2.4)$$

where G is the gravitational constant, M the Earth's total mass and R the spherical harmonic reference radius. R is usually defined as mean equatorial radius of the Earth. Furthermore, ΔC_{nm} and ΔS_{nm} are residual spherical harmonic coefficients without the normal field of the Earth (cf. Eq. 2.2). It should be noted that Eq. 2.4 is often formulated with fully-normalized Legendre Polynomials \bar{P}_{nm} and fully normalized, residual coefficients $\Delta \bar{C}_{nm}$ and $\Delta \bar{S}_{nm}$, as this has numerical benefits (e.g., Fecher *et al.*, 2015; Rexer, 2017). The (solid) spherical harmonic series for the disturbing potential $T(r, \vartheta, \lambda)$ is

$$T(r, \vartheta, \lambda) = \sum_{n=0}^{\infty} \left(\frac{R}{r} \right)^{n+1} T_n(\vartheta, \lambda). \quad (2.5)$$

It describes the disturbing potential T at each point (r, ϑ, λ) , which is not within the Earth's masses, whereby the (fully normalized) residual spherical harmonic coefficients $\Delta \bar{C}_{nm}$ and $\Delta \bar{S}_{nm}$ are available from a GGM. Accordingly, in practice, the sum in Eq. 2.5 is not applied to infinity, but to the maximum SH degree of the GGM (e.g., described in P-IV). In this work, GGMs are in general distinguished between high-resolution GGMs and satellite-only GGMs. Thereby, high-resolution GGMs are defined to have at least a maximum SH degree of 719 (e.g., XGM2016), while satellite-only GGMs include the Earth's gravity field to approximately SH degree 200 or 300 (e.g. GOCO06S, Kvas *et al.*, 2019), which is equal to the maximum resolution of GOCE.

The process of applying a spherical harmonic series for the calculation of gravity functionals (e.g., Eq. 2.5) is called Spherical Harmonic Synthesis (SHS). It is applied for the calculation of geoid heights and the validation of GGMs in P-I and P-II (details in Sect. 2.2). Furthermore, it is used for the reduction of gravity measurements in P-III and P-IV, and, in general, for the Remove-Compute-Restore (RCR) procedure. The spherical harmonic expansion for other gravity functionals is also derived from Eq. 2.5. For the gravity anomaly Δg (in spherical approximation) and the gravity disturbance δg we have

$$\begin{aligned} \Delta g &= -\frac{\partial T}{\partial r} - \frac{2}{r} T \\ &= \frac{1}{r} \sum_{n=0}^{\infty} (n-1) \left(\frac{R}{r} \right)^{n+1} T_n(\vartheta, \lambda), \end{aligned} \quad (2.6)$$

$$\begin{aligned}\delta g &= -\frac{\partial T}{\partial r} \\ &= \frac{1}{r} \sum_{n=0}^{\infty} (n+1) \left(\frac{R}{r}\right)^{n+1} T_n(\vartheta, \lambda).\end{aligned}\quad (2.7)$$

Apart from SHS, the gravity disturbance δg and the gravity anomaly Δg can also be derived from (full) gravity measurements g by reducing the normal gravity γ

$$\Delta g = g_P - \gamma_Q, \quad (2.8)$$

$$\delta g = g_P - \gamma_P, \quad (2.9)$$

whereby the subscript of g and γ defines the point, where the normal gravity is calculated (Fig. 2.1). Eq. 2.9 is applied to calculate the gravity disturbance δg from absolute gravity measurements in P-IV.

2.2 Heights and height systems

The basic structure of potential surfaces and physical heights is presented in Fig. 2.1, and explained in accordance with *Hofmann-Wellenhof & Moritz* (2006). We define a point P_0 on the geoid, an equipotential surface with $W = W_0$ (details in P-I), and project it onto the point Q_0 on the ellipsoid by means of the ellipsoidal normal. Thereby, the ellipsoid is defined by the surface, where the normal potential U is equal to the potential W_0 in point P_0 . According to the theory of Stokes, the distance between P_0 and Q_0 is denoted geoid height N (or geoid undulation), and is calculated by

$$N = \frac{T(P_0)}{\gamma_{Q_0}}, \quad (2.10)$$

where γ_{Q_0} is the normal gravity at the ellipsoid in Q_0 . According to the theory of Molodensky (*Hofmann-Wellenhof & Moritz*, 2006), we find a similar relation for the height anomaly ζ (or quasi-geoid height)

$$\zeta = \frac{T(P)}{\gamma_Q}, \quad (2.11)$$

with P being a point on the Earth's surface, and Q the corresponding point on the telluroid with the same ellipsoidal normal (Fig. 2.1). Thereby, the telluroid is defined by the surface where the normal potential U of every point Q is equal to the gravity potential W of every point P . Furthermore, the

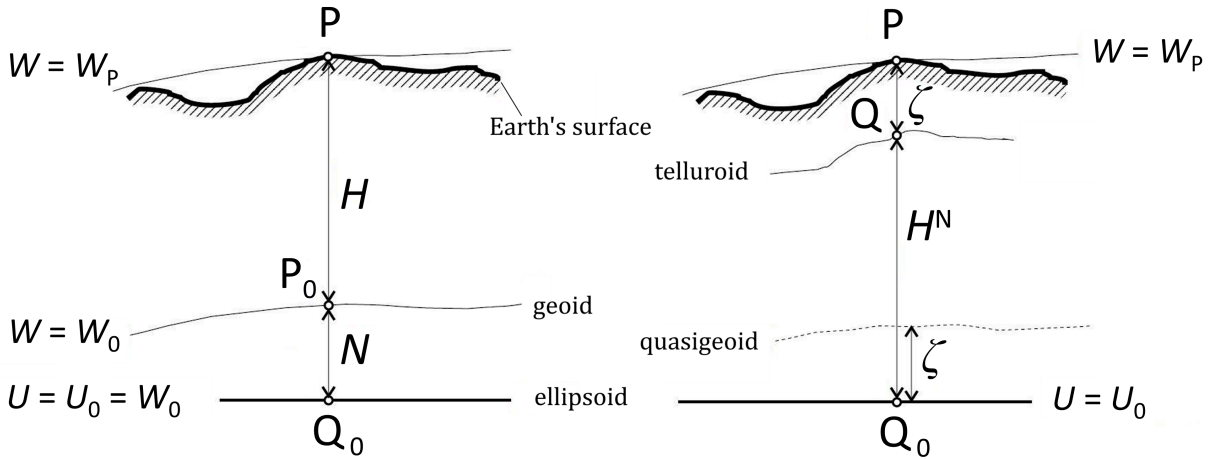


Fig. 2.1 – Overview of physical heights and potential surfaces according to the theory of Stokes (left) and the theory of Molodensky (right). Visualization is adapted from *Gerlach* (2003).

ellipsoidal height h of a point P is given as the distance between the Earth's surface and the ellipsoid. It can be written as a combination with either the geoid height N

$$h = N + H, \quad (2.12)$$

where H is the orthometric height of point P, or with the height anomaly ζ

$$h = \zeta + H^N, \quad (2.13)$$

where H^N is the normal height of point P. The orthometric height H and the normal height H^N are the two most important types of physical heights, and can be transferred by spirit leveling and gravimetry (*Heiskanen & Moritz, 1967*). Ellipsoidal heights are usually measured by GNSS (*Hofmann-Wellenhof & Moritz, 2006*). The publications P-I, P-II and P-III calculate geoid heights, while P-IV uses height anomalies according to the theory of Molodensky.

In an ideal case, all orthometric heights would refer to the true geoid, that is a global equipotential surface. However, in P-I we see that local height systems are defined by a local vertical datum, which is usually realized by a local tide gauge instead of a global equipotential surface. Additionally, there is a variety of different definitions and standards for height systems around the world (e.g., the difference between orthometric and normal heights). As a result, physical heights are often not comparable. In order to make physical heights comparable among each other, they either have to refer to the same equipotential surface, or their corresponding geoid height/height anomaly and ellipsoidal height have to be available with high accuracy (*Gruber et al., 2014*). With the introduction of an International Height Reference System it would be possible to connect physical heights to a globally consistent vertical datum, which therefore enables a height comparison and transfer (*Sánchez & Sideris, 2017; Ihde et al., 2017*). It should be noted that P-I includes more details

about various reference surfaces. Furthermore, it shows a visualization with the relation between two realizations of a local vertical datum, a respective equipotential surface, and the corresponding physical heights.

From the satellite missions GOCE and GRACE, the static part of the Earth's gravity field at spatial scales of 80-100 km is available with an accuracy of 1-2 cm (P-I; P-II; *Brockmann et al.* 2014; *Gruber et al.* 2012). Accordingly, a satellite-only GGM with this spatial resolution is able to provide a globally consistent reference surface, which should be used as a basis for HSU (P-I; P-II; *Gerlach et al.* 2013; *Gruber et al.* 2014; *Rülke et al.* 2012). However, geoid signals with smaller spatial resolution (higher SH degrees) are still missing and introduce an omission error, whose effect on HSU is explained in P-I. Therefore, HSU, with a globally consistent GGM alone, is not sufficient to reach centimeter accuracy (P-I). In high-resolution GGMs, on the other hand, the omission error is significantly reduced (P-II). However, some regions in high-resolution GGMs include only very sparse gravity data for the refinement of higher frequencies (e.g., *Pavlis et al.* 2012). Accordingly, they still include a significant omission error there (*Ihde et al.*, 2017). Additionally, inhomogeneous or faulty gravity data can result in a commission error, that might be included in a high-resolution GGM. Both errors pose a significant problem for high-accuracy applications such as the realization of an IHRF, since they would normally propagate to the frame's quality. Accordingly, *Ihde et al.* (2017) propose not to use high-resolution GGMs for HSU, but their corresponding potential is quantified nevertheless.

P-II assesses the quality of high-resolution GGMs, and quantifies their potential and suitability for HSU. The applied method is called GNSS/leveling (details in P-I and P-II). It calculates the difference between the ellipsoidal height measurements h from GNSS, and the sum of the geoid heights N from a GGM and the orthometric heights H from spirit leveling (all quantities in Eq. 2.13). The resulting difference allows an analysis of the included omission error in the GGM as well as the corresponding measurement errors. P-II gives the accuracy of a geoid model from a high-resolution GGM (with added information about the topography induced gravity) according to the gravity information that is incorporated in the GGM. In areas with very high observation density, a geoid accuracy of 1 cm might be feasible, while less good coverage reduces the performance to several centimeters or a decimeter (P-II). It should be noted that apart from the data coverage, also the terrain structure has a very high impact to the geoid accuracy. Correspondingly, P-IV indicates that geoid accuracies are worse, when the calculations are done in mountainous regions. Furthermore, the GNSS/leveling method analyzes a combination of errors from GGM, GNSS and spirit leveling. Accordingly, it is not always easy to conclude, which component contributes errors to what extent (*Gruber et al.*, 2012). In case the geoid is calculated from a high-resolution GGM only, *Gruber et al.* (2014) give an accuracy of 4 to 6 cm in well-surveyed regions, and 20 to 40 cm in sparsely surveyed regions. Although, *Sánchez & Sideris* (2017) and *Ihde et al.* (2017) take over these values in their publications, it should be noted that the values might be better depending on the terrestrial gravity data quality and the gravity signal above the resolution of the GGM.

2.3 International Height Reference System

P-I already describes the problem, which results from different vertical height systems and the corresponding advantage from HSU or the introduction of an IHRS. A more detailed description of the issue can be found in *Sánchez (2012)*; *Sánchez & Sideris (2017)* and *Ihde et al. (2015, 2017)*, which should be summarized in the following.

Geometry and gravity potential are used to characterize the Earth. Heights can describe the geometry of the Earth by an ellipsoidal height h (Fig. 2.1), but also its geopotential part (e.g., orthometric heights H in Eq. 2.12). At the moment, the definition of ellipsoidal heights has several advantages compared to the measurement of physical heights. Ellipsoidal heights are already consistent around the world, their measurement with GNSS works at high accuracy, is quick and has rather low costs. Physical heights, in contrast, are defined in local vertical systems differently around the world and their transfer could be difficult (P-I, Sect. 2.2). However, only physical heights can describe the flow of water or mass distributions on the Earth, which makes a global physical height reference system mandatory (*Ihde et al., 2017*). The topic is much discussed in literature and was already mentioned by *Rummel & Teunissen (1988)* and *Rapp & Balasubramania (1992)*. Nowadays, the realization of an IHRS is significantly simplified by the high accuracy of the static part of the Earth's gravity field, which is available from GOCE and GRACE mainly (P-II).

Based on the necessity of an IHRS introduction, the matter is constantly supported by IAG working groups for approximately a decade (details in *Ihde et al., 2017*). Furthermore, in 2015, the 'definition and realization of an International Height Reference System' was published as an IAG resolution (*Drewes et al., 2016*). It specifies the main goals in this matter, and defines the vertical reference level for the IHRS as $W_0 = 62636853.4 \text{ m}^2\text{s}^{-2}$, while the derivation of W_0 is explained in *Sánchez et al. (2016)*. The IHRS should define a global physical reference frame with high accuracy, and it should be realized with the IHRF as an equivalent to the already existing ITRF. Its reference stations should be distributed around the world, and define the gravity potential W_P that correlates to the geometric coordinates of a point P.

For the unification of already existing physical height systems, *Ihde et al. (2017)* propose three possibilities:

- 1) The common adjustment of existing leveling networks could combine neighboring countries, and is therefore only possible on the same continent. The European Vertical Reference System (EVRS) is an example for a height combination from leveling adjustment (*Ihde et al., 2002*; *Ihde & Augath, 2002*).
- 2) The unification by a combination of tide gauge observations and Mean Dynamic ocean Topography (MDT) could combine measurements at the coast. However, MDT measurements might suffer from local effects, and altimetry measurements from reduced quality close to the coast (*Rummel, 2012*).

- 3) The combination of GNSS observations with a geoid model could provide the absolute potential value W from the disturbing potential T (see Eq. 2.2). Therefore, the unification uses either a (high-resolution) GGM, or preferably the refinement of a GGM with regional gravity data.

Case 1 and 2 are restricted to certain requirements, so that only case 3 could be applied as a general case for HSU. *Ihde et al. (2017)* mention the development of strategies for the calculation of potential values at IHRF reference stations as an unsolved issue in the outlook. The newly developed residual least-squares collocation (Chap. 3, P-III) can provide significant benefits for the combination of high-resolution GGM and regional gravity data, and therefore also for the calculation of potential values W at IHRF stations. This method and its application for HSU are the main focus of this thesis.

Although, it is necessary to calculate the absolute gravity potential W for the definition of IHRF stations, the most common case for regional gravity field determination is the prediction of geoid heights or height anomalies from gravity anomalies or disturbances. Accordingly, P-III uses synthetic gravity anomalies to calculate geoid heights, and P-IV gravity disturbances to result in height anomalies. Thereby, both publications establish the required connection between ellipsoidal and physical heights (Sect. 2.2), and it should be noted that the calculation of absolute potential values W (from Eq. 2.2) and physical heights (Eq. 2.12 or 2.13) is methodically quite similar to the calculations in P-III and P-IV.

2.4 Regional gravity field determination

Data for regional gravity field determination:

Apart from the calculation of gravity functionals by SHS with GGMs (Sect. 2.1 and 2.2), there is also the possibility to combine the globally consistent satellite information with available gravity measurements and topography-induced gravity locally (e.g., around an IHRF station). This combination is necessary since different forms of gravity observations have different advantages and disadvantages:

- Satellite information, for example, is better suited for calculating the long-wavelength part of the Earth's gravity field, which is globally consistent with high accuracy (compare Sect. 2.2). However, due to the distance to the Earth's surface, satellite missions are not able to measure the gravity field at wavelengths below approximately 80-100 km. Consequently, they suffer from a significant omission error (P-I).
- Terrestrial gravity measurements can provide the short to medium-wavelength part of the Earth's gravity field, depending on their distribution. However, they might suffer from systematic effects locally, which follows from the fact that terrestrial observations are mainly

measured with relative gravimeters, were often taken several decades ago and sometimes do not contain a detailed documentation.

- Airborne gravity measurements combine advantages and disadvantages from terrestrial and satellite measurements: on the one hand, they are theoretically consistent for a local region and generally well distributed over an area. On the other hand, they might issue a bias problem for individual flight lines, and the measured gravity signal is already attenuated due to the flight height of the aircraft. Additionally, airborne gravimetry commonly requires preprocessing in order to remove high-frequency noise from the observations (P-IV).
- The very high-frequency parts of the Earth's gravity field, e.g., above the resolution of a GGM, are mainly related to the topography (e.g., *Rexer et al.* 2016). Accordingly, topographic information is often used to describe these frequencies, as other gravity sources rarely have the same resolution (see *Hirt et al.* 2019). This is especially important in mountainous areas or areas with varying topography, where the high-frequency part of the gravity field can contribute significantly to the gravity signal. However, topography-induced gravity information has to include density assumptions, which might not coincide with reality. For more details about topographic gravity information, it is referred to *Hirt et al.* (2013) and *Hirt & Rexer* (2015), while P-IV describes the handling of high-frequency gravity signals from mountainous topography in practice.

In this context, this thesis focuses on the combination of terrestrial, airborne and satellite gravity measurements with related topographic information (e.g., P-IV). For the derivation of gravity values from satellite altimetry it is referred to *Sandwell & Smith* (1997).

Methods for regional gravity field determination:

As a result of the individual advantages and disadvantages, the challenge is often an optimal combination of different sources of gravity information. While SH functions (Eqs. 2.4 and 2.5) provide a good global representation, they are limited in their ability of spatial localization and generally provide no proper representation of terrestrial data with varying quality or density. Accordingly, LSC and several other methods such as Spherical Radial Basis Functions (SRBF, *Freedon et al.* 1998; *Schmidt et al.* 2007), Stokes's formula (*Heiskanen & Moritz*, 1967; *Ågren et al.*, 2009), multipole wavelets (*Chambodut et al.*, 2005; *Hohlschneider et al.*, 2003), Slepian functions (*Simons*, 2010) or point-mass models (*Sünkel*, 1981; *Ågren*, 2004) are applied for regional gravity field determination. This work focuses on LSC and RLSC, gives reasons for that in Sect. 1.1 and presents the corresponding approaches in P-III and Chap. 3. However, results from other approaches, especially from a calculation with SRBFs (Sect. 4.6), are used for comparisons in Chap. 4 and P-IV. Accordingly, the basics of SRBFs and some connections between different approaches for regional gravity field modeling are shortly outlined in the following. The corresponding references can be used for a more detailed study of the methods, which should not be repeated here. An overview of the mentioned approaches for regional gravity field determination as well as a list of individual advantages and disadvantages is given in *Lieb* (2017).

Radial basis functions are isotropic kernel functions that use the spherical distance between an input point and a target point as primary input. Correspondingly, SRBFs are appropriate functions applied on the sphere. They are generally used to calculate a regular grid of (unknown) coefficients, which is afterwards exploited for the calculation of different gravity functionals. *Freedden et al.* (1998) provide the basics for calculations with SRBFs, which are applied and extended in numerous publications (examples in the following and *Lieb et al.* 2016). *Schmidt et al.* (2007) use these formulations to derive the relation between space localizing methods (spherical splines and wavelets as example for SRBFs) from the general formulation of SH functions. *Bentel et al.* (2013) examine different forms of SRBFs for regional gravity field modeling. Thereby, differences between the shape, the location and the bandwidth of SRBFs are main criteria for the final performance (*Liu et al.*, 2020a). Finally, multiresolution representation allows SRBFs to optimally combine different sources of gravity data to exploit them in specific frequency bands of the gravity field (*Schmidt et al.*, 2007; *Lieb et al.*, 2016).

SH functions use Legendre polynomials as basis for modeling gravity effects, as is done by all of the above mentioned approaches in order to ensure a solution of Laplace's equation (*Hofmann-Wellenhof & Moritz*, 2006) in the global case. While SH functions apply Legendre polynomials for a mere spectral representation, SRBFs, multipole wavelets and Slepian functions use them for a compromise between spectral and spatial representation (*Freedden et al.*, 1998), which is also visualized in *Lieb* (2017). The advantages of SH functions and SRBFs can be combined, when SH functions are used for the low degrees of the gravity field, and spherical wavelets for the medium to high-frequency part (*Schmidt et al.*, 2005). Regarding the remaining methods, LSC applies Legendre polynomials in the definition of covariance functions, which are used to calculate a minimum norm solution (*Tscherning*, 2015). Point-mass models use Legendre polynomials in the expansion of the reciprocal distance. Finally, Stokes's formula includes Legendre polynomials in the definition of the Kernel function within an integration procedure (*Heiskanen & Moritz*, 1967). This joint application of the Legendre polynomials as basis functions in regional gravity field determination also results in similarities among different approaches, which are studied in the several publications: *de Min* (1995) reports about similarities between LSC and Stokes's formula, while *Eicker* (2008) compares LSC with SRBFs from a spline kernel. In specific cases and after some modifications, it is even possible to show a (numerical) equivalence between LSC, Stokes's formula and SRBFs (*Ophaug & Gerlach*, 2017).

Handling of the GGM in regional gravity field determination:

Apart from the variety of methods, there are also three different approaches (referred to as cases) in the handling of the GGM in regional gravity field determination. These approaches are evaluated in the following for their ability to calculate the absolute gravity potential at an IHRF station. Thereby, all three approaches should be combined with topography-induced gravity information whenever this is necessary.

- 1) SHS of high-resolution GGMs is the fastest and easiest approach to calculate arbitrary gravity functionals (e.g., applied in P-I, P-II). In this case, local measurements (which are not already

in the GGM) cannot be included into the calculation and local characteristics might not be presented correctly in the available GGM models. Accordingly, this approach very much depends on the quality of GGMs and suffers heavily from the omission and commission error of the model. In general, the quality of the terrestrial gravity observations (which was included to the corresponding GGM calculation) is the main driver for its final performance. Furthermore, the selection of the GGM can have a considerable impact on the result, as various high-resolution GGMs can differ significantly from each other (P-II). The main value of this approach would display in areas, where all available terrestrial gravity measurements are already included into the high-resolution GGM or the accuracy requirements are not that demanding.

- 2) The combination of a satellite-only GGM with regional and local gravity measurements provides a globally consistent reference surface and allows a good representation of the high-frequency part of the gravity field at the same time (*Pail et al.*, 2010; *Ågren & Sjöberg*, 2014; *Gerlach & Ophaug*, 2017). Its advantage is a good adaptation to the local characteristics, since the method allows a flexible weighting among different data sets. However, this might also be disadvantageous, since several IHRs stations that are calculated with this method are not necessarily consistent due to the possibly high impact of the local measurements.
- 3) A high-resolution GGM can also be refined with regional and local gravity measurements (e.g., *Forsberg et al.* 2014; *Abd-Elmotaal* 2017; *McCubbine et al.* 2018). In this case the calculation can be adapted to local characteristics, while other disadvantages of the first case might remain (e.g., commission error, impact from GGM selection, questionable reliability of GGM). In comparison with case 2, case 3 generally needs less regional gravity field information, and observations in a smaller area respectively.

Although, *Ihde et al.* (2017) recommend case 2 for HSU, this thesis shows why case 3 is generally preferable when the method of RLSC is applied. RLSC allows a consistent inclusion of accuracy information from the high-resolution GGM. Thereby, RLSC presents a significant improvement towards other realizations of case 3, since the GGM is not introduced with a questionable accuracy any more, which was mentioned as a main disadvantage by *Ihde et al.* (2017). Furthermore, the application of regional varying weighting in XGM calculations results in an improved accuracy estimation, which can be included to RLSC calculations in the form of location dependent variance-covariance information (details in Chap. 3). As a result, the selection of the GGM in RLSC has less impact than it would have in other methods, as long as the corresponding accuracy estimation is realistic. In comparison to case 2, the application of case 3 with RLSC furthermore exploits the generally good quality of high-resolution GGMs over the ocean, and provides a high consistency for different stations around the world (P-III).

2.5 Evaluation, summary and research questions

Chap. 2 explains the basics of spherical harmonic series and GGMs (Sect. 2.1), height systems (Sect. 2.2), the IHRS (Sect. 2.3), and regional gravity field determination (Sect. 2.4). Together with P-I it emphasizes that a globally consistent reference is needed for the height system unification, and that satellite gravity missions are the only possibility to provide it with the desired accuracy (Q1). Although, a satellite-only GGM has an accuracy of 1-2 cm at spatial scales of 80 to 100 km, it cannot be used for HSU alone due to the omission error (P-I). In order to reduce the omission error, and to apply a satellite-only GGM for HSU, it has to be refined by regional gravity field determination with local measurements or from a combination towards a high-resolution GGM (Q2).

The quality of different high-resolution GGMs is analyzed with GNSS/leveling in P-II. GNSS/leveling allows an assessment of the error content in GGMs, and can therefore be used for their validation (Q3). In combination with topography-induced gravity effects, GGMs might be able to calculate geoid heights with an accuracy up to 1 cm, in case the terrestrial gravity data in the GGM is of very high quality. This is shown for an analysis from GNSS/leveling data in Germany (P-II). In general, however, the geoid accuracy that is available from a GGM alone, is given with a few centimeters in case of good terrestrial data coverage and some decimeters in case of sparse coverage (Q4). P-II furthermore quantifies how much a HSU depends on the selection of the high-resolution GGM, as it validates 6 different high-resolution models for 24 different data sets from GNSS/leveling. Topography-induced gravity effects can and should be added to the geoid effects in order to model the very high-frequency effects of the gravity field. Obviously, this will become more important if the topography gets rougher. The combination of Chap. 2, P-I and P-II satisfies research objective O-1, as the challenges and benefits for a HSU are explained, and the role of a globally unified GGM is demonstrated.

Apart from the geoid calculation with a GGM alone, Sect. 2.4 gives also an overview of different data and methods for regional gravity field determination. Two strategies for the refinement of a GGM with terrestrial gravity data are discussed, which are based on a satellite-only GGM or a high-resolution GGM respectively. We regard these two methods for regional gravity field determination as generally beneficial towards the GGM-only method in terms of accuracy (*Ihde et al.*, 2017), and consider advantages and disadvantages for both of them (Sect. 2.4). However, the disadvantages from a refinement of a high-resolution GGM with regional gravity data can be reduced significantly, when the model is introduced with reliable accuracy estimation. Consequently, in the next chapter, residual least-squares collocation is presented as a new and beneficial method for the combination of a high-resolution GGM and regional gravity field information.

Chapter 3

Residual least-squares collocation

3.1 Introduction to RLSC

Summary of P-III:

The publication P-III is of highest importance for Chap. 3, since it not only describes the basics and the derivation of RLSC, but also

- explains the fundamentals of LSC on which RLSC is based (*Moritz, 1980*);
- names the reason for adapting LSC and lists the advantages of the RLSC approach;
- justifies a new notation for covariance matrices, which distinguishes between covariance matrices derived from the total average (\bar{C}) and the expectation operator (C);
- introduces a consistent notation system, which allows the distinction between different sources of gravity functionals (e.g., GGM or topographic gravity model) and different forms of covariance matrices;
- highlights the differences to already existing LSC formulations with explicit comparison to *Moritz (1980)*; *Forsberg & Tscherning (1981)*; *Haagmans & van Gelderen (1991)*; *Hofmann-Wellenhof & Moritz (2006)*; *Pail et al. (2010)*; *Sansò & Sideris (2013)* and *Rieser (2015)*;
- explains the benefits, which RLSC provides for the introduction of an IHRS;
- and displays the advantages of RLSC in comparison to standard LSC in a synthetic test case.

This chapter outlines parts of P-III, while it is referred to the original publication for details. Accordingly, Tab. 3.1 provides an overview of the differences between standard LSC and RLSC, which are described in P-III. Thereby, Tab. 3.1 is intended to summarize main aspects in a clear structure, while it cannot provide the same differentiation as given in P-III, since differences between various LSC approaches are not distinguished. As a result of this simplification, LSC approaches with anisotropic or location-dependent covariance information (e.g., *Tscherning 1999*; *Darbeheshiti & Featherstone 2009* or *Migliaccio et al. 2011*) cannot be considered in Tab. 3.1. Furthermore, the advantages of RLSC in comparisons to LSC approaches with included variance covariance information (*Haagmans & van Gelderen, 1991*; *Pail et al., 2010*; *Sansò & Sideris, 2013*) differ from

	Standard LSC	Residual least-squares collocation
Overview	Basic LSC approaches differ in the handling of covariance matrices, RCR, GGM and topographic reduction.	Least squares collocation approach that uses only residuals, and includes individual covariance information for every input quantity.
Literature (theory)	<i>Moritz (1980); Pail et al. (2010); Sansò & Sideris (2013)</i>	P-III
Literature (real data application)	<i>Ågren & Sjöberg (2014); Rieser (2015); Abd-Elmotaal (2017)</i>	P-IV
General approach	Signal covariance matrices \bar{C} model the gravity signal	Error covariance matrices C model accuracies and correlations of input quantities
RCR	Generally included	Included by definition
Covariance GGM	Might be included for satellite-only model, but most approaches do not include the variance covariance information of a GGM	Always included; covariance matrices are derived directly from the XGM normal equation system (P-III, Sect. 3).
Covariance residuals	Empirical covariance fitting (<i>Tscherning & Rapp, 1974</i>) or signal degree variances (Sect. 3.2)	Not included; signal is not modeled in RLSC
Covariance topographic reduction	Not included; modeling of remaining gravity signal instead	Error information is not available, therefore covariance matrices are approximated from signal degree variances (Sect. 3.2)
Modeling of the gravity field	Beyond the resolution of a satellite-only model: independent of the location (homogeneous) and independent of the location (isotropic)	Up to resolution of GGM: location-dependent and anisotropic

Tab. 3.1 – Summary of basic differences between standard LSC and RLSC. A more detailed description of the differences as well as a differentiation of various LSC approaches is given in P-III.

LSC approaches without (e.g., *Forsberg & Tscherning 1981; Hofmann-Wellenhop & Moritz 2006; Rieser 2015*), but cannot be distinguished in Tab. 3.1. However, RLSC advantages to different LSC methods are distinguished in P-III and two main benefits of RLSC exist in comparison to all previous formulations of LSC:

- RLSC includes anisotropic and location-dependent covariance matrices from a high-resolution GGM.
- RLSC formulates a residual concept, which uses only error covariance matrices and considers accuracy information for every input quantity.

These two main advantages provide RLSC with the ability to give more realistic accuracy estimates, and are further explained in the following.

Covariance information of a high-resolution GGM:

In regional geoid determination, the Earth's gravity field is often modeled as isotropic and homogeneous, although this is generally not true in reality (*Tscherning*, 1999). In the LSC formulations by *Moritz* (1980); *Forsberg & Tscherning* (1981); *Hofmann-Wellenhof & Moritz* (2006) and *Rieser* (2015), for example, covariance matrices model an isotropic and homogeneous gravity field. In contrast, RLSC is able to include anisotropic and location-dependent covariance matrices, which are derived from a high-resolution GGM that applies regional varying weighting (*Fecher et al.*, 2015). Thereby, the variance-covariance information is derived directly from the normal equation system of the model, which is formulated in P-III (Sect. 3). Currently, this covariance information from a high-resolution GGM is available for either GOCO05C (*Fecher et al.*, 2015) or one of the XGM models (e.g., XGM2019 by *Zingerle et al.*, 2020 accepted). However, the computation of covariance matrices for input and output is very CPU-intensive (details in the conclusion of P-III). It should also be noted that, in theory, RLSC can also be used with a satellite-only GGM (e.g., GOCO06S). In this case, however, it would lose its main benefits and resemble the already existing approaches by *Pail et al.* (2010) and *Sansò & Sideris* (2013), which already include accuracy information from a satellite-only GGM.

Error covariance matrices in the residual concept:

The difference between RLSC and LSC defined by *Moritz* (1980) is clearly visible when we compare the calculation formulas themselves. However, the difference in the notation is explained first; for the (input) observations \mathbf{l} as a combination of the true input signal \mathbf{t} and the random (stochastic) observation noise \mathbf{n} , P-III uses the following notation for (standard) LSC

$$\bar{\mathbf{s}} = \bar{\mathbf{C}}_{st} (\mathbf{C}_{nn} + \bar{\mathbf{C}}_{tt})^{-1} \mathbf{l}, \quad (3.1)$$

where

- $\bar{\mathbf{s}}$ = output functional,
- $\bar{\mathbf{C}}_{st}$ = signal covariance matrix between input and output,
- \mathbf{C}_{nn} = error covariance matrix for the input \mathbf{l} ,
- $\bar{\mathbf{C}}_{tt}$ = signal covariance matrix for the input \mathbf{l} .

Thereby, our notation includes two adaptations to the formulation by *Moritz* (1980). First, the true gravity functionals are marked by the separated symbols \mathbf{t} (input signal) and \mathbf{s} (output signal). Second, the bar over a quantity marks a covariance function $\bar{\mathbf{C}}$ or a resulting gravity functional (e.g., $\bar{\mathbf{s}}$), which is calculated from the total average $\bar{\mathbf{E}}$ instead of the expectation value \mathbf{E} (details in P-III, Sect. 2.1). Accordingly, the LSC notation in Eq. 3.1 is equivalent to the following notation in *Moritz* (1980)

$$\hat{\mathbf{s}} = \mathbf{C}_{st} (\mathbf{C}_{nn} + \mathbf{C}_{tt})^{-1} \mathbf{l}, \quad (3.2)$$

where every equivalent quantity has the same meaning. Regarding the Eqs. 3.1 and 3.2, the observations \mathbf{l} are described with two different covariance matrices, whereby $\bar{\mathbf{C}}_{tt}$ and \mathbf{C}_{tt} describe the signal part and \mathbf{C}_{nn} the corresponding observation error.

This differs from the approach in RLSC, where the signal part is reduced by applying a RCR procedure. Details about the RCR approach are described in *Hofmann-Wellenhof & Moritz (2006)* or *Rieser (2015)*. Accordingly, the signal part of the observations is reduced by an a priori model without systematic errors. As a result, the signal part is not modeled in the collocation, which is applied to residuals only. In order to highlight quantities, that result from an a priori model, they are marked by a hat operator. Following P-III, the formula for RLSC is

$$\mathbf{s} = \mathbf{C}_{\hat{\mathbf{s}}\hat{\mathbf{l}}} (\mathbf{C}_{\mathbf{l}\mathbf{l}} + \mathbf{C}_{\hat{\mathbf{l}}\hat{\mathbf{l}}})^{-1} (\mathbf{l} - \hat{\mathbf{l}}) + \hat{\mathbf{s}}. \quad (3.3)$$

where

- \mathbf{s} = output functional ,
- $\mathbf{C}_{\hat{\mathbf{s}}\hat{\mathbf{l}}}$ = error covariance matrix between input and output model,
- $\mathbf{C}_{\mathbf{l}\mathbf{l}}$ = error covariance matrix for the input \mathbf{l} ,
- $\mathbf{C}_{\hat{\mathbf{l}}\hat{\mathbf{l}}}$ = error covariance matrix for the input model $\hat{\mathbf{l}}$,
- $\hat{\mathbf{l}}$ = input functional derived from the a priori model,
- $\hat{\mathbf{s}}$ = output functional derived from the a priori model.

Unlike LSC in Eq. 3.1, RLSC in Eq. 3.3 has an error covariance matrix for every input quantity, so that $\mathbf{C}_{\mathbf{l}\mathbf{l}}$ describes the accuracy of the input observations \mathbf{l} , and $\mathbf{C}_{\hat{\mathbf{l}}\hat{\mathbf{l}}}$ the model observations $\hat{\mathbf{l}}$, respectively. Correspondingly, the stochastic modeling of RLSC benefits from involving all related components and provides a more realistic accuracy estimation. It should be noted that LSC in Eq. 3.1 does not correspond to RLSC even when it includes a remove-compute-restore approach, as the covariance matrices $\bar{\mathbf{C}}_{st}$ and $\bar{\mathbf{C}}_{tt}$ stay signal covariance matrices even when they model the residual gravity signal. This difference is described in detail in Sect. 2.3 of P-III. The same section also presents the stochastic model corresponding to Eq. 3.3 (P-III, Eq. 32).

3.2 Covariance functions in RLSC

In RLSC (Eq. 3.3) there are covariance matrices for the observations ($\mathbf{C}_{\mathbf{l}\mathbf{l}}$) and the a priori models ($\mathbf{C}_{\hat{\mathbf{l}}\hat{\mathbf{l}}}$, $\mathbf{C}_{\hat{\mathbf{s}}\hat{\mathbf{l}}}$). While the calculation of the former is explained in detail in the publications P-III and P-IV, respectively, the derivation of the latter ones is shortly discussed in the following.

In P-III and P-IV, the model observations $\hat{\mathbf{l}}$ are a combination of a high-resolution GGM and a topographic gravity model. The corresponding covariance functions of the high-resolution GGM are derived directly from its normal equation system, which is also explained in P-III. For the topographic gravity model, however, there is no accurate accuracy information available (*Rexer et al., 2016*).

Accordingly, the covariance function is approximated from empirical covariance fitting (P-III), which is a common approach in regional gravity field modeling, and explained in detail by *Tscherning & Rapp* (1974). A possible method to do so, is the definition of covariance functions from signal degree variances, which is described in the following.

The statistical behavior of the gravity field (e.g., disturbing potential T) can be described by covariance functions, which are calculated from a global average operator. Their derivation in spherical harmonics is explained in *Heiskanen & Moritz* (1967) or *Rieser* (2015) and not repeated here. Instead, we adopt the resulting covariance function $\bar{C}_{TT}(r, r', \psi)$ for the disturbing potential T between the points $P(r, \vartheta, \lambda)$ and $S(r', \vartheta', \lambda')$ outside the sphere

$$\bar{C}_{TT}(r, r', \psi) = \sum_{n=2}^{\infty} \left(\frac{R^2}{rr'} \right)^{n+1} k_n P_n(\cos \psi), \quad (3.4)$$

where

- ψ = spherical distance between P and S,
- R = constant Earth radius,
- k_n = signal degree variances,
- $P_n(\cos \psi)$ = Legendre polynomials for cosines of the spherical distance ψ .

The signal degree variances k_n for the disturbing potential cannot be measured directly, but are available from a residual GGM by calculating

$$k_n = \sum_{m=0}^n (\Delta \bar{C}_{nm}^2 + \Delta \bar{S}_{nm}^2), \quad (3.5)$$

where $\Delta \bar{C}_{nm}$ and $\Delta \bar{S}_{nm}$ are the fully-normalized coefficients not considering the normal gravity field (Sect. 2.1). When $\Delta \bar{C}_{nm}$ and $\Delta \bar{S}_{nm}$ are provided from a GGM, covariance functions describe an average global gravity field. However, regional characteristics of the gravity field generally do not coincide with a global average, which is why regional gravity field determination needs an adaption of the covariance matrices in Eq. 3.4 (details in Sect. 3 of P-III or Sect. 3.3 of this thesis). Another approach for empirical covariance fitting without using signal degree variances is explained by *Tscherning & Rapp* (1974) or *Rieser* (2015). Regardless of the underlying method, covariance functions are of essential importance for the calculation.

Following the basics of spherical harmonics in Chap. 2.1 the covariance function for the disturbing potential can be used to calculate other functionals by covariance propagation. A detailed summary of various derivatives of the covariance function is given by *Rieser* (2015). In the following, only covariance functions, which are used in P-III, are listed:

Covariance function for the geoid undulation N :

$$\bar{C}_{NN}(r, r', \psi) = \frac{1}{\gamma_0^2} \bar{C}_{TT}(r, r', \psi) \quad (3.6)$$

Covariance function for the gravity anomaly Δg :

$$\bar{C}_{\Delta g \Delta g}(r, r', \psi) = \sum_{n=2}^{\infty} \frac{(n-1)^2}{rr'} \left(\frac{R^2}{rr'}\right)^{n+1} k_n P_n(\cos \psi) \quad (3.7)$$

Cross-covariance function between geoid undulation N and gravity anomaly Δg :

$$\bar{C}_{N \Delta g}(r, r', \psi) = \frac{1}{\gamma_0} \sum_{n=2}^{\infty} \frac{(n-1)}{r'} \left(\frac{R^2}{rr'}\right)^{n+1} k_n P_n(\cos \psi) \quad (3.8)$$

The covariance functions for P-IV are calculated correspondingly, whereby γ_0 is replaced by γ_Q (compare Eqs. 2.10 and 2.11), as P-IV uses the height anomaly ζ instead of the geoid undulation N . Furthermore, the $(n-1)$ term in the Eqs. 3.7 and 3.8 is replaced by $(n+1)$ to account for the gravity disturbances (Eq. 2.9) in this publication.

3.3 Application of covariance functions

For applications in regional gravity field determination, covariance functions (Eqs. 3.6 to 3.8) are not calculated from degree 2 to infinity, but adapted to the local residuals instead (*Tscherning & Rapp, 1974*). Thereby, an Empirical Covariance Function (ECF) is calculated from the reduced input observations, and a Model Covariance Function (MCF) is fitted to it. P-III explains details about this procedure, which includes a visual comparison between ECF and MCF, and the derivation of the resulting signal degree variances k_n . Accordingly, in P-III, for example, the covariance function is applied from SH degree 720 to 2160 with a scaling factor, as this fits the local residuals. This is even consistent to the calculation scenario, as SH degrees from 2 to 719 are removed by the XGM2016 model, and degrees above 2160 are neglected due to the synthetic test case. In P-IV, covariance matrices are calculated to the maximum SH degree 5400. For the airborne observations, the gravity signal above this degree is negligible, because of signal attenuation at the flight height and an additionally applied low-pass filter (P-IV). For modeling the gravity field on the Earth's surface we do not expect the terrestrial observations to improve the result above SH degree 5400, which is due to their limited spatial resolution. Accordingly, we consider topography-induced gravity information as best gravity source above SH degree 5400, and therefore apply ERTM2160 (*Hirt et al., 2014*) in P-IV. However, it should be noted that (R)LSC is not very sensitive to the maximum SH degree, as signal degree variances decrease with rising degree.

The Earth radius R in Chap. 3.2 is commonly included as constant value. In *Moritz* (1980) or *Hofmann-Wellenhopf & Moritz* (2006), for example, R is chosen as approximate mean radius of the Earth

$$R = \sqrt[3]{a^2 b} \approx 6371 \text{ km}, \quad (3.9)$$

where a is the semimajor, and b the semiminor axis of the Earth's ellipsoid. This is also the implementation that is applied in P-III. Correspondingly, the $\left(\frac{R^2}{rr'}\right)$ term depends only on the height of the two observation points (h_R, h'_R) about the reference sphere R , which is defined as

$$\begin{aligned} h_R &= r - R, \\ h'_R &= r' - R. \end{aligned} \quad (3.10)$$

In case that variances are extracted from the covariance functions in Chap. 3.2, they vary mainly by their height h_R above the reference sphere R . However, the height h_R depends not only on the ellipsoidal height h (Eq. 2.13), but also on the latitude φ . As a result, variances from the a priori model (e.g., Eqs. 3.6 to 3.8) show a significant dependence on latitude. This is presented for the variance of the topographic gravity model in Fig. 5 of P-III. The dependence on latitude is a common effect in representations of covariance functions, and for example, also visible in *Gerlach & Fecher* (2012). However, in a general point of view this dependence on latitude does not make sense, as it affects (R)LSC predictions, but is generally not included in the observation accuracy itself. In P-III, for example, the observation accuracy from altimetry does not depend on the latitude in the way the variance model does. With this consideration in mind, the calculation of the $\left(\frac{R^2}{rr'}\right)$ term was adopted in P-IV.

In P-IV, the reference surface is not implemented by a sphere with a constant radius R , but with the changing radius R_{ell} of an ellipsoid. Following a presentation in *Heiskanen & Moritz* (1967), the relation between the ellipsoidal height h (Sect. 2.2) for a point $P(r, \varphi, \lambda)$, and the corresponding ellipsoidal radius R_{ell} is schematically presented in Fig. 3.1. In contrast to Eq. 3.10, this results in the following approximation

$$\begin{aligned} h &\approx r - R_{\text{ell}}, \\ h' &\approx r' - R'_{\text{ell}}. \end{aligned} \quad (3.11)$$

Correspondingly, the term $\left(\frac{R^2}{rr'}\right)$ now depends mainly on the ellipsoidal height h of an observation instead of its height h_R above the reference sphere (Eq. 3.10). As a result, we get rid of the dependence on latitude that is visible in P-III and *Gerlach & Fecher* (2012) resulting in better fitting covariance matrices. This is of special importance in P-IV, as the $\left(\frac{R^2}{rr'}\right)$ term generally has a higher influence for airborne gravity observations.

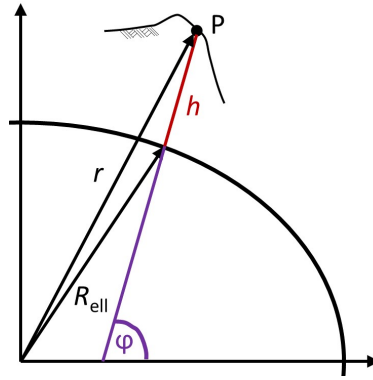


Fig. 3.1 – Relationship between spherical coordinate r , ellipsoidal height h and ellipsoidal radius R_{ell} for a point $P(r, \varphi, \lambda)$ on the Earth's surface.

3.4 Evaluation, summary and research questions

P-III repeats the basics of collocation with random errors, which are given by *Moritz* (1980, Chap. 14). Following the publication of *Tscherning* (1999), P-III describes, why homogeneous and isotropic covariance functions in LSC cannot provide an optimal result when modeling the gravity field of the Earth. Consequently, P-III derives a mathematical concept to include location-dependent and anisotropic covariance matrices from a high-resolution GGM to LSC, naming it RLSC, and highlighting differences to the original approach by *Moritz* (1980). In this method, all input quantities are included with a consistent error covariance matrix, which describes corresponding accuracies and correlations. In P-III, for example, error covariance matrices are included for the gravity observations, XGM2016 and the topographic gravity model. Covariance functions of XGM thereby describe existing correlations, while a covariance function of the topographic gravity model is not available, and therefore included by an isotropic and homogeneous approximation. By this approach, the stochastic model incorporates all involved components and provides more realistic accuracy estimates than other LSC approaches. Accordingly, P-III satisfies the research objective O2 and the research question Q5.

In contrast to RLSC, previous formulations of LSC (e.g., *Moritz* 1980; *Haagmans & van Gelderen* 1991; *Hofmann-Wellenhop & Moritz* 2006; *Pail et al.* 2010; *Sansò & Sideris* 2013; *Rieser* 2015) always include signal covariance matrices. Furthermore, RLSC is the first approach that includes full covariance information of a high-resolution GGM directly to collocation, while *Haagmans & van Gelderen* (1991); *Pail et al.* (2010) and *Sansò & Sideris* (2013) already included covariance matrices from satellite-only GGMs. The biggest differences between RLSC and LSC arise when LSC approaches do not include the accuracy of the reduction model (e.g., *Forsberg & Tscherning* 1981; *Hofmann-Wellenhop & Moritz* 2006 and *Rieser* 2015), or do not implicitly include a reduction model (*Moritz*, 1980). The more detailed description of these differences in P-III, the resulting advantages and the explanations in Chap. 3 answer research question Q6. Furthermore, they result in the following advantages for a possible IHRS calculation.

RLSC can benefit from the generally good accuracy of high-resolution GGMs over oceans and in coastal areas, where the manual combination of different data sources might be more complicated (discussion in Sect. 5.2). Furthermore, P-III demonstrates that regional gravity field modeling with RLSC outperforms LSC in areas with sparse gravity data coverage and explains, why RLSC, in general, produces better results when the number of local gravity observations is limited. This helps the establishment of an IHRF, as its stations should be distributed globally, therefore obviously including areas with sparse data coverage as well. Finally, RLSC is able to provide realistic accuracy estimates, which are of essential importance for the IHRF (*Ihde et al.*, 2017). A general disadvantage of the application of high-resolution GGMs as reference model for the IHRF might be, that errors from the model will most likely affect the IHRF as well. However, in RLSC, possible errors in the GGM should at least be represented in the corresponding covariance matrices, which therefore considers these errors in the resulting accuracy estimates.

Chapter 4

The 1 cm geoid experiment

4.1 IAG working group 2.2.2

The definition of a regional gravity calculation test case in Colorado was decided during the business meeting of IAG JWG 0.1.2 (Strategy for the Realization of the IHRS, chair L. Sánchez) at IAG-IASPEI 2017 (Kobe, Japan). This test case called 'the 1cm geoid experiment' was established as JWG 2.2.2 within the IAG period from 2015 to 2019, and chaired by Y. M. Wang. Its purpose was the validation of different methodologies for regional gravity field determination with identical input data. The designed area in the US states Colorado and New Mexico was selected for its dense gravity data availability from terrestrial and airborne measurement campaigns, and due to the contained Geoid Slope Validation Survey 2017 (GSVS17). In the GSVS17, positions, gravity values and deflections of the vertical were measured with very high accuracy. Although, the results and computations of GSVS17 are not yet publicly available (June 2020), they should be published soon (*D. van Westrum, personal communication*).

Within JWG 2.2.2, 14 international groups calculated geoid heights along the 223 benchmarks of GSVS17. 13 of these groups also submitted corresponding height anomalies and potential values, whereby the height anomalies are studied in P-IV and this thesis. Accordingly, P-IV also explains the background of 'the 1 cm geoid experiment' in more detail. It highlights the RLSC result that was calculated in this context, while the findings are also summarized in Sect. 4.3. P-IV includes the first application of RLSC with real gravity data, since P-III used only synthesized observations. Furthermore, P-IV contains airborne gravimetry in RLSC for the first time, whereby resulting challenges and solutions are described in Sect. 4.2.

Two summary papers of the JWG by *Wang et al.* (in review) and *Sánchez et al.* (in review) each include an overview of the 1 cm geoid experiment, name all groups that participated, and shortly describe the different methodologies that have been applied. While *Wang et al.* (in review) compare the height anomaly and geoid height results along GSVS17 among all participants and provide preliminary comparisons against the GSVS17 measurements (details in Sect. 4.5), *Sánchez et al.* (in review) provide similar comparisons for the potential values. However, both summaries are not published yet (June 2020), and only *Wang et al.* (in review) is available for discussion in

this thesis (Sect. 4.4 and 4.5), as I am a co-author. Apart from the gravity functionals at GSVS17 benchmarks, participants of the 1 cm geoid experiment also calculated a regular grid of height anomalies and geoid heights with the approximate size of 500 x 300 km on the Earth's surface. In *Wang et al.* (in review), these grid calculations are validated against a set of historical GNSS/leveling data, and among each other.

My contribution to the summary paper (*Wang et al.*, in review) is given mainly from the leadership in the RLSC contribution, which is denoted as 'IAPG' (Institute of Astronomical and Physical Geodesy). In the context of a research trip to National Geodetic Survey (NGS), I discussed the content of the summary paper with the paper's main author (Y. M. Wang) and contributed several ideas and corrections to the manuscript at that time (November 2019). Additionally, I helped with reviewing and editing in the final stages of the manuscript.

Furthermore, I am a co-author of the publication *Liu et al.* (2020b), which describes another solution of the 1 cm geoid experiment, that is named DGFI (Deutsches Geodätisches Forschungsinstitut) in *Wang et al.* (in review). This contribution uses SRBFs and explains this approach in detail, while its results are summarized in Sect. 4.6 of this thesis. As DGFI joined the 1 cm geoid experiment as one of the latest groups, I helped the paper's main author Q. Liu with the general introduction to the project and my experience about the corresponding gravity observations. Together we prepared the gravity data selection for the SRBF's input (e.g., detection of duplicate observations, reduction of airborne observation frequency), but it should be noted that the calculations of IAPG and DGFI include significant differences in the selection and inclusion of airborne gravity observations (P-IV; *Liu et al.* 2020b). Furthermore, I selected the most suitable (a priori) reduction models for airborne and terrestrial gravity observations, and accordingly, the solutions IAPG and DGFI include similar reduction models (Sect. 4.4). Lastly, I contributed by editing the manuscript.

It should be noted that my overall contribution to *Wang et al.* (in review) and *Liu et al.* (2020b) is relatively small in comparison to the corresponding main author, so that these publications are not included as an integral part of this thesis. All methods in the 1 cm geoid experiment rely on GGMs for data reduction, and often use the same models (*Wang et al.*, in review). Furthermore, the final results of P-IV differ significantly from the a priori models, which are used in the remove-compute-restore approach (demonstrated in Sect. 4.4). Accordingly, the fact that some similarities occur in the gravity data handling between the RLSC approach (IAPG) and the SRBF approach (DGFI) is not sufficient to consider these results as strongly correlated.

4.2 Application of low-pass filters in airborne gravimetry

Airborne gravity measurements differ from terrestrial gravity observations not only due to the signal (content and frequency, see Sect. 2.4), but also because of the corresponding noise effects. In general, the noise in airborne gravity measurements is higher due to the measurement in motion, and is handled by a low-pass filter (*Wei & Schwarz, 1998; Childers et al., 1999; Olesen, 2003; Li, 2011; Becker, 2016*). Correspondingly, the main challenge in the usage of airborne gravity data is the separation between signal and noise, which constitutes in the following problem: removing the high-frequency noise from airborne observations will also result in an attenuation of the signal, while keeping the full signal is not possible without retaining significant parts of the noise. Accordingly, the low-pass filter that is applied to airborne observations should constitute the best compromise between removing the noise and keeping the signal (*Childers et al., 1999*).

In the introduction of P-IV, this aspect is explained in more detail, while the corresponding Sect. 2 ('Reasons for low-pass filter in airborne gravimetry') justifies the inclusion of a low-pass filter to airborne gravity observations in the GRAV-D project (Gravity for the Redefinition of the American Vertical Datum). While a low-pass filter for airborne gravity measurements is very effective in reducing the observations noise, it also correlates the measurements (and the gravity signal). However, these correlations are not considered in previous LSC approaches, where low-pass filtered observations are generally assumed as uncorrelated (*Forsberg et al., 2000, 2014; Hwang et al., 2007*). Accordingly, in Sect. 3 of P-IV ('Methodology'), an approach for the consistent inclusion of a low-pass filter to the functional and stochastic model of RLSC is derived at the example of a Gaussian low-pass filter. As a result, the approach in P-IV should give a more consistent error modeling and an improved accuracy estimation. Especially in the combination with other data sets (e.g., terrestrial gravity) it appears important to consider the correlations in filtered airborne gravity observations. Finally, the one-step RLSC approach allows to consider the very high resolution of airborne gravimetry in along-track direction, which is often not possible in other approaches (see P-IV) being based on gridded input data.

4.3 Validation of RLSC in Colorado

We consider the frame of the 1 cm geoid experiment as perfect validation opportunity for the RLSC method, since we can derive a reference result, although the experiment uses real gravity data for the calculation. This follows from the fact that the mean value of 14 independent results (13 for height anomaly) along the 223 benchmarks of GSVS17 is assumed to be of much higher accuracy than an individual result itself (P-IV). Correspondingly, we calculate the mean value from all results of the 1 cm geoid experiment, denote it as 'mean reference', and compare our result with it (P-IV). It should be noted that all comparisons in P-IV are computed for the height anomaly ζ , since we (and

most of the groups in JWG 2.2.2) use the theory of Molodensky (see Chap. 2.2) for the calculations. Comparisons with the geoid height N can be found in *Wang et al.* (in review), but suffer heavily from the geoid-quasigeoid separation term, which is not consistent among the groups. Additional validations for the absolute potential value W are presented in *Sánchez et al.* (in review). Apart from the comparison to the mean reference, several internal validations in P-IV allow the assessment of our own result, and provide insights for the target area and available data sets. The findings from comparisons in P-IV are summarized in the following:

- Our output grid (height anomalies ζ) provides significant benefits towards available gravity models. Compared to the combination of our a priori models, which consist of XGM2018 (internal successor of XGM2016), dV_ELL_Earth2014 (*Rexer et al.*, 2016; *Hirt & Rexer*, 2015), and ERTM2160, our result shows notable improvements in the medium wavelengths of the gravity field. These differences between SH degree 720 and 2190 represent mainly the benefit of the gravity observations towards the a priori models, which consist only from topography-derived information in these degrees. In comparison to EGM2008 (*Pavlis et al.*, 2012) our result includes long wavelength improvements from the GOCE mission.
- The analysis of output residuals indicates a very good consistency between satellite, terrestrial and airborne gravity data in the non-mountainous regions. However, the terrestrial measurements show partial disagreements to satellite and airborne observations in the highly mountainous regions of Colorado. We assume that these differences result at least partially from outliers or measurement errors in the gravity database of the terrestrial observations. Furthermore, the inhomogeneous data distribution should be considered: terrestrial observations are often located in mountain valleys, which could result in a systematic bias for the representation of the full gravity field.
- Further improvements of the RLSC result could be reached by an outlier detection or an iterative RLSC approach, where the output residuals are used to derive input accuracies for a second RLSC calculation.
- In comparison to the mean reference our height anomaly result has a mean value of 1.0 cm and the lowest standard deviation (7.5 mm) among all 13 results (confirmed by *Wang et al.* in review). When the individual mean offsets are corrected, our solution is the only result that stays within ± 2 cm to the reference, while it furthermore provides a realistic accuracy estimation.
- Four alternative solutions (with adapted RLSC input) provide variations between a few millimeter and up to 6 cm (P-IV, Fig. 11). This indicates that first, RLSC is able to adjust with the necessary flexibility when there is detailed information about the individual data sets; and second, that the remaining differences among the methods result partly from flexible weighting of the data sets (satellite, terrestrial and airborne observations), and not only from variations in the regional gravity calculation methods, the reduction models or the topographic modeling.

P-IV and this chapter mainly validate and quantify the performance of RLSC, while the following two chapters focus on the results of the 1 cm geoid experiment in general, their error contributions and the quality of different methods.

4.4 Comparisons to a mean reference

The individual groups in the 1 cm geoid experiment provide height anomaly results which differ with a standard deviation of 7.5 mm to 2.4 cm from the mean reference (P-IV). In doing so, 10 out of 13 groups show standard deviations between 1 and 2 cm, which is considered as the corresponding benchmark. A description of each method and further statistics are presented in *Wang et al.* (in review), while visualizations of the differences can be found in P-IV and *Wang et al.* (in review). It should be noted that the input gravity measurements in this evaluation scenario are identical for all groups, and accordingly, the mentioned standard deviations cannot be considered as overall accuracy for regional gravity field determination. However, the differences include effects from regional gravity field and topographic modeling methods, global reduction models, weighting between different data sources and conventions. The conventions are mostly unified during several stages in the 1 cm geoid experiment, which is shown in *Wang et al.* (in review). However, some differences remain even after the final iteration (e.g., theory of Molodensky vs. Stokes, Sect. 2.2).

P-IV demonstrates that the different handling and relative weighting of available data sources (in the 1 cm geoid experiment: satellite, terrestrial and airborne measurements) have a significant effect to the final performance. This effect should be approximated based on the calculations in P-IV, where three RLSC results are presented with different relative weighting between airborne and terrestrial data. In Fig. 4.1, the three combined solutions are repeated from P-IV in relation to the mean reference, which is defined as zero. The black curve shows the final RLSC result in the 1 cm geoid experiment. The green curve is based on the same calculations, but includes a reduced relative weight for the airborne observations, while it is increased for the purple curve respectively (details in P-IV). The standard deviation of the differences between the final result (black) and the two alternate versions (green and purple) is 0.4 and 0.5 cm, respectively. These are effects resulting from a slight modification within a consistent processing method, which even includes the same weighting for the satellite information and the XGM2018 in general. Correspondingly, the effect of relative weighting within the 1 cm geoid experiment, where we have different approaches which all differ in their data reduction, data thinning (see P-IV) and downward continuation, is assumed to be significantly higher, and accounted for with 0.5 to 1 cm at least.

The additional curves in Fig. 4.1 show model-only solutions. The red curve is the height anomaly result for the combination of our a priori models (XGM2018, dV_ELL_Earth2014, ERTM2160), which equals Eq. 29 in P-IV without the RLSC effect ($\Delta \zeta_{\text{out}}$). Like already discussed in P-IV, the model only solution results in significant disadvantages in the medium wavelengths of the gravity

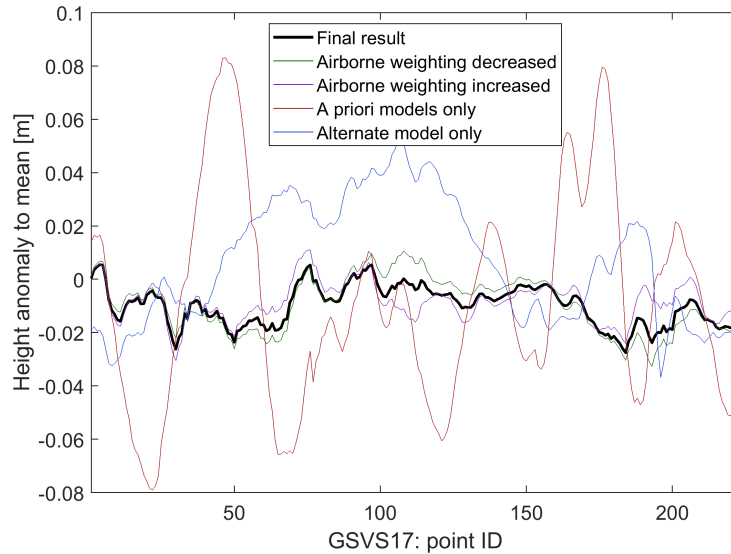


Fig. 4.1 – Comparison of different height anomaly solutions along GSVS17.

field, where it contains only topography-derived gravity information instead of measurements. In the Colorado test area, the topography is generally highly mountainous. Additionally, GSVS17 runs along mountain valleys and over mountain passes, where the mere topographic information from dV_ELL_Earth2014 seems not reliable enough to describe the real gravity field with a very high accuracy. In Fig. 4.1, we cannot see any correlations between the final RLSC result (black) and the combination of our a priori models (red). Correspondingly, the two solutions IAPG and DGFI in the 1 cm geoid experiment are assumed to include only minor correlations, although their a priori models are very similar and differ only in the version of XGM. The blue curve in Fig. 4.1 is an EGM2008 based model-only solution, which is combined with ERTM2160 for the gravity field effects above SH degree 2160. In the medium wavelengths of the gravity field, the blue curve fits generally better to the mean reference than the a priori models (red). However, we see a long-wavelength deviation due to missing GOCE information. Accordingly, the interpretation of model-only solutions along GSVS17 in Fig. 4.1 is identical to the corresponding analysis in P-IV (Fig. 7), which used grid comparisons.

In terms of a statistical comparison towards the mean reference, the a priori models in P-IV have a standard deviation of 4.0 cm with a mean value of -0.8 cm, while the EGM2008 based solution has a standard deviation of 2.3 cm with a mean of 0.6 cm (Tab. 4.1). Correspondingly, we can verify that in a comparison to the mean reference along GSVS17, regional gravity field modeling in general provides better results than a solution from SHS or a combination of models (theory described in Chap. 2.4). RLSC shows much better standard deviations than the model-only solutions. However, it should be noted that the model-only solutions in the area have generally not included the airborne gravity measurements yet, which could lead to an improvement of those in the future. Furthermore, the mean reference of all groups from the 1 cm geoid experiment is not the perfect validation for global models or SHS, as is explained in the following chapter.

Solution	SD	Mean value	Description	Figure
RLSC ('IAPG')	0.7 cm	1.0 cm	Sect. 4.3	Fig. 4.1; P-IV: Fig. 10 & 11
SRBF ('DGFI')	0.9 cm	0.5 cm	Sect. 4.6	in <i>Liu et al.</i> (2020b)
EGM2008	2.3 cm	0.6 cm	Sect. 4.4	Fig. 4.1
A priori models in P-IV	4.0 cm	-0.8 cm	Sect. 4.4	Fig. 4.1

Tab. 4.1 – Comparison of different solutions to the mean reference of the 1 cm geoid experiment in Colorado. Provided are Standard Deviation (SD), mean value, the corresponding chapter in this thesis and the figure, where the solution is visualized.

4.5 Quality assessment from GSVS17 measurements

The quality of individual solutions is validated against a reference mean value in Sect. 4.3 and 4.4, but can also be analyzed in comparison to independent GNSS/leveling measurements with a higher accuracy, which will be available from GSVS17. These GSVS17 measurements should be published together with a detailed description and evaluation by *van Westrum et al.* (in review). They were purposefully not shared within the 1 cm geoid experiment in order to provide an independent validation method for the results of the individual groups (*Wang et al.*, in review). However, the JWG's summary paper by *Wang et al.* (in review) already includes an in advance comparison, which shows the visual difference of individual solutions with GSVS17 and the corresponding mean value, standard deviation, minimum and maximum value. It should be noted that the submission of the summary paper (April 2020) by *Wang et al.* (in review) was much later than the submission of P-IV (early November 2019). Accordingly, P-IV does not include comparisons with the measurements of GSVS17, and this thesis only a general discussion, as the actual values of GSVS17 are still not publicly available (June 2020). For the comparisons of individual results with GSVS17, a bias has to be removed (*Wang et al.*, in review), which is included in the orthometric heights of NAVD88 (North American Vertical Datum of 1988).

In *Wang et al.* (in review), the height anomalies of the 1 cm geoid experiment differ with standard deviations of 1.8 to 3.6 cm from the GSVS17 measurements. Thereby, 12 out of 13 solutions range within the standard deviations from 2.5 to 3.6 cm, which is considered as the overall quality of gravity data and methods in this case (since the accuracy of the GSVS17 measurements is assumed to be very high). However, the GSVS17 measurements show systematic effects compared to the individual solutions from the 1 cm geoid experiment (*Wang et al.*, in review). While the height anomaly of the models is in average a few centimeters higher than GSVS17 from benchmark 1 to 165, it is several centimeters lower after this point. At one point around benchmark 185, all solutions from the 1 cm geoid experiment are at least 3.5 cm below GSVS17, and the mean reference shows absolute differences of more than 5 cm to GSVS17 at some benchmarks. This effect cannot be traced back to the methods, which are generally independent from each other, and are likely to result from systematic effects within the gravity data of the 1 cm geoid experiment or even a remaining problem in the GSVS17 validation. Accordingly, the overall quality of 2.5 to 3.6 cm includes a significant con-

tribution from systematic effects in the underlying measurements. It can be expected that even a perfect method in the 1 cm geoid experiment could not reach results, which are similar to GSVS17. As a result, GSVS17 cannot be used for the validation of different methods without adaptations, and the comparison to the mean reference is currently considered as the preferred quality assessment for modeling methods within the 1 cm geoid experiment.

4.6 Co-author publication: *Liu et al. (2020b)*

Accordingly, the DGFI result in *Liu et al. (2020b)* is also validated against the mean reference of height anomalies along GSVS17. With a mean value of 0.5 cm and a standard deviation of 0.9 cm (Tab. 4.1), the result from SRBF is the second solution with a standard deviation below 1 cm (*Wang et al.*, in review). Note that *Liu et al. (2020b)* do not include the same value, as the publication focuses on Root Mean Square (RMS) calculations, where its difference to the mean reference is 1.0 cm. *Liu et al. (2020b)* offer the only solution in the 1 cm geoid experiment, which results are from SRBFs, and explain the corresponding method in detail. Thereby, the publication highlights the effects and the characteristics that result from the selection of various SRBFs. Unlike P-IV, this publication also includes comparisons about geoid heights (along GSVS17), but shows clearly that the comparison of height anomalies is beneficial in the 1 cm geoid experiment. This also supports the findings in *Wang et al. (in review)*.

Like P-IV, *Liu et al. (2020b)* include height anomaly solutions in case either the terrestrial or the airborne data set is not included to the calculation. Both publications agree that the combination of all available data sets is clearly beneficial to the respective 'single solutions', and show this visually (Fig. 11 in P-IV; Fig. 6 in *Liu et al. 2020b*). In both cases, the terrestrial-only solution provides better results than the airborne-only solution, as the difference between airborne-only solution and mean reference is dominated by a specific wavelength. Obviously, in a mountainous region, airborne gravity measurements with a setting like in the GRAV-D project (e.g., data line spacing 10 km) are not recommended as only gravity observation source. However, P-IV and *Liu et al. (2020b)* show a much better agreement for other areas in the Colorado experiment, which indicates that the lack of terrestrial observations would have a much smaller impact there.

In general, methods for regional gravity field determination depend on the quality of a priori models. This results from the fact that local gravity field calculations cannot determine the long wavelength components of the gravity field, which are mainly available from satellite missions (Sect. 2.2). Furthermore, the density of terrestrial observations is in general not sufficient to determine the very high frequencies of the gravity field, which are largely correlated to topography and approximated from it (*Hirt et al., 2013; Rexer et al., 2016*). Fig. 4.1 and Sect. 4.4 indicate that a priori models alone are generally not sufficient to meet requirements of very high accuracy. However, the results in P-IV and *Liu et al. (2020b)* suggest that RLSC and SRBFs work well with the corresponding a priori mod-

els, as the combination of XGM, dV_ELL_Earth2014 and ERTM2160 is applied in the two solutions with the lowest standard deviation (in comparison to the mean reference for height anomalies). Thereby, the amplitudes of the very high frequencies in the solutions IAPG and DGFI are relatively small by comparison to other methods (P-IV, Fig. 10 and *Wang et al.* in review), which supports the inclusion of ERTM2160. More importantly, the same effect can be observed in a validation against the GSVS17 measurements (*Wang et al.*, in review), which confirms the corresponding handling of high-frequency signal. It should be noted that it is not possible to evaluate the XGM model from the comparison to the mean reference, as more than half of the participating groups included it to their calculation (*Wang et al.*, in review). Accordingly, the differences between XGM and the GSVS17 measurements should be studied in detail, as soon as the GSVS17 measurements are published with a detailed documentation of their calculation.

4.7 Co-author publication: *Wang et al.* (in review)

P-IV and previous parts of this chapter explain why the comparison to a mean reference along GSVS17 is the best approach to validate different methodologies for regional gravity field determination in the 1 cm geoid experiment. Apart from the evaluation of standard deviations and mean values in comparison to the mean reference (Sect. 4.4, P-IV) and the analysis of the high-quality measurements along GSVS17 (Sect. 4.5), *Wang et al.* (in review) provide further validations, which are partially discussed for RLSC and SRBFs in the following.

In the comparison against the mean reference, *Wang et al.* (in review) also present a statistical value which is called 'range'. It gives the bandwidth between the maximum and minimum difference from the mean reference. While this range is 3.4 cm for the IAPG result and 4.3 cm for DGFI, the average of the remaining methods amounts a range of 8.4 cm. RLSC and SRBFs provide not only the lowest standard deviations, but also the smallest peak deviations to the mean reference. Accordingly, the calculation of these two methods is less likely to include significant errors, which could result from data preparation, the remove-compute-restore approach or basic definitions. This is considered to be an additional prove of their reliability in the 1 cm geoid experiment.

The 1' x 1' height anomaly grids, which are submitted in the 1 cm geoid experiment, are also evaluated against a common mean reference. However, it should be considered that unlike the GSVS17 benchmarks, the definition of the output grids and their positions was not generalized among all groups. Accordingly, different groups might calculate gravity functionals at a different topography, and *Wang et al.* (in review) had to interpolate some grids due to different cell-registrations. In case one solution is considered as an outlier, the standard deviations in comparison to the mean reference amount from 1.5 to 2.9 cm. The corresponding range varies from 18.0 to 44.9 cm accordingly. In both cases, the DGFI result shows with 1.5 cm and 18.0 cm the smallest (best) values, whereby RLSC is slightly behind with 1.8 cm and 20.3 cm respectively. In general, the standard

deviation of the grid comparison increases by a factor of 1.5 to the GSVS17 benchmarks. We conclude that this increase results mainly from differences in the output positions among various groups. Accordingly, the comparison of grid results is not as reliable as the comparison of GSVS17 benchmarks in order to evaluate an individual method's quality. The comparison of 1' x 1' geoid grids is also included in *Wang et al.* (in review), but includes the separation term, as most groups calculate the height anomaly ζ first, and derive the geoid height N from it. As a result, all values for the quality assessment of geoid heights N increase significantly in comparison to the height anomaly ζ . For the geoid heights the standard deviations are between 2.1 cm and 5.6 cm, while the range amounts for 25.0 to 68.7 cm. However, it should be noted that in this case no solution is identified as outlier.

In *Wang et al.* (in review) these geoid height grids are also used for the validation with historical GNSS/leveling observations, which allow the derivation of geoid values N . However, the significance of these comparison is limited by the following aspects:

- The validation of GNSS/leveling observations also includes errors from the separation term between the height anomaly ζ and the geoid height N .
- In order to compare the individual solutions to the GNSS/leveling observations, the geoid height grids have to be interpolated at the GNSS/leveling benchmarks. In the mountainous area of the Rocky Mountains, this interpolation is likely to produce effects in the measurable range.
- The GNSS/leveling observations include a tilt and a bias, which is reduced by the values from a mean geoid grid. Although, this reduction should be able to characterize the local bias/tilt, some effects from the separation term or the topographic reduction could remain in the comparison.
- According to *Wang et al.* (in review) the quality of historical GNSS/leveling observations in the mountainous areas of the Rocky Mountains is believed to be poor. It is estimated to be between 3 and 5 cm.

Correspondingly, the analysis of historical GNSS/leveling observations cannot be the main indicator for the quality of different solutions in 'the 1 cm geoid experiment'. The standard deviations in this comparison are between 4.3 and 6.0 cm, whereby RLSC has 4.9 cm and SRBFs have 4.8 cm. The range is between 27.8 and 39.9 cm (when one solution is considered as outlier). RLSC has a range of 31.8 cm, while SRBFs have 34.5 cm. Accordingly, RLSC and SRBFs produce average results in the validation from historical GNSS/leveling observations.

4.8 Evaluation, summary and research questions

P-IV applies RLSC with original gravity field observations for the first time. It explains why airborne gravity measurements should be smoothed with a low-pass filter, and how this filter is considered in the functional and stochastic model of RLSC. Since previous LSC approaches do not consider correlations from low-pass filtered observations, the RLSC concept in P-IV should be able to improve the combination of heterogeneous gravity data and provide a more realistic accuracy estimation. Correspondingly, the formulation in P-IV explains, how and why a low-pass filter is included to the RLSC formulation, which answers research question Q7. P-IV also describes the RLSC result within the scope of IAG JWG 2.2.2 'the 1 cm geoid experiment'. Accordingly, the purpose and main conclusions of P-IV are summarized in Sect. 4.1 and Sect. 4.3, respectively.

The available terrestrial and airborne gravity data in Colorado and New Mexico are used for regional gravity field modeling by 14 international groups. In order to evaluate the height anomaly results along the GSVS17 benchmarks, a mean value of all solutions is used as reference. In a comparison against this reference, the height anomaly solutions IAPG with RLSC and DGFI with SRBFs provide the smallest standard deviations among all results (0.7 and 0.9 cm respectively). Although, this does not necessarily mean they are the best methods for regional gravity field modeling, it demonstrates their validity and robustness in a challenging real data scenario. This is also supported by the small peak-to-peak range, which both methods have in the comparison to the mean reference. Furthermore, the comparisons verify the results of the newly developed concept of RLSC with an included low-pass filter approach (P-IV). Currently, the comparison to the mean reference along GSVS17 is considered as one of the most meaningful quality assessments. This chapter and *Wang et al.* (in review) also describe other comparisons and validations for the results in the 1 cm geoid experiment. Thereby, RLSC and SRBFs produce either good or average results. The detailed description in P-IV and the analysis in this chapter answer research question Q8, as they evaluate the performance of RLSC in various validations.

Within the 1 cm geoid experiment we result in the following conclusions for the error assessment: the overall accuracy of height anomaly calculations with various methods along GSVS17 is generally between 1 and 2 cm, when the input accuracy of gravity measurements is not considered. In a comparison to real measurements of high accuracy (GSVS17), various methods show differences between 2.5 and 3.6 cm. However, this presently includes systematic effects, which result most likely from the terrestrial gravity observations in the 1 cm geoid experiment. A proportion of these comparison results exists only from differences in the relative weighting between terrestrial and airborne observations. In an analysis along GSVS17, this effect is estimated with approximately 1 cm. The quality of two model-only solutions was investigated as well, and indicates significant disadvantages along GSVS17. However, the performance of these solutions cannot be quantified directly, as they should be compared to the high-quality observations from GSVS17 instead of the mean reference (as done in Sect. 4.4).

In the overall structure of this thesis, Chap. 4 and P-IV apply and verify RLSC in a combination of terrestrial, airborne and satellite information, which satisfies research objective O3. Chap. 4 specializes the RLSC concept from Chap. 3 for a data scenario in Colorado. In collaboration with P-IV, it thereby validates the RLSC method with real data for the first time.

Chapter 5

Discussion

5.1 Future aspects of the 1 cm geoid experiment

Conclusions of 'the 1 cm geoid experiment' are currently published in the special issue 'Reference Systems in Physical Geodesy' (RSPG) of Journal of Geodesy. It should include all publications that are mentioned in this context in Chap. 4, whereby the current status (June 2020) of these publications is given in the following:

- P-IV was first submitted in November 2019 and was accepted after the second revision on July 1, 2020.
- The summary paper *Wang et al.* (in review) was initially submitted in April 2020 and is still in review.
- The publication *Liu et al.* (2020b) is in review since March 2020.
- The summary paper *Sánchez et al.* (in review) with the strategy for implementation of the IHRS was first submitted in May 2020 and is currently in review.
- *van Westrum et al.* (in review) was also submitted in May 2020 and is in review at the moment.

Several other publications in RSPG describe the solutions of other participating groups in detail, while their results and a short summary are also included in *Wang et al.* (in review) and *Sánchez et al.* (in review). *van Westrum et al.* (in review) describe the gathering and evaluation of high-quality measurements along GSVS17. After their publication, the analysis of high-quality measurements along GSVS17 should be used for further studies within the continuation of the 1 cm geoid experiment. Furthermore, the publication of high-quality measurements along GSVS17 would allow a more detailed analysis of the systematic effects in *Wang et al.* (in review). It should be possible to define a part of GSVS17 that is not affected by systematic effects, which allows the determination of an overall accuracy for regional gravity field determination in very challenging terrain. The availability of high-quality observations will additionally allow a better evaluation of the model-only solutions which are presented in Sect. 4.4.

Analysis of the 1 cm geoid experiment will be continued in a new JWG in the IAG period from 2019 to 2023. This JWG is called 'Error assessment of the 1 cm geoid experiment' and chaired by the author of this thesis. Its purpose is to further validate the computations, derive realistic error estimates, and determine and quantify possible error sources. Thereby, particular importance should be given to the separation of data-driven errors and method-driven errors, as the latter could significantly affect the calculation of IHRF stations. In general, the ability of a method to estimate an error budget for the computation of potential values is very important for the IHRS. Due to data restrictions, varying data quality and different local characteristics, the quality of IHRS stations will vary significantly around the globe. Accordingly, potential values of the IHRS should be accompanied with realistic accuracy estimations. The contribution of the 1 cm geoid experiment to the IHRS and a specific proposal for the implementation of this HSU are already included in the conclusions of P-IV, and will be further explained in *Sánchez et al.* (in review).

5.2 RLSC for the calculation of IHRF stations

The most general approach for the unification of (physical) height systems is the combination of GNSS measurements with a geoid model (Sect. 2.3, *Ihde et al.* 2017). In Sect. 2.4, three approaches are considered in order to calculate the geoid model regionally around an IHRF station. In the author's opinion, the combination of a high-resolution GGM with a refinement from local gravity observations is preferable for the realization of the IHRS (Sect. 2.4, case 3). This approach provides the most consistent solution globally, as all stations of the IHRS would include the same high-resolution GGM as reference model. Especially IHRF stations in regions close to the sea could benefit from this approach, as high-resolution GGMs generally provide a good quality over oceans. In these areas, regional gravity field determination from a satellite-only GGM (case 2) would have to consider altimetry on top of local gravity observations. This would make the calculation more complicated, and would most likely result in method-dependent differences for the calculation of IHRF stations around the world. Case 1, which is the derivation of potential values from model calculations alone, stays the easiest approach. However, it should be preferred only in cases, where no local gravity observations are available or the accuracy requirements are not too demanding.

RLSC provides consistent results for the refinement of a high-resolution GGM with local gravity field observations (P-IV). In the 1 cm geoid experiment, it performs among the best and most robust solutions of 13 independent calculations. For the introduction of an IHRS, we consider RLSC as beneficial, since it provides the probably most sophisticated error modeling among all the contributing methods of the 1 cm geoid experiment. The advantages of RLSC in terms of accuracy estimation are repeated in the following from P-III and P-IV:

- LSC, in general, allows the derivation of accuracy estimates from stochastic modeling, and can even provide full covariance information of all output quantities (e.g., P-III, Eq. 2). While

other approaches for regional gravity field estimation are sometimes not able to provide accuracy estimates, most of them are not able to calculate a full covariance matrix.

- RLSC models the accuracy of every input quantity and therefore includes all accuracy factors directly in its calculation (P-III). This is not always the case for regional gravity field estimations, as, for example, the reference model is often assumed as error free. Other LSC approaches that consider the accuracy of all relevant error contributions are listed in P-III.
- The RLSC approach allows a (partially) anisotropic and location-dependent modeling of the Earth's gravity field (P-III). This is enabled by the covariance information from a high-resolution GGM (e.g., XGM2016), which is calculated from regional varying weighting. *Pail et al.* (2010); *Sansò & Sideris* (2013) and *Haagmans & van Gelderen* (1991) include a similar advantage, but formulate it only for satellite-only GGMs, while P-III is the first formulation for high-resolution GGMs.
- RLSC allows the consideration of correlations between observations, which result, for example, from a low-pass filter in airborne gravimetry (P-IV). Thereby, P-IV presents the first inclusion of these correlations to a LSC-based calculation, as they are usually not taken into account in regional gravity field determination. In a combination between different data sets these correlations are of increased importance, as they influence the relative weighting between different data sets (e.g., terrestrial and airborne observations).
- Airborne observations generally contain a very high resolution in along-track direction. The direct one-step calculation in RLSC allows the full exploitation of this information for the combination of various data sets (P-IV). Other approaches which include a regular grid as intermediate step might lose the very high along-track resolution for their data combination.

We consider also two disadvantages for the calculation of IHRF stations with the present formulation. First, the computation of covariance matrices for RLSC, in general, but specifically their derivation from the high-resolution GGM, is very CPU-expensive (P-III, Sect. 5). However, with implementations for massive parallel computing, the computations are not necessarily time consuming in the absolute sense. Second, the estimation of output accuracies cannot automatically consider inconsistencies between different data sets. At the present stage, these accuracies depend significantly on the distribution of input observations (P-III, P-IV). Accordingly, an iterative RLSC approach would be able to calculate realistic input accuracies in a first step. In a second step, these estimated input accuracies, which for example consider inconsistencies between terrestrial and airborne data sources, are used in a second RLSC calculation. However, this disadvantage is not specific for LSC or RLSC, but a common problem in approaches for regional gravity field determination that provide an output accuracy.

A major focus of this thesis (P-III and P-IV) is on the improvement of regional gravity field determination by adapting LSC. However, also the enhancement of gravity observations or reduction models would lead to benefits in regional gravity field determination, and is therefore discussed in the following two sections.

5.3 The gravity models XGM2019e and EGM2020

In the 1 cm geoid experiment the RCR approach in RLSC is implemented with XGM2018 in combination with the topography-induced gravity model dV_ELL_Earth2014 and partially ERTM2160. Details of the reduction are described in P-IV (Sect. 4). This combination of dV_ELL_Earth2014 and XGM is considered as so useful that it is, by now, implemented in a new GGM. XGM2019e is a combination of dV_ELL_Earth2014 and the new XGM2019 (*Zingerle et al.*, 2020 accepted). It includes the updated satellite model GOCO06S (*Kvas et al.*, 2019), and is available in three different versions and resolutions (*Zingerle et al.*, 2019), which are described in *Zingerle et al.* (2020 accepted):

- XGM2019: includes no information of dV_ELL_Earth2014. Its spatial resolution is identical to XGM2016 and XGM2018. It combines GOCO06S and terrestrial data by applying full normal equation systems. For a calculation of potential values at IHRF stations, XGM2019 would be used for the covariance matrices $C_{\hat{s}\hat{s}}^m$, $C_{\hat{s}\hat{i}}^m$ and $C_{\hat{i}\hat{i}}^m$ (see P-III, Sect. 2.4).
- XGM2019e_2159: the resolution is identical to EGM2008. In P-IV, and possibly future IHRF calculations, this model could be used for the remove-compute-restore approach of terrestrial data in combination with ERTM2160.
- XGM2019e_5399: in its maximum resolution the XGM2019e is equivalent to a spatial resolution of 2', which equals approximately 4 km. This model is equivalent to the combination that was applied for the reduction of the airborne gravity measurements in P-IV.

Accordingly, XGM2019e would provide the following main benefits in a comparison to the reduction approach in P-IV:

- Improvements from the new satellite model GOCO06S.
- A more consistent transition zone around SH degree 719, where the high-resolution GGM and the topography-induced gravity model are combined. XGM2019e applies a direct combination of the normal equation systems of XGM2019 and dV_ELL_Earth2014, therefore providing a consistent solution even in the transition area.
- A simplified data reduction (P-IV, Sect. 4), as the topography-induced gravity model is included in the high-resolution GGM.

Additional changes to its predecessors (XGM2016, XGM2018) are also described in *Zingerle et al.* (2020 accepted). Further improvements of XGM2019e are planned as soon as improved terrestrial gravity observations are available, for example, from EGM2020. This long-awaited successor of EGM2008 is currently developed by the National Geospatial-Intelligence Agency (NGA). It will be provided in the same resolution as EGM2008, with a spatial resolution of approximately 10 km. In comparison to EGM2008, EGM2020 will benefit from new calculation procedures and extended gravity data sources. Especially the representation of the long-wavelength component of the Earth's gravity field improved significantly since the publication of EGM2008, mainly by the

satellite missions GRACE and GOCE (Sect. 2.2). Furthermore, several new acquisitions of gravity data (terrestrial, shipborne and airborne) as well as additional marine observations from altimetry will be included to EGM2020.

At one point, EGM2020 was planned for December 2019, but its publication prolonged and it is currently not announced for a specific date (June 2020). Although, the model is not available yet, it will likely be used as basis for the IHRS in the future. Since NGA has access to the world largest gravity data base, EGM2020 will probably be for the time being the best representation of the gravity field above satellite resolution. Accordingly, it makes sense to exploit the advantages of EGM2020 for the definition of the IHRS and the calculation of IHRF stations. EGM2020 cannot be included directly for RLSC, since it does not provide full variance-covariance information, and its normal equation system will not be published. However, the publication of EGM2020 will allow the calculation of a new XGM model, which would use the improved terrestrial data, and therefore also improve RLSC. Correspondingly, we conclude that RLSC will be able to build upon up-to-date GGM models even in the future.

5.4 Improvement of the GRAV-D processing

In the course of raw data analysis with GRAV-D observations at NGS, I have identified some possibilities for data improvement. The current version of the GRAV-D processing (Beta2, *GRAV-D Team* 2018a,b) applies a Gaussian low-pass filter to the absolute gravity measurements, thereby assuming a constant flight height in the observations. Although, the vertical movements of the aircraft are relatively small, they can easily affect the absolute gravity observation which changes with height. Consequently, the Gaussian low-pass filter should be applied to gravity disturbances δg (Sect. 2.1) rather than the absolute gravity g , as the normal gravity γ is a good approximation for gravity changes from height differences. Accordingly, the Gaussian low-pass filter would, in this case, not reduce high-frequency noise from vertical movement, but only high-frequency noise from the gravity instrument. Preliminary studies show, that low-pass filtered gravity disturbances are significantly smoother than gravity disturbances from the current GRAV-D processing.

Furthermore, the outlier detection in the current processing seems overcautious, as it eliminates more flight segments than necessary. This detection of outliers is implemented by a comparison of the GRAV-D observations with synthesized values from a GGM (Sect. 2.1). However, the GGM is realized with a SH model to degree 2190, therefore neglecting frequencies above. In the mountainous areas of the Rocky Mountains (e.g., Colorado) the gravity signal at flight height can easily exceed SH degree 2190. Accordingly, flight segments in these regions can be detected as outliers not because of incorrect measurements, but simply due to high-frequency gravity signal. In my opinion, the risk of incorrect outlier detection could be reduced, when it would be realized with a GGM to a higher SH degree (e.g., XGM2019e). In the GRAV-D block MS05 (*GRAV-D Team*,

2018b), which was used for the Colorado experiment, this approach would result in significantly less data gaps than the current processing.

Finally, the identification and calculation of offsets in individual flight lines of the GRAV-D project is not solved yet. In the beta2 version, GRAV-D measurements are tied to absolute gravity field measurements at the airfield. However, this approach often results in a significant bias of individual flight lines compared to a GGM. Possible alternatives are the correction of individual offsets directly from a GGM, or a crossover analysis between all flight lines of an observation block. In both cases, the calculation of the offset gets more robust, when the length of the flight line or respectively, the number of crossovers increases. Accordingly, both approaches would improve when offsets are not calculated individually for each flight line, but jointly for all flight lines between start and landing of the aircraft. An overview of these is available in *GRAV-D Team* (2018a).

All in all, the analysis of these aspects is not finished, but will be continued in strong cooperation with NGS.

Chapter 6

Conclusions

Regional gravity field determination in general and LSC methods in particular, use common simplifications for their calculation procedure. Accordingly, the gravity field of the Earth is often modeled as isotropic and homogeneous, although it is known that this is not true. Furthermore, correlations from a low-pass filter in airborne gravimetry are generally not considered in common gravity field modeling approaches. In this thesis, the new method called residual least-squares collocation considers a high-resolution GGM as anisotropic and location-dependent, and includes it in terms of a full variance-covariance matrix. Additionally, correlations resulting from a Gaussian low-pass filter in airborne gravimetry are handled consistently in the functional and stochastic model. Correspondingly, RLSC enables a more realistic accuracy estimation and provides an enhanced modeling of the Earth's gravity field. This makes RLSC a useful extension to already existing LSC methods, which could be applied for the calculation of potential values at IHRF stations.

Although, potential values at IHRF stations can be derived from high-resolution GGMs, this would generally not satisfy the accuracy requirements for the definition of an IHRS, mainly because of the remaining omission error. Accordingly, the calculation of IHRF stations should be based on regional gravity field determination on top of a GGM, which ensures global consistency. Therefore, a satellite-only GGM or a high-resolution GGM is refined with local gravity observations, and additionally supplemented with detailed information about topography-induced gravity effects. In this thesis, RLSC is proposed for regional gravity field determination, as it could provide substantial advantages for the calculation of IHRF stations.

RLSC is an adaption of already existing LSC approaches. RLSC models explicitly only residuals, whereby it uses error covariance matrices instead of the signal covariance matrices, which are applied in LSC. As a result, the method describes every input quantity with a corresponding covariance matrix, therefore providing error estimates that include all relevant contributions. For the first time, RLSC includes full variance-covariance information of a high-resolution GGM into a LSC-based calculation method. Furthermore, this thesis derives a concept for an optimal combination of a high-resolution GGM, terrestrial gravity observations and filtered airborne gravimetry. The results of RLSC are validated by a comparison to height anomalies from 12 other approaches of regional gravity field determination in the 1 cm geoid experiment. Thereby, RLSC provides reliable

height anomalies in a very challenging and mountainous test area. RLSC leads to the smallest standard deviation and the smallest peak-to-peak variation in a comparison to the mean reference along the GSVS17 benchmarks in Colorado. This is currently characterized as one of the most important validation tools for regional gravity field modeling methods in the 1 cm geoid experiment. In comparison to independent high-quality GNSS/leveling measurements, RLSC shows lower high-frequency variations than several other methods, but also systematic effects. However, these effects occur in a majority of the methods in the 1 cm geoid experiment, therefore indicating that they are not related to the RLSC procedure itself.

In general, the assessment of method-related differences in the 1 cm geoid experiment amounts for approximately 1 to 2 cm. Thereby, at least 0.5 cm of the differences, but more likely close to 1 cm, result from different relative weightings of input data. The combination of method-related and data-related errors is generally between 2.5 and 3.6 cm, when the high-quality measurements from the GSVS17 benchmarks are considered as reference. However, data-related errors are significantly increased by systematic effects, which will be analyzed in the current IAG period (2019-2023) as soon as the GSVS17 measurements are publicly available. Most likely, it will be possible to eliminate these systematic effects, or at least identify an area without them, so that the high-quality measurements along GSVS17 would provide a realistic quality assessment of all error sources in the 1 cm geoid experiment. Additionally, this would allow a better distinction between data-related and method-related differences.

In the end, results in the 1 cm geoid experiment should be evaluated by a combined comparison against the high-quality GNSS/leveling measurements along GSVS17, and the joint mean value of all solutions. Thereby, the comparison to high-quality measurements evaluates a method's general ability to calculate potential values with high accuracy. Especially in the high-frequency part of the gravity field, GNSS/leveling observations provide a very accurate validation. The comparison to the joint mean value ensures that different methods provide similar results when using identical data, which should guarantee a uniform IHRF system even when IHRF stations are calculated with different methods. Accordingly, methods that perform well in both validations prove their reliability and performance in a very challenging test case, and could generally be used for the calculation of IHRF stations. Apart from the evaluation of GSVS17 measurements, the continuation of the 1 cm geoid experiment will also resume the analysis of differences among the methods. Especially the handling of topography, the inclusion of airborne gravimetry and the separation term between geoid height and height anomaly are likely to be responsible for remaining differences in the results. The contribution of these aspects should be quantified, which will finally allow an even better unification of all methods.

To summarize, this thesis explains why the adaptations in RLSC provide more realistic error estimates than common LSC approaches. RLSC improves the calculation of gravity functionals by modeling an anisotropic and location dependent gravity field, and enables a direct combination of heterogeneous gravity data even considering the correlations from a low-pass filter. This work presents a determination and quantification of possible error sources in the 1 cm geoid exper-

iment, which will be intensified in the continuation of the JWG. While this thesis already evaluates advantages of the RLSC approach in order to derive realistic accuracy estimates, the continuation of the JWG will study this aspect for other methods of regional gravity field determination.

Bibliography

- Abd-Elmotaal HA (2017) Gravimetric geoid for Egypt implementing Moho depths and optimal geoid fitting approach. *Stud Geophys Geod*, 61: 657–674. doi 10.1007/s11200-015-1258-2
- Ågren J (2004) Regional Geoid Determination Methods for the Era of Satellite Gravimetry: Numerical Investigations Using Synthetic Earth Gravity Models. Dissertation, KTH Royal Institute of Technology. ISBN 91-7323-097-9
- Ågren J, Sjöberg LE, Kiamehr R (2009) The new gravimetric quasigeoid model KTH08 over Sweden. *Journal of Applied Geodesy*, 3(3): 143-153. doi 10.1515/JAG.2009.015
- Ågren J, Sjöberg LE (2014) Investigation of Gravity Data Requirements for a 5 mm-Quasigeoid Model over Sweden. In: Marti U. (eds) *Gravity, Geoid and Height Systems*. International Association of Geodesy Symposia, vol 141. Springer, Cham. doi 10.1007/978-3-319-10837-7_18
- Balasubramania N (1994) Definition and Realization of a Global Vertical Datum. Ohio State University, Department of Geodetic Science and Surveying, OSU Report No. 427
- Becker D (2016) Advanced Calibration Methods for Strapdown Airborne Gravimetry. Dissertation, Technical University of Darmstadt. ISBN 978-3-935631-40-2
- Bentel K, Schmidt M, Gerlach C (2013) Different radial basis functions and their applicability for regional gravity field representation on the sphere. *Int J Geomath*, 4: 67–96. doi 10.1007/s13137-012-0046-1
- Brockmann JM, Zehentner N, Höck E, Pail R, Loth I, Mayer-Gürr T, Schuh W-D (2014) EGM_TIM_RL05: An independent geoid with centimeter accuracy purely based on the GOCE mission. *Geophys Res Lett*, 41(22): 8089–8099. doi 10.1002/2014GL061904
- Bucha B, Janák J (2013) A MATLAB-based graphical user interface program for computing functionals of the geopotential up to ultra-high degrees and orders. *Computers & Geosciences*, 56: 186-196. doi 10.1016/j.cageo.2013.03.012
- Chambodut A, Panet I, Mandeau M, Diament M, Holschneider M, Jamet O (2005) Wavelet frames: An alternative to spherical harmonic representation of potential fields. *Geophys J Int*, 163(3): 875–899. doi 10.1111/j.1365-246X.2005.02754.x
- Childers VA, Bell RE, Brozena JM (1999) Airborne gravimetry: An investigation of filtering. *Geophysics*, 64(1): 61-69. doi 10.1190/1.1444530
- Colombo OL (1980) A World Vertical Network. Ohio State University, Department of Geodetic Science and Surveying, OSU Report No. 296
- Darbeshti N, Featherstone WE (2009) Non-stationary covariance function modelling in 2D least-squares collocation. *J Geod*, 83: 495–508. doi 10.1007/s00190-008-0267-0

- de Min E (1995) A comparison of Stokes' numerical integration and collocation, and a new combination technique. *Bull Géod*, 69: 223–232. doi 10.1007/BF00806734
- Drewes H, Kuglitsch F, Ádám J, Rózsa S (2016) The Geodesist's Handbook 2016. *J Geod*, 90: 907–1205. doi 10.1007/s00190-016-0948-z
- Drinkwater MR, Floberghagen R, Haagmans R, Muzi D, Popescu A (2003) GOCE: ESA's first Earth Explorer Core Mission. In: Beutler GB et al. (eds) *Earth Gravity Field from Space - from Sensors to Earth Sciences*, Space Sciences Series of ISSI, 17: 419–432, Springer, Dordrecht. doi 10.1007/978-94-017-1333-7_36
- Eicker A (2008) *Gravity Field Refinement by Radial Basis Functions from In-situ Satellite Data*. Dissertation, University of Bonn
- Fecher T, Pail R, Gruber T (2015) Global gravity field modeling based on GOCE and complementary gravity data. *International Journal of Applied Earth Observation and Geoinformation*, 35(A): 120-127. doi 10.1016/j.jag.2013.10.005
- Forsberg R, Tscherning CC (1981) The use of height data in gravity field approximation by collocation. *J Geophys Res*, 86(B9): 7843-7854. doi 10.1029/JB086iB09p07843
- Forsberg R, Olesen A, Bastos L, Gidskehaug A, Meyer U, Timmen L (2000) Airborne geoid determination. *Earth Planets Space*, 52: 863-866. doi 10.1186/BF03352296
- Forsberg R, Olesen AV, Einarsson I, Manandhar N, Shreshta K (2014) Geoid of Nepal from Airborne Gravity Survey. In: Rizos C, Willis P (eds) *Earth on the Edge: Science for a Sustainable Planet*. International Association of Geodesy Symposia, vol 139. Springer, Berlin. doi 10.1007/978-3-642-37222-3_69
- Freedon W, Gervens T, Schreiner M (1998), *Constructive Approximation on the Sphere: With Applications to Geomathematics*, Oxford Science Publications, Clarendon Press, ISSN 0198536828, ISBN 978-0-19-853682-6.
- Gerlach C (2003) *Zur Höhensystemumstellung und Geoidberechnung in Bayern*. Deutsche Geodätische Kommission, Reihe C, Nr. 571, Verlag der Bayerischen Akademie der Wissenschaften, München.
- Gerlach C, Fecher T (2012) Approximations of the GOCE error variance-covariance matrix for least-squares estimation of height datum offsets. *J Geodetic Sci*, 2(4): 247-256. doi 10.2478/v10156-011-0049-0
- Gerlach C, Rummel R (2013) Global height system unification with GOCE: a simulation study on the indirect bias term in the GBVP approach. *J Geod*, 87: 57–67. doi 10.1007/s00190-012-0579-y
- Gerlach C, Ophaug V (2017) Accuracy of Regional Geoid Modelling with GOCE. In: Vergos G, Pail R, Barzaghi R (eds) *International Symposium on Gravity, Geoid and Height Systems 2016*. International Association of Geodesy Symposia, vol 148. Springer, Cham. doi 10.1007/1345_2017_6
- GRAV-D Team (2018a) Block MS05 (Mountain South 05); GRAV-D Airborne Gravity Data User Manual. Youngman M, Johnson J (eds), Version BETA#2. Available May 4, 2020
- GRAV-D Team (2018b) Gravity for the Redefinition of the American Vertical Datum (GRAV-D) Project, Airborne Gravity Data; Block MS05. Available May 4, 2020
- Gruber T, Gerlach C, Haagmans R (2012) Intercontinental height datum connection with GOCE and GPS-levelling data. *J Geodetic Sci*, 2(4): 270–280. doi 10.2478/v10156-012-0001-y

- Gruber T, Rummel R, Ihde J, Liebsch G, Rülke A, Schäfer U, Sideris M, Rangelova E, Woodworth P, Hughes C, Gerlach C (2014) STSE - GOCE + Height System Unification with GOCE: Summary and Final Report. Doc No GO-HSU-RP-0021, issue 1.0, 25 Feb 2014.
- Haagmans RHN, van Gelderen M (1991) Error variances-covariances of GEM-TI: Their characteristics and implications in geoid computation. *J Geophys Res*, 96(B12): 20011-20022. doi 10.1029/91JB01971
- Heiskanen WA, Moritz H (1967) *Physical Geodesy*. W.H.Freeman and Company, San Francisco.
- Hirt C, Claessens S, Fecher T, Kuhn M, Pail R, Rexer M (2013), New ultrahigh-resolution picture of Earth's gravity field, *Geophys Res Lett*, 40(16): 4279-4283. doi 10.1002/grl.50838
- Hirt C, Kuhn M, Claessens S, Pail R, Seitz K, Gruber T (2014) Study of the Earth's short-scale gravity field using the ERTM2160 gravity model. *Computers & Geosciences*, 73: 71-80. doi 10.1016/j.cageo.2014.09.00
- Hirt C, Rexer M (2015) Earth2014: 1 arc-min shape, topography, bedrock and ice-sheet models - Available as gridded data and degree-10,800 spherical harmonics. *International Journal of Applied Earth Observation and Geoinformation*, 39: 103-112. doi 10.1016/j.jag.2015.03.001
- Hirt C, Yang M, Kuhn M, Bucha B, Kurzmann A, Pail R (2019) SRTM2gravity: An Ultrahigh Resolution Global Model of Gravimetric Terrain Corrections. *Geophys Res Lett*, 46: 4618–4627. doi 10.1029/2019GL082521
- Hofmann-Wellenhof B, Moritz H (2006) *Physical Geodesy*. Springer, Wien. ISBN-10 2-211-33544-7
- Holschneider M, Chambodut A, Manda M (2003) From global to regional analysis of the magnetic field on the sphere using wavelet frames. *Physics of the Earth and Planetary Interiors*, 135(2-3): 107-124. doi 10.1016/S0031-9201(02)00210-8
- Hwang C, Hsiao Y-S, Shih H-C, Yang M, Chen K-H, Forsberg R, Olesen AV (2007) Geodetic and geophysical results from a Taiwan airborne gravity survey: Data reduction and accuracy assessment. *J Geophys Res*, 112(B4), B04407. doi 10.1029/2005JB004220
- Ihde J, Augath W, Sacher M (2002) The Vertical Reference System for Europe. In: Drewes H, Dodson AH, Fortes LPS, Sánchez L, Sandoval P (eds) *Vertical Reference Systems*. International Association of Geodesy Symposia, vol 124. Springer, Berlin. doi 10.1007/978-3-662-04683-8_64
- Ihde J, Augath W (2002) The European Vertical Reference System (EVRS), Its relation to a World Height System and to the ITRS. In: Ádám J, Schwarz KP (eds) *Vistas for Geodesy in the New Millennium*. International Association of Geodesy Symposia, vol 125. Springer, Berlin. doi 10.1007/978-3-662-04709-5_14
- Ihde J, Sánchez L (2005) A unified global height reference system as a basis for IGGOS. *Journal of Geodynamics*, 40(4-5): 400–413, doi 10.1016/j.jog.2005.06.015
- Ihde J, Barzaghi R, Marti U, Sánchez L, Sideris M, Drewes H, Foerste C, Gruber T, Liebsch G, Pail R (2015) Report of the ad hoc group on an International Height Reference System (IHRS). In: Drewes H, Hornik H (eds) *Travaux de l'AIG 39, IAG Reports 2011–2015*
- Ihde J, Sánchez L, Barzaghi R, Drewes H, Foerste C, Gruber T, Liebsch G, Marti U, Pail R, Sideris M (2017) Definition and Proposed Realization of the International Height Reference System (IHRS). *Surv Geophys*, 38(3): 549-570. doi 10.1007/s10712-017-9409-3

- Krarup T (1969). A Contribution to the Mathematical Foundation of Physical Geodesy. In: Borre K (ed) *Mathematical Foundation of Geodesy - Selected Papers of Torben Krarup*. Springer, Berlin, 2006. doi 10.1007/3-540-33767-9
- Kutterer H, Neilan R, Bianco G (2012) Global geodetic observing system (GGOS). In: Drewes H, Kuglitsch F, Ádám J, Rózsa S (eds) *The geodesist's handbook 2012*. *J Geod*, 86(10): 915–926. doi 10.1007/s00190-012-0584-1
- Kvas A, Mayer-Gürr T, Krauss S, Brockmann JM, Schubert T, Schuh W-D, Pail R, Gruber T, Jäggi A, Meyer U (2019) The satellite-only gravity field model GOCO06s. *GFZ Data Services*. doi 10.5880/ICGEM.2019.002
- Li X (2011) Strapdown INS/DGPS airborne gravimetry tests in the Gulf of Mexico. *J Geod*, 85: 597-605. doi 10.1007/s00190-011-0462-2
- Lieb V, Schmidt M, Dettmering D, Börger K (2016) Combination of various observation techniques for regional modeling of the gravity field. *J Geophys Res Solid Earth*, 121(5): 3825-3845. doi 10.1002/2015JB012586
- Lieb V (2017) Enhanced regional gravity field modeling from the combination of real data via MRR. Dissertation, Technical University of Munich
- Liu Q, Schmidt M, Pail R, Willberg M (2020a) Determination of the Regularization Parameter to Combine Heterogeneous Observations in Regional Gravity Field Modeling. *Remote Sens*, 12(10), 1617. doi 10.3390/rs12101617
- Liu Q, Schmidt M, Sánchez L, Willberg M (2020b) Regional gravity field refinement for (quasi-) geoid determination based on spherical radial basis functions in Colorado. *J Geod*, 94, 99. doi 10.1007/s00190-020-01431-2
- McCubbine JC, Amos MJ, Tontini FC, Smith E, Winefield R, Stagpoole V, Featherstone WE (2018) The New Zealand gravimetric quasigeoid model 2017 that incorporates nationwide airborne gravimetry. *J Geod*, 92: 923–937. doi 10.1007/s00190-017-1103-1
- Migliaccio F, Reguzzoni M, Gatti A, Sansò F, Hecceg M (2011) A GOCE-only global gravity field model by the space-wise approach. In: *Proceedings of the 4th International GOCE User Workshop*. ESA SP-696.
- Moritz H (1980) *Advanced Physical Geodesy*. Herbert Wichmann, Karlsruhe. ISBN 3-87907-106-3
- Moritz H (2000) Geodetic Reference System 1980. *J Geod*, 74: 128-133. doi 10.1007/s001900050278
- Olesen AV (2003) Improved airborne scalar gravimetry for regional gravity field mapping and geoid determination. Dissertation, Faculty of Science, University of Copenhagen
- Ophaug V, Gerlach C (2017) On the equivalence of spherical splines with least-squares collocation and Stokes's formula for regional geoid computation. *J Geod*, 91: 1367–1382. doi 10.1007/s00190-017-1030-1
- Pail R, Reguzzoni M, Sansò F, Kühtreiber N (2010) On the combination of global and local data in collocation theory. *Stud Geophys Geod*, 54(2): 195-218. doi 10.1007/s11200-010-0010-1
- Pail R, Fecher T, Barnes D, Factor JF, Holmes SA, Gruber T, Zingerle P (2018) Short note: the experimental geopotential model XGM2016. *J Geod*, 92(4): 443-451. doi 10.1007/s00190-017-1070-6

- Pavlis NK, Holmes SA, Kenyon SC, Factor JK (2012) The development and evaluation of the Earth Gravitational Model 2008 (EGM2008). *J Geophys Res*, 117, B04406. doi 10.1029/2011JB008916
- Petit G, Luzum B (2010) IERS Conventions (2010). Frankfurt: Bundesamt für Kartographie und Geodäsie, IERS Technical Note No. 36, ISBN 3-89888-989-6
- Rapp R, Balasubramania N (1992) A Conceptual Formulation of a World Height System. Ohio State University, Department of Geodetic Science and Surveying, OSU Report No. 421
- Rexer M, Hirt C, Claessens S, Tenzer R (2016) Layer-Based Modelling of the Earth's Gravitational Potential up to 10-km Scale in Spherical Harmonics in Spherical and Ellipsoidal Approximation. *Surv Geophys*, 37(6): 1035-1074. doi 10.1007/s10712-016-9382-2
- Rexer M (2017) Spectral Solutions to the Topographic Potential in the context of High-Resolution Global Gravity Field Modelling. Dissertation, Technical University of Munich
- Rieser D (2015) GOCE gravity gradients for geoid and Moho determination applying the Least Squares Collocation approach. Dissertation, Graz University of Technology
- Rülke A, Liebsch G, Sacher M, Schäfer U, Schirmer U, Ihde J (2012) Unification of European height system realizations. *J Geodetic Sci* 2(4): 343-354. doi 10.2478/v10156-011-0048-1
- Rummel R, Teunissen P (1988) Height datum definition, height datum connection and the role of the geodetic boundary value problem. *Bull Géod*, 62: 477–498. doi 10.1007/BF02520239
- Rummel R (2001) Global Unification of Height Systems and GOCE. In: Sideris MG (eds) Gravity, Geoid and Geodynamics 2000. International Association of Geodesy Symposia, vol 123. Springer, Berlin. doi 10.1007/978-3-662-04827-6_3
- Rummel R (2012) Height unification using GOCE. *J Geodetic Sci* 2(4): 355-362. doi 10.2478/v10156-011-0047-2
- Sánchez L (2012) Towards a vertical datum standardisation under the umbrella of Global Geodetic Observing System. *J Geodetic Sci*, 2(4): 325-342. doi 10.2478/v10156-012-0002-x
- Sánchez L, Čunderlík R, Dayoub N, Mikula K, Minarechová Z, Šíma Z, Vatrt V, Vojtíšková M (2016) A conventional value for the geoid reference potential W_0 . *J Geod*, 90(9): 815–835. doi 10.1007/s00190-016-0913-x
- Sánchez L, Sideris MG (2017) Vertical datum unification for the International Height Reference System (IHRM). *Geophys J Int*, 209(2): 570-586. doi 10.1093/gji/ggx025
- Sánchez L, Ågren J, Huang J, Wang YM, Mäkinen J, Pail R, Barzaghi R, Vergos GS, Ahlgren K, Liu Q (SUBMITTED, 2020) Strategy for the implementation of the International Height Reference System (IHRM). *J Geod*.
- Sandwell DT, Smith WHF (2009) Marine gravity anomaly from Geosat and ERS 1 satellite altimetry. *J Geophys Res*, 102(B5): 10039–10054. doi 10.1029/96JB03223
- Sansò F, Sideris MG (eds) (2013) Geoid Determination: Theory and Methods. Springer, Heidelberg. doi 10.1007/978-3-540-74700-0

- Schmidt M, Fabert O, Shum CK (2005) On the estimation of a multi-resolution representation of the gravity field based on spherical harmonics and wavelets. *Journal of Geodynamics*, 39(5): 512-526. doi 10.1016/j.jog.2005.04.007
- Schmidt M, Fengler M, Mayer-Gürr T, Eicker A, Kusche J, Sánchez L, Han S-C (2007) Regional gravity modeling in terms of spherical base functions. *J Geod*, 81: 17–38. doi 10.1007/s00190-006-0101-5
- Simons FJ (2010) Slepian Functions and Their Use in Signal Estimation and Spectral Analysis. In: Freedon W, Nashed MZ, Sonar T (eds) *Handbook of Geomathematics*. Springer, Berlin. doi 10.1007/978-3-642-01546-5_30
- Sünkel H (1981) Point Mass Models and the Anomalous Gravitational Field. Ohio State University, Department of Geodetic Science and Surveying, OSU Report No. 328
- Tapley BD, Bettadpur S, Watkins M, Reigber C (2004) The gravity recovery and climate experiment: Mission overview and early results. *Geophys Res Lett*, 31(9), L09607. doi 10.1029/2004GL019920
- Torge W (2003). *Geodäsie*. De Gruyter, Berlin. ISBN 3-11-017545-2
- Tscherning CC, Rapp RH (1974) Closed Covariance Expressions for Gravity Anomalies, Geoid Undulations, and Deflections of the Vertical Implied by Anomaly Degree Variance Models. Ohio State University, Department of Geodetic Science and Surveying, OSU Report No. 208
- Tscherning CC (1999) Construction of anisotropic covariance functions using Riesz-representers. *J Geod*, 73(6): 332-336. doi 10.1007/s001900050250
- Tscherning CC (2015) Least-Squares Collocation. In: Grafarend E (ed) *Encyclopedia of Geodesy*. Springer, Cham. doi 10.1007/978-3-319-02370-0_51-1
- van Westrum D, Ahlgren K, Hirt C, Guillaume S (SUBMITTED, 2020) A Geoid Slope Validation Survey (2017) in the Rugged Terrain of Colorado, USA. *J Geod*.
- Wang YM, Sánchez L, Ågren J, Huang J, Forsberg R, Abd-Elmotaal HA, Barzaghi R, Bašić T, Carrion D, Claessens S, Erol B, Erol S, Filmer M, Grigoriadis VN, Isik MS, Jiang T, Koç O, Li X, Ahlgren K, Krčmaric J, Liu Q, Matsuo K, Natsiopoulos DA, Novák P, Pail R, Pitoňák M, Schmidt M, Varga M, Vergos GS, Véronneau M, Willberg M, Zingerle P (SUBMITTED, 2020) Report on the 1-cm geoid experiment in Colorado. *J Geod*.
- Wei M, Schwarz KP (1998) Flight test results from a strapdown airborne gravity system. *J Geod*, 72(6): 323-332. doi 10.1007/s001900050171
- Zingerle P, Pail R, Gruber T, Oikonomidou X (2019) The experimental gravity field model XGM2019e. GFZ Data Services. doi 10.5880/ICGEM.2019.007
- Zingerle P, Pail R, Gruber T, Oikonomidou X (ACCEPTED, 2020) The combined global gravity field model XGM2019e. *J Geod*. doi 10.1007/s00190-020-01398-0

Acknowledgments

I would like to thank those who were kind enough to support me in writing this thesis and helped me with my scientific endeavors in one way or another. My warmest thanks to Roland Pail for all the time he spent guiding me, for his helpful ideas and for giving me the possibility to write this work in the first place. Special thanks to Michael Schmidt - our discussions have always been very helpful, and more than once he has pointed out aspects I might have paid insufficient attention to. Many thanks to Jonas Ågren for the rare but enjoyable times we met each other and for taking the time to evaluate this thesis. I would also like to thank Thomas Gruber for introducing me to the topic, for his constant support especially in the early years of my work and for his help with my questions of scientific as well as organizational nature.

Many thanks to all current and former colleagues at IAPG, who have been of significant help during these years. I am grateful that I have always found someone capable of answering my questions, for the numerous discussions in both my own and related research areas, the technical support, the great time we had together and the variety and distraction, which I encountered every day. Special thanks goes to Philipp Zingerle who should be specifically addressed regarding all the points just mentioned and to Christoph Gisinger, my valuable teacher, who introduced me to 'scientific work'. I would like to thank Reiner Rummel for the meaningful discussions and for being my living library when I was searching for literature. Many thanks to Verena Lieb and Qing Liu for providing me with the required insights into a related method and the very good cooperation in general.

Special gratitude also goes to George Vergos and his colleagues - they have been wonderful hosts during my trips to Thessaloniki and working with them has been a great pleasure as well as a valuable educational experience. For my invitation to Washington D.C. I thank Steve Hilla and Yan Wang, and I would like to thank them and their colleagues for the unique experience I had at NGS.

Finally, I would like to thank my family and my girlfriend Elena for always believing in me more than I ever could myself. I am very grateful for the constant support in all aspects of my life.

Appendix A

P.1 Publication I: Analysis of GOCE Omission Error and its Contribution to Vertical Datum Offsets in Greece and its Islands

Reference

Willberg M., Gruber T., Vergos G. (2017) Analysis of GOCE Omission Error and Its Contribution to Vertical Datum Offsets in Greece and Its Islands. In: Vergos G., Pail R., Barzaghi R. (eds) International Symposium on Gravity, Geoid and Height Systems 2016. International Association of Geodesy Symposia, vol 148. Springer, Cham. doi 10.1007/1345_2017_3

Copyright

This work originally has been published in International Association of Geodesy Symposia, available at <https://link.springer.com/>, and is reprinted here with permissions of Springer. The copyright has been transferred to Springer International Publishing AG.

Abstract

In this paper we evaluate three different geoid models (a pure and an extended satellite-only model and a local geoid solution) for the mainland of Greece and fourteen of its biggest islands in terms of signal content and applicability for height system unification. By comparing local geoid heights from GNSS and spirit leveling with the three geoid models it is possible to make statements about the Earth's gravity signal that is omitted in these models (omission error). In a further step we try to quantify the contribution of the omission error to the height system unification between the investigated islands. It becomes obvious that a satellite-only gravity field model (GOCO05S) until degree and order 200 is not sufficient for the mountainous islands of Greece due to an omission error of up to 2 m. The same model with high frequency corrections from EGM08 as well as topography is able to reduce the omission error drastically and shows similar results as for the local geoid model. As an outcome, we can see homogeneous omission errors for the smaller islands and in general a high correlation between the size of the island and the amplitudes of the omission error.

Declaration of own contribution

(MW: Martin Willberg; TG: Thomas Gruber; GV: Georgios S. Vergos)

The original idea for the study was proposed by TG and GV. The study design was then developed by MW with the help of TG and GV. MW calculated geoid solutions from the two global geopotential models with the support of TG, thereby applying also software that was developed by TG. GV provided the local Hellenic geoid model. MW is responsible for the results, the analysis and the interpretation. Furthermore, MW formulated the text with corrections from TG and GV. MW created the figures.

The overall own contribution of MW for *P-I* is estimated at 83 %, which is the average value of the percentage values estimated for the six criteria listed in the table below (Tab. P.1).

Criteria	Estimated own contribution
Computation and results	85 %
Ideas and study design	50 %
Analysis and interpretation	90 %
Text	90 %
Figures	100 %
Tables	-
Total	83 %

Tab. P.1 – Criteria and estimated contribution share of Martin Willberg for *P-I*


Confirmation by the authors

We hereby confirm the correctness of the declaration of own contribution for the publication

Willberg M., Gruber T., Vergos G. (2017) Analysis of GOCE Omission Error and Its Contribution to Vertical Datum Offsets in Greece and Its Islands. In: Vergos G., Pail R., Barzaghi R. (eds) International Symposium on Gravity, Geoid and Height Systems 2016. International Association of Geodesy Symposia, vol 148. Springer, Cham. doi: https://doi.org/10.1007/1345_2017_3

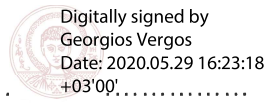
Thomas Gruber

Institute for Astronomical and Physical Geodesy, Technical University of Munich, Germany

Signature:  Date: *15-5-2020*

Georgios Vergos

GravLab, Department of Geodesy and Surveying, Aristotle University of Thessaloniki, Greece

Signature: **Georgios Vergos**  Date:

Digitally signed by
Georgios Vergos
Date: 2020.05.29 16:23:18
+03'00'



Analysis of GOCE Omission Error and Its Contribution to Vertical Datum Offsets in Greece and Its Islands

Martin Willberg, Thomas Gruber, and Georgios S. Vergos

Abstract

In this paper we evaluate three different geoid models (a pure and an extended satellite-only model and a local geoid solution) for the mainland of Greece and fourteen of its biggest islands in terms of signal content and applicability for height system unification. By comparing local geoid heights from GPS and spirit levelling with the three geoid models it is possible to make statements about the Earth's gravity signal that is omitted in these models (omission error). In a further step we try to quantify the contribution of the omission error to the height system unification between the investigated islands. It becomes obvious that a satellite-only gravity field model (GOCO05S) until degree and order 200 is not sufficient for the mountainous islands of Greece due to an omission error of up to 2 m. The same model with high frequency corrections from EGM08 as well as topography is able to reduce the omission error drastically and shows similar results as for the local geoid model. As an outcome, we can see homogenous omission errors for the smaller islands and in general a high correlation between the size of the island and the amplitudes of the omission error.

Keywords

GOCE • Height systems • Local vertical datum • Omission error

1 Introduction and Problem Definition

The connection and unification of height systems has been identified as one of the most important tasks in physical geodesy. The International Association of Geodesy (IAG) accommodated this and issued a resolution about the establishment of an International Height Reference System (IHRIS) (Drewes et al. 2016). The basis of height system unification is a globally consistent Earth gravity field as

it is observed by the Gravity field and steady-state Ocean Circulation Explorer mission (GOCE) satellite (Drinkwater et al. 2003) in combination with other satellite information as it is provided by the Gravity Recovery And Climate Experiment mission (GRACE) (Tapley et al. 2004). It has been proven that GRACE/GOCE based Earth gravity field models deliver the static part of the geoid with an accuracy of 1–2 cm at spatial scales of 100 km and larger (Brockmann et al. 2014). Still missing are geoid signals with smaller spatial resolution, which cannot be observed by satellites due to their distance from the Earth surface. This is the so-called omission error, which plays an important role in height system unification and is the major topic of this paper.

We investigate the possibility to account for the omission error (or in other words the omitted signal) in a satellite-only gravity field model depending on local characteristics at the evaluation points (e.g. availability of gravity observations, terrain roughness, land-ocean transition). We regard three possible approaches: (1) The omission error

M. Willberg (✉) • T. Gruber
Institute of Astronomical and Physical Geodesy, Technical University of Munich, Munich, Germany
e-mail: martin.willberg@tum.de; thomas.gruber@tum.de

G.S. Vergos
GravLab, Department of Geodesy and Surveying, Aristotle University of Thessaloniki, Thessaloniki, Greece
e-mail: vergos@topo.auth.gr

is neglected at all, assuming that no surface gravity data is available. (2) The omitted signal is estimated from a global high resolution gravity field model incorporating surface and altimetry-derived gravity data, e.g. the EGM2008 model (Pavlis et al. 2012, 2013), and topography-induced gravity field information (confer Hirt et al. 2010). (3) A regional geoid model (Grigoriadis 2009) based on a satellite model and terrestrial/altimetry gravity data is used, assuming that this model contains the full gravity signal. The results obtained from these three approaches are finally compared to independent geoid heights as they are derived from GPS and spirit levelling. This will allow us to gain accuracy estimates about the incorporated data sets and/or the estimation of the omission error at each individual point investigated. Finally, the impact of the omission error on offsets between different height systems can be quantified as well.

With its hundreds of islands Greece is an ideal test area for such analyses. The mainland of Greece and the islands have numerous different (orthometric) height systems, also known as locally realised vertical datums, which have never been connected through hydrostatic levelling. Most of the islands show large topographic effects and the omission error frequently lies far above the global average of about three decimetres as it is determined from standard degree variance models (Gruber et al. 2011, 2014). Furthermore, the islands in the Aegean and Ionian Sea have already been subject to several studies about the geopotential value W_0 and the height offsets (Kotsakis et al. 2012; Grigoriadis et al. 2014). These can be complemented with the different aspects of this analysis. The origin of the Hellenic Vertical Datum is defined by the tide gauge station in Piraeus harbour near Athens, but only the mainland of Greece is connected to this official vertical datum. All islands have their own vertical datum installed by the Hellenic Military Geographic Service between 1963 and 1986 according to the local mean sea level at one point respectively (Grigoriadis et al. 2014).

The situation between various islands is exemplified by two different vertical height systems and an ocean in between (Fig. 1). The following description is a summary of Gruber et al. (2012), but adapted to the situation in Greece. As orthometric heights are chosen as height coordinates in Greece we stick to these in the following analyses, but all conclusions are applicable to normal heights as well. For more details about height systems, geoid determination from spherical harmonics, or regional approaches we refer to Heiskanen and Moritz (1967).

Local height systems are defined by the local equipotential surface through the origin of the vertical system, which in most cases is set to the observed mean sea level at one point at the coast (e.g. tide gauge) (brown solid line). Orthometric heights (brown dotted lines) can then be transferred from the origin to every other point on the Earth surface by spirit levelling and gravimetry.

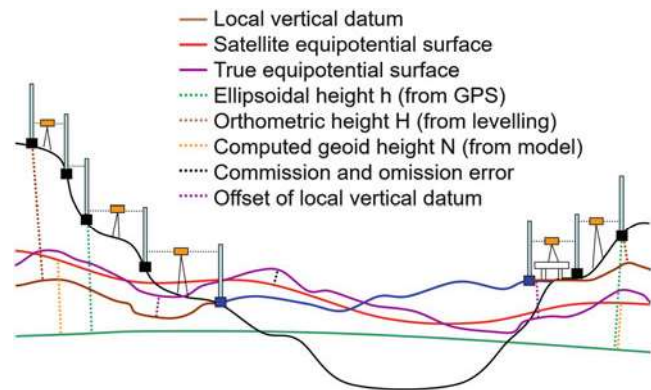


Fig. 1 Overview of different heights and reference surfaces as used in this paper. Adapted from Gruber et al. (2012)

With the combination of ellipsoidal heights determined from GPS (green dotted lines) and in case of error-free orthometric heights one can compute the height of the local equipotential surface above the reference ellipsoid, which is named local geoid throughout the paper. But neither the local geoid height nor the orthometric height can be compared between different height systems, because of different origins in the vertical datum (Fig. 1). Satellite based global gravity field models are able to deliver a globally consistent equipotential surface (red solid line), but as explained above this still differs from the true equipotential surface (purple solid line) due to the commission and omission error (black dotted line).

The paper is structured as follows: Sect. 2 describes the different data sets used in this study. After that, we present the procedures and their results for three different geoid models with a special emphasis on the accuracies of each model in Sect. 3 and the influence of these accuracies on height systems in Sect. 4. The final Sect. 5 summarizes the results and provides some conclusions.

2 Data Sets Used for the Study

For the evaluation we need geoid information from a Global Gravity Model (GGM) based on GOCE, a local geoid calculation based on terrestrial gravimetry information and GPS/levelling data, which we use to check our three approaches at selected stations. Of all the Greek islands we select only those with twelve or more GPS/levelling stations available for our study. In addition, we include data from the Greek mainland. The procedure itself is not limited to the chosen islands, but a minimum number of GPS/levelling stations helps to derive conclusive results. A map with the 14 selected islands (Andros, Chios, Corfu, Crete, Eyvoia, Karpathos, Kefalonia, Kos, Lesvos, Limnos, Naxos, Rhodes, Samos and Zakyntos) can be found in Sect. 4 (Fig. 3).

2.1 Geoid Solutions from Global Model

With GOCO05S we use a state-of-the-art satellite-only GGM based on all data from the GRACE and GOCE missions (Mayer-Gürr and GOCO Team 2015). Comparisons to other combined GGMs (EGM2008, GOCO05C) show that it has full signal content approximately up to degree 200–220. Therefore, using this model up to degree and order 200, assuming that no terrestrial data is available, is a good starting point for our initial analysis (confer case 1 in the introduction). For case 2 the omitted signal is approximated in two steps: first, by adding the EGM2008 model geoid from degree 201 to degree 2190, and second, by adding the geoid impact computed from a Residual Terrain Model (RTM) above the resolution of EGM2008. A more detailed description of the general approach of using a GGM in order to estimate the omission error can be found in Gruber et al. (2011).

2.2 Local Hellenic Geoid Model

The Hellenic Geoid Model 2009 (HGM2009) was derived from a thoroughly validated gravity database, which contains terrestrial data for land and sea areas as well as satellite altimetry derived gravity anomalies. The HGM2009 was estimated by employing the spherical Stokes kernel and the 1D spherical FFT approach (Haagmans et al. 1993). Regarding the necessary reductions, the EGM96 (Lemoine et al. 1998) was chosen as the geopotential reference model, while a Digital Terrain and Bathymetry Model, obtained from the combination of SRTM3 (Farr et al. 2007) and SRTM30-Plus (Becker et al. 2009), was used for computing the terrain corrections.

2.3 GPS-Levelling Data

The GPS measurements used in this paper originate from a nation-wide campaign carried out in 2007 and their resulting height accuracy is given as 2–5 cm (Vergos et al. 2014). The orthometric heights were measured by spirit and/or precise trigonometric levelling long before the GPS measurements were taken and their precision at that time was given as approximately 1–2 cm. Nevertheless, their true precision remains unknown, because the levelling was not accompanied by local gravimetric ground measurements; instead, interpolated values from free air anomaly maps were used (Kotsakis et al. 2012). This results in a hardly quantifiable error due to nonparallel equipotential fields. For this reason, the levelling data represent the most problematic data set used in our study.

3 Omission Error Analysis

For the omission error analysis, we compare the geoid solutions of the three mentioned cases with the local geoid height which we get from GPS-levelling by subtracting the orthometric height H from the ellipsoidal height h (compare Fig. 1). This is done for every point i with GPS/levelling observations by the difference

$$\Delta N_i = N_i - (h_i - H_i), \quad (1)$$

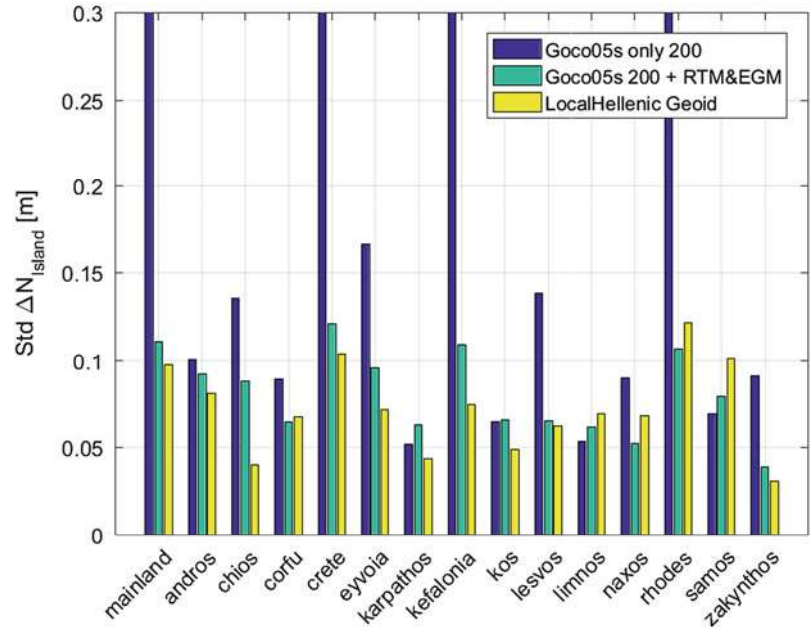
where N_i is the selected geoid solution. As the geoid model N and the orthometric height H in general refer to different equipotential reference surfaces there is a height offset in ΔN . It is assumed that the GPS/levelling observations contain the full signal of the Earth gravity field, so the omission error of our geoid models N completely transfers to ΔN along with random and systematic errors in all three quantities involved. Systematic errors can occur due to geometrical distortions in the levelling network, long or medium wavelength effects in the geoid model, datum inconsistencies between geoid and ellipsoidal heights and unmodeled time-dependent variations (Kotsakis et al. 2012). For analyzing the omission error, we eliminate the constant offset and the systematic distortion from the observations by a planar fit to ΔN and by subtracting this plane from the differences.

$$\Delta N_i^{\text{corrected}} = N_i - (h_i - H_i) - \Delta N^{\text{correctionSurface}} \quad (2)$$

We do not apply a higher order correction surface as this could partially remove the omitted signal as well. Because there are outliers in the GPS/levelling data we also apply a simple 2σ criterion during the data processing, which eliminates about 5% of our observation points. Also, these outliers were not used for further analyses.

After removing the offset and the systematic distortions, the random errors as well as the omission errors remain in $\Delta N_i^{\text{corrected}}$ and can be interpreted for our three test cases. As we are not interested in single point differences we use the standard deviations over a target area (island or mainland Greece respectively) to evaluate geoid differences (Fig. 2). When we neglect the observation errors of GPS and levelling for a moment and assume that the estimation of the correction plane removes systematic distortions, then in cases 1 and 2 the remaining $\Delta N_i^{\text{corrected}}$ gives us the sum of omission and commission error of our geoid model N determined from spherical harmonics. In case 3, in contrast, $\Delta N_i^{\text{corrected}}$ shows mainly modelling errors in the local Hellenic Geoid. According to a variance-covariance propagation of the GOCO05S model, the commission error in Greece accounts for about 1.6 cm.

Fig. 2 Standard deviation of $\Delta N_i^{\text{corrected}}$ for the three different geoid models: case 1 (blue), case 2 (green) and case 3 (yellow). All bars are presented after parameter estimation of a plane and outlier removal by a 2σ criterion. *Cutted bars* show 48 cm for the mainland, 64 cm for Crete, 39 cm for Kefalonia and 33 cm for Rhodes



The standard deviations in case 1 range from 5 to 65 cm and are much higher than in the other cases (Fig. 2) because all gravity field signals above degree 200 are neglected. In both the second and the third case our extreme values account from 3 to 4 cm to about 12 cm; thereby the local Hellenic geoid in case 3 generally provides slightly better results.

As expected, case 1 shows by far the worst results, though there are islands (Karpathos, Limnos and Samos) where case 1 performs slightly better than case 2. In general, it can be seen that large islands, respectively islands with a higher number of measurement points, tend to show higher omission errors here.

Of course our simplification with error-free observations is not true and, in fact, we already know that our GPS/levelling observations were not optimally done. The visualized difference in Fig. 2 shows (in all 3 cases) random errors due to the observation accuracy of GPS and spirit levelling and therefore the omission error (cases 1 and 2) and the modelling errors (case 3) of the high frequency signal are even below the values presented in Fig. 2. As a conclusion, the approach in case 2, where we calculate the geoid heights N only by using a global satellite model, point positions, and EGM08 coefficients as input, shows almost the same performance as the far more complex local geoid calculation.

4 Height System Offsets Between Islands

In Sect. 3 we used the comparison of the selected geoid models to the local geoid from GPS/levelling to evaluate the accuracy of our models at selected islands. Now we take

the geoid model differences ΔN again, but do not subtract the correction surface resulting in absolute geoid height offsets ΔN^{mean} for every island. This is done by calculating the mean value over Eq. (1), where n is the number of observation points per island:

$$\Delta N^{\text{mean}} = \Sigma (N_i - (h_i - H_i)) / n \quad (3)$$

These ΔN^{mean} values per island represent the mean offset of the Local Vertical Datum (LVD) to the geoid model N and enable the connection of different vertical datums. As in general, there are no well observed tide gauge stations on the Greek islands; it is considered to be more accurate to use mean values over the whole island instead of single reference points (e.g. tide gauges) for the offsets of the LVD. However, with this consideration it is not possible to compare heights between two individual points of different vertical datums as the offsets stay unknown.

In Fig. 3 the offsets of the LVD are visualized for every island and the mainland in case 1 (upper value) and case 2 (lower value). While in case 1 the offsets have a wide distribution from -243 to $+25$ cm, they range from -38 to $+13$ cm in case 2. Almost all of the offsets are negative which means that the LVD for that island is below the used geoid model.

In Sect. 3 we showed that the GOCO05S model performs much better when adding high frequency parts from EGM and RTM information. This allows us to calculate the omission error in case 1 by using the more accurate case 2 results as reference. The omission error of GOCO05S up to degree and order 200 is then a simple difference of the two values in Fig. 3. Regarding the islands, it varies from about 8 cm for



Fig. 3 Mean offset of GOCO05s and extended GOCO05s geoid models to point-wise GPS-levelling observations. The two values give the mean offset of the LVD when calculating the model with EGM and RTM above degree 200 (case 2, bottom value) and without them (case 1, upper value)

Lesvos to almost 2 m for Rhodes. Most of the islands show omission errors far above the average of 30 cm, while the impact for the mainland is much smaller (3 cm). The reason is the small size of the islands compared to the resolution of GOCE (about 100 km for degree 200). Even the biggest island, Crete, has only an extension of up to 55 km in the north-south direction. When a target area is smaller than the resolution of GOCE the satellite-only gravity field is not able to calculate a representative mean value (especially when there is variable topography) and this can result in increased omission errors (Fig. 3).

The bottom values in Fig. 3 are then used for the computation of height offsets between the data sets (islands and mainland) as shown in Fig. 4. The offsets of the LVD in case 2 are presented as absolute values of the pairwise differences which gives us a 15 × 15 matrix where the colour indicates the height system offset between two data sets. The result is a symmetric matrix with values up to 50 cm with the maximum being the result of the difference between the highest and the lowest offset (Corfu and Rhodes). Dark blue values show data sets with similar offsets of the vertical datum while brighter values (e.g. column or line of Rhodes) indicate that a LVD has a large discrepancy to the others. Pairwise differences provide an easy way

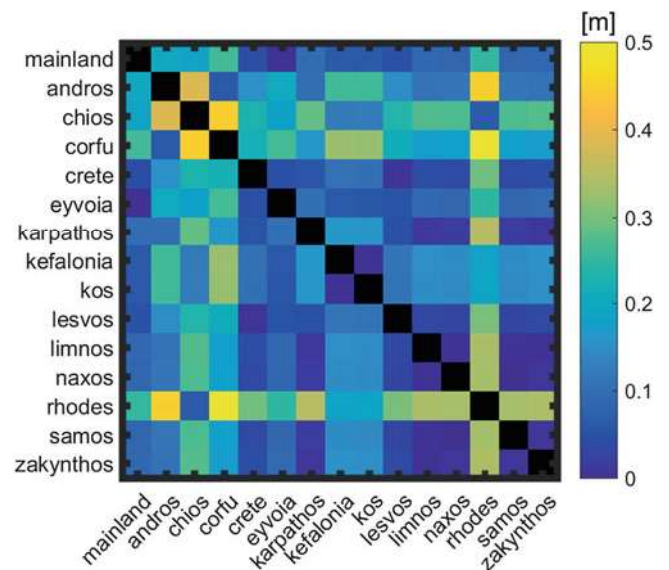


Fig. 4 Pairwise difference of the height offset between chosen islands/mainland. Calculation based on the GOCO05S model with EGM & RTM (case 2)

for height system unification to visualize height systems offsets.

5 Summary and Conclusions

When combining the results from Sects. 3 and 4 it becomes clear that a satellite-only model (case 1) is not suitable to calculate geoid heights for the Greek islands. The small size of the islands leads to large omission errors because GOCE is not able to distinguish the island from the surrounding sea. However, the omission error for the smaller islands (all except Crete, Rhodes, Kefalonia) is homogenous and similar to all points on the island, which can be seen by the small standard deviations in Fig. 2.

Case 2 shows in both investigations large differences compared to case 1, which again demonstrates that the gravity field signal above degree 200 should not be neglected. The big differences between the smaller and the bigger islands in case 1 are reduced though not eliminated in case 2 when using the GOCO05S model with EGM and RTM information. And the geoid differences are quite similar between cases 2 and 3, which is a good indicator that a satellite-only model with corrections is able to adapt to local characteristics.

References

- Becker JJ et al (2009) Global bathymetry and elevation data at 30 arc seconds resolution: SRTM30_PLUS. *Mar Geodesy* 32(4):355–371. doi:[10.1080/01490410903297766](https://doi.org/10.1080/01490410903297766)
- Brockmann JM, Zehentner N, Höck E, Pail R, Loth I, Mayer-Gürr T, Schuh W-D (2014) EGM TIM RL05: an independent geoid with centimeter accuracy purely based on the GOCE mission. *Geophys Res Lett* 41(22):8089–8099. doi:[10.1002/2014GL061904](https://doi.org/10.1002/2014GL061904)
- Drewes H, Kuglitsch F, Adám J, Rózsa S (2016) The Geodesist's handbook 2016. *J Geodesy* 90:907–1205. doi:[10.1007/s00190-016-0948-z](https://doi.org/10.1007/s00190-016-0948-z)
- Drinkwater MR, Floberghagen R, Haagmans R, Muzi D, Popescu A (2003) GOCE: ESA's first Earth explorer core mission. In: *Earth gravity field from space—from sensors to Earth sciences*. Space sciences series of ISSI, vol 17. Kluwer, Dordrecht, pp 419–432. ISBN: 1-4020-1408-2
- Farr TG et al (2007) The shuttle radar topography mission. *Rev Geophys* 45(2):RG2004. doi:[10.1029/2005RG000183](https://doi.org/10.1029/2005RG000183)
- Grigoriadis VN (2009) Geodetic and geophysical approach of the Earth's gravity field and applications in the Hellenic area. Dissertation, Aristotle University of Thessaloniki (in Greek)
- Grigoriadis VN, Kotsakis C, Tziavos IN, Vergos GS (2014) Estimation of the reference geopotential value for the local vertical datum of continental Greece using EGM08 and GPS/levelling data. In: *International association of geodesy symposia*, vol 141. Springer, Cham, pp 249–255. doi:[10.1007/978-3-319-10837-7_32](https://doi.org/10.1007/978-3-319-10837-7_32)
- Gruber T, Visser PNAM, Ackermann C, Hosse M (2011) Validation of GOCE gravity field models by means of orbit residuals and geoid comparisons. *J Geodesy* 85:845–860. doi:[10.1007/s00190-011-0486-7](https://doi.org/10.1007/s00190-011-0486-7)
- Gruber T, Gerlach C, Haagmans R (2012) Intercontinental height datum connection with GOCE and GPS-levelling data. *J Geodetic Sci* 2(4):240–280. doi:[10.2478/v10156-012-0001-y](https://doi.org/10.2478/v10156-012-0001-y)
- Gruber T, Rummel R, Ihde J, Liebsch G, Rülke A, Schäfer U, Sideris M, Rangelova E, Woodworth P, Hughes C, Gerlach C (2014) STSE - GOCE + height system unification with GOCE: summary and final report, Issue 1.0, 24 Feb 2014
- Haagmans R, de Min E, van Gelderen M (1993) Fast evaluation of convolution integrals on the sphere using 1D FFT and a comparison with existing methods for Stokes' integral. *Manuscr Geodaet* 18:227–241
- Heiskanen WA, Moritz H (1967) *Physical geodesy*. W.H. Freeman & Co Ltd, New York
- Hirt C, Featherstone WE, Marti U (2010) Combining EGM2008 and SRTM/DTM2006.0 residual terrain model data to improve quasi-geoid computations in mountainous areas devoid of gravity data. *J Geodesy* 84(9):557–567. doi:[10.1007/s00190-010-0395-1](https://doi.org/10.1007/s00190-010-0395-1)
- Kotsakis C, Katsambalos K, Ampatzidis D (2012) Estimation of the zero-height geopotential level W_0^{LVD} in a local vertical datum from inversion of co-located GPS, leveling and geoid heights: a case study in the Hellenic islands. *J Geodesy* 84:423–439. doi:[10.1007/s00190-011-0530-7](https://doi.org/10.1007/s00190-011-0530-7)
- Lemoine FG et al (1998) The development of the joint NASA GSFC and National Imagery and Mapping Agency (NIMA) geopotential model EGM96. NASA Technical Paper, 1998-206861
- Mayer-Gürr T, GOCO Team (2015) The combined satellite gravity field model GOCO05s. Presentation at EGU 2015, Vienna
- Pavlis NK, Holmes SA, Kenyon SC, Factor JK (2012) The development and evaluation of the earth gravitational model 2008 (EGM2008). *J Geophys Res* 117:B04406. doi:[10.1029/2011JB008916](https://doi.org/10.1029/2011JB008916)
- Pavlis NK, Holmes SA, Kenyon SC, Factor JK (2013) Correction to the development and evaluation of the earth gravitational model 2008 (EGM2008). *J Geophys Res* 118:2633. doi:[10.1002/jgrb.50167](https://doi.org/10.1002/jgrb.50167)
- Tapley BD, Bettadpur S, Watkins M, Reigber C (2004) The gravity recovery and climate experiment: mission overview and early results. *Geophys Res Lett* 31(9):L09607. doi:[10.1029/2004GL019920](https://doi.org/10.1029/2004GL019920)
- Vergos GS, Grigoriadis VN, Tziavos IN, Kotsakis C (2014) Evaluation of GOCE/GRACE global geopotential models over Greece with collocated GPS/levelling observations and local gravity data. In: *International Association of Geodesy symposia*, vol 141. Springer, Cham, pp 85–92. doi:[10.1007/978-3-319-10837-7_11](https://doi.org/10.1007/978-3-319-10837-7_11)

P.2 Publication II: Signal and Error Assessment of GOCE-based High Resolution Gravity Field Models

Reference

Gruber, T., Willberg, M. (2019). Signal and error assessment of GOCE-based high resolution gravity field models, *Journal of Geodetic Science*, 9(1), 71-86. doi 10.1515/jogs-2019-0008

Copyright

This work originally has been published in *Journal of Geodetic Science* as open access, available at <https://www.degruyter.com/>. The publication is available under the license of Creative Commons. The copyrights remain with the authors.

Abstract

The signal content and error level of recent GOCE-based high resolution gravity field models is assessed by means of signal degree variances and comparisons to independent GNSS-leveling geoid heights. The signal of the spherical harmonic series of these models is compared to the pre-GOCE EGM2008 model in order to identify the impact of GOCE data, of improved surface and altimetric gravity data and of modeling approaches. Results of the signal analysis show that in a global average roughly 80% of the differences are due to the inclusion of GOCE satellite information, while the remaining 20% are contributed by improved surface data. Comparisons of the global models to GNSS-leveling derived geoid heights demonstrate that a 1 cm geoid from the global model is feasible, if there is a high quality terrestrial gravity data set available. For areas with less good coverage an accuracy of several centimeters to a decimeter is feasible taking into account that GOCE provides now the geoid with a centimeter accuracy at spatial scales of 80 to 100 km. Comparisons with GNSS-leveling geoid heights also are a good tool to investigate possible systematic errors in the global models, in the spirit leveling and in the GNSS height observations. By means of geoid height differences and geoid slope differences one can draw conclusions for each regional data set separately. These conclusions need to be considered for a refined analysis, e.g., to eliminate suspicious GNSS/leveling data, to improve the global modeling by using full variance-covariance matrices and by consistently weighting the various data sources used for high resolution gravity field models. The paper describes the applied procedures, shows results for these geoid height and geoid slope differences for some regional data sets and draws conclusions about possible error sources and future work to be done in this context.

Declaration of own contribution

(TG: Thomas Gruber; MW: Martin Willberg)

The idea and study design were developed by TG, whereby significant aspects are the result of joint discussions between MW and TG. Both authors evaluated GNSS/leveling observations together. Thereby, MW contributed mainly with analysis and interpretation in the United States and Greece, which are used for the general conclusions of the paper. Accordingly, MW performed and validated parts of the calculations, but created only smaller shares of the corresponding results. TG produced most of the text, figures and tables, where MW contributed primarily with discussions, improvements and validation.

The overall own contribution of MW for *P-II* is estimated at 19 %, which is the average value of the percentage values estimated for the six criteria listed in the table below (Tab. P.2).

Criteria	Estimated own contribution
Computation and results	20 %
Ideas and study design	25 %
Analysis and interpretation	25 %
Text	15 %
Figures	15 %
Tables	15 %
Total	19 %

Tab. P.2 – Criteria and estimated contribution share of Martin Willberg for *P-II*

Confirmation by the author

I hereby confirm the correctness of the declaration of own contribution for the publication

Gruber, T., Willberg, M. (2019). *Signal and error assessment of GOCE-based high resolution gravity field models*, *Journal of Geodetic Science*, 9(1), 71-86. doi: <https://doi.org/10.1515/jogs-2019-0008>

Thomas Gruber

Institute for Astronomical and Physical Geodesy, Technical University of Munich, Germany

Signature: 

Date: *15.5.2020*

P.3 Publication III: Residual least-squares collocation: use of covariance matrices from high-resolution global geopotential models

Reference

Willberg, M., Zingerle, P., Pail, R. Residual least-squares collocation: use of covariance matrices from high-resolution global geopotential models. *J Geod* 93, 1739–1757 (2019). doi 10.1007/s00190-019-01279-1

Copyright

This work originally has been published in *Journal of Geodesy*, available at <https://link.springer.com/>, and is reprinted here with permissions of Springer. The copyright has been transferred to Springer-Verlag GmbH Germany.

Abstract

The paper presents a modified formulation of Least-Squares Collocation. This Residual Least-Squares Collocation (RLSC) includes a remove-compute-restore procedure with a high-resolution Global Geopotential Model (GGM) and a topographic gravitational potential model. In contrast to previous approaches, in RLSC, the remaining input residuals are modeled with error covariance matrices instead of signal covariance matrices. Therefore, we include the full variance-covariance information of a high-resolution GGM, namely the XGM2016, to the procedure. The included covariance matrices are anisotropic and location-dependent and enable a realistic error modeling of a target area. This fact represents an advantage over covariance matrices derived from signal degree variances or empirical covariance fitting. Additionally, due to the stochastic modeling of all involved components, RLSC provides realistic accuracy estimates. In a synthetic closed-loop test case with a realistic data distribution in the Andes we demonstrate the advantages of RLSC for regional geoid modeling and quantify the benefit which results mainly from a rigorously handled high-resolution GGM. In terms of root mean square deviations from the true reference solution, RLSC delivers an improvement of about 30% compared to a standard LSC approach, where the benefit is particularly pronounced in areas with a sparse data distribution. This improved performance, together with the fact that the resulting stochastic error estimates better reflect the true errors, might be an important aspect for the application of RLSC to derive gravity potential values and their uncertainties at reference stations of the International Height Reference System.

Declaration of own contribution

(MW: Martin Willberg; PZ: Philipp Zingerle; RP: Roland Pail)

MW and PZ derived the mathematical formulation of RLSC and the study design together, which are mostly the results of joint discussions (between MW and PZ). MW designed the test case in South America and the comparison between RLSC and LSC. PZ produced covariance matrices for XGM2016. Apart from that, MW performed the majority of all computations and created the results. MW was responsible for most of the analysis and interpretations, where PZ and RP contributed with discussions, corrections and support. MW wrote the text with improvements from RP and PZ. MW created figures and tables for the paper.

The overall own contribution of MW for *P-III* is estimated at 85 %, which is the average value of the percentage values estimated for the six criteria listed in the table below (Tab. P.3).

Criteria	Estimated own contribution
Computation and results	90 %
Ideas and study design	60 %
Analysis and interpretation	75 %
Text	90 %
Figures	95 %
Tables	100 %
Total	85 %

Tab. P.3 – Criteria and estimated contribution share of Martin Willberg for *P-III*


Confirmation by the authors

We hereby confirm the correctness of the declaration of own contribution for the publication

Willberg, M., Zingerle, P., Pail, R. (2019) Residual least-squares collocation: use of covariance matrices from high-resolution global geopotential models. J Geod 93, 1739–1757. doi: <https://doi.org/10.1007/s00190-019-01279-1>

Philipp Zingerle

Institute for Astronomical and Physical Geodesy, Technical University of Munich, Germany

Signature:  Date: *2.7.2020*

Roland Pail

Institute for Astronomical and Physical Geodesy, Technical University of Munich, Germany

Signature:  Date: *2.7.2020*



Residual least-squares collocation: use of covariance matrices from high-resolution global geopotential models

Martin Willberg¹ · Philipp Zingerle¹ · Roland Pail¹

Received: 24 August 2018 / Accepted: 30 June 2019 / Published online: 16 July 2019
© Springer-Verlag GmbH Germany, part of Springer Nature 2019

Abstract

The paper presents a modified formulation of least-squares collocation. This residual least-squares collocation (RLSC) includes a remove–compute–restore procedure with a high-resolution global geopotential model (GGM) and a topographic gravitational potential model. In contrast to previous approaches, in RLSC, the remaining input residuals are modeled with error covariance matrices instead of signal covariance matrices. Therefore, we include the full variance–covariance information of a high-resolution GGM, namely the XGM2016, to the procedure. The included covariance matrices are anisotropic and location-dependent and enable a realistic error modeling of a target area. This fact represents an advantage over covariance matrices derived from signal degree variances or empirical covariance fitting. Additionally, due to the stochastic modeling of all involved components, RLSC provides realistic accuracy estimates. In a synthetic closed-loop test case with a realistic data distribution in the Andes we demonstrate the advantages of RLSC for regional geoid modeling and quantify the benefit which results mainly from a rigorously handled high-resolution GGM. In terms of root mean square deviations from the true reference solution, RLSC delivers an improvement of about 30% compared to a standard LSC approach, where the benefit is particularly pronounced in areas with a sparse data distribution. This improved performance, together with the fact that the resulting stochastic error estimates better reflect the true errors, might be an important aspect for the application of RLSC to derive gravity potential values and their uncertainties at reference stations of the international height reference system.

Keywords Least-squares collocation · Regional geoid modeling · Covariance function · Remove–compute–restore · XGM2016 · High-resolution GGM

1 Introduction

In this paper, we present a method for improving regional geoid modeling by including full covariance information from a high-resolution global geopotential model (GGM) in least-squares collocation (LSC). Since its foundation by Krarup (1969), and the key publication by Moritz (1980) LSC is considered as one of the most important methods for local and regional geoid modeling. Although the main concept of LSC has never changed, a few adaptations have been introduced recently. Nowadays, frequently a satellite-only model is used in LSC as background for the long wavelength part of the Earth's gravity field. LSC thereby benefits

from the good model quality in the long wavelength part that is mainly provided by the Gravity Recovery And Climate Experiment (GRACE; Tapley et al. 2004) mission and the Gravity field and steady-state Ocean Circulation Explorer (GOCE; Drinkwater et al. 2003) mission.

Compared to satellite-only GGMs, high-resolution GGMs (we use this term for models with a maximum degree of 719 or higher) have included a wider spectral range of the Earth's gravity signal and therefore exhibit a higher commission error. For many of these high-resolution GGMs, the associated variance–covariance information is not fully available. As an example, in the case of EGM2008 only grids of geographic error variances of gravity anomalies and geoid undulations are provided (Pavlis et al. 2012). Additionally, EGM2008 and other high-resolution GGMs like EIGEN-6c (Förste et al. 2014) assume constant accuracy for their input ground data. However, with GOCO05c (Fecher et al. 2017) and its successor XGM2016 (Pail et al. 2018) we have two high-resolution GGMs that apply regional vary-

Martin Willberg
martin.willberg@tum.de

¹ Institute of Astronomical and Physical Geodesy, Technical University of Munich, Arcisstrasse 21, 80333 Munich, Germany

ing weighting which results in an improved, more realistic and location-dependent accuracy estimation that enables us to use covariance matrices from these models for LSC. In this paper, we present the first inclusion of high-resolution GGMs with their full covariance matrices in LSC, develop the corresponding methodology and demonstrate its improvement to standard LSC in a numerical closed-loop simulation. The benefit of consistently including covariance matrices from a satellite-only GGM has already been demonstrated in various publications. This was first performed with a full covariance matrix by Haagmans and van Gelderen (1991). Pail et al. (2010) then demonstrated the rigorous inclusion of a GGM and its full accuracy information to LSC in a remove–compute–restore (RCR) approach. However, unlike other methods, our approach is specifically adjusted to work with high-resolution GGMs which leads us to an extended formalism of the LSC problem. Gerlach and Fecher (2012) showed that for GOCE covariance information, the very high computation effort of calculating full covariance matrices can be significantly reduced using approximations such as sparse or block-diagonal covariance matrices without losing much benefit. However, this simplification is not valid in our case since GGMs with regional weighting cause strong correlations among the gravity field parameters (Fecher et al. 2017).

The LSC approach is in practice still a frequently applied method for regional gravity geoid modeling. According to Moritz (1980) and Sansò (1986) the disturbing gravity field T of the Earth can be described as a random field. Also, it is possible to derive a statistical and homogeneous description of T that determines a global average part of the gravity field (Moritz 1980; Tscherning 1999). However, this does not coincide with reality because the correlation length and the covariance change with location. As a result, the use of homogeneous and isotropic covariance functions (e.g., in Moritz 1980) does not always give an optimal result in LSC (Tscherning 1999). Therefore, we adapt the LSC notation from Moritz (1980) in several, closely connected ways: (1) we include consistent treatment of covariance information in an RCR approach, (2) we change the definition of covariance matrices by replacing the total average operator with the mathematical expectation value, and (3) we use only residuals as LSC input which changes the nature of the covariance matrices as they describe only uncertainties instead of signal content. Here, our approach differs from previous studies by Moritz (1980), Pail et al. (2010), Forsberg and Tscherning (1981), Tscherning and Rapp (1974), or Sansò (1986). Only through these adaptations, we are able to use the location-dependent covariance matrices that are derived directly from the normal equation system of a high-resolution GGM. Furthermore, our notation offers the advantage that every input quantity in LSC is directly described by a covariance matrix which is in contrast with, for example, the definition by Haagmans and van Gelderen (1991). We see these adapta-

tions as a necessary step towards using modern high-quality models effectively in LSC. At the present stage, we use the XGM2016 (Pail et al. 2018) and the topographic gravity model dV_ELL_Earth2014 (Rexer et al. 2016) for the RCR approach.

This paper is structured as follows. In Sect. 2 we derive in detail the adaptations to LSC by Moritz (1980). Next, in Sect. 3 we describe the specifications of a synthetic test case scenario in South America as well as the data sets that we use to show the benefit of our method. The results of three numerical test cases are visualized and outlined in Sect. 4, and finally Sect. 5 draws conclusions, describes ways to benefit from the demonstrated approach, and provides an outlook.

2 Theoretical background

2.1 LSC according to Moritz (1980)

This section adopts the content and notation of Moritz (1980). For our purposes we rewrite only those parts that are essential for the next sections. The formulas of the least-squares prediction for random observations \mathbf{I} and a random output signal \mathbf{s} are given in Moritz (1980, Chapter 9) with

$$\mathbf{s} = \mathbf{C}_{sl} \mathbf{C}_{ll}^{-1} \mathbf{I}, \tag{1}$$

$$\mathbf{E}_{ss} = \mathbf{C}_{ss} - \mathbf{C}_{sl} \mathbf{C}_{ll}^{-1} \mathbf{C}_{ls}, \tag{2}$$

where \mathbf{E}_{ss} is the error covariance of the output \mathbf{s} , and \mathbf{C} are covariance matrices with the subscripts giving the positions and functionals of the related points. This is valid for all \mathbf{I} and \mathbf{s} with

$$E\{\mathbf{I}\} = \mathbf{0}, \quad E\{\mathbf{s}\} = \mathbf{0}, \tag{3}$$

where E describes the expectation operator in form of a mathematical probability distribution. Afterwards, in the section ‘Collocation with random errors’ (Moritz 1980, Chapter 14) the observations \mathbf{I} as a functional of the gravitational potential T are redefined as a combination of the true input signal \mathbf{t} and a random (stochastic) noise \mathbf{n} . So that, in symbolic notation we have

$$\mathbf{I} = \mathbf{t} + \mathbf{n}. \tag{4}$$

In analogy to the definition of \mathbf{t} , \mathbf{s} is defined as the true output signal. The gravity field functionals \mathbf{t} and \mathbf{s} are not random in a mere statistical manner since every evaluation point has a value without uncertainty. However, as it is done by Moritz (1980, Chapter 14), we treat \mathbf{t} and \mathbf{s} as statistical values in a

formal sense. This justifies the usage of the expectation operator E which, however, leaves the signals \mathbf{t} and \mathbf{s} unaffected

$$\begin{aligned} E\{\mathbf{s}\} &= \mathbf{s}, \\ E\{\mathbf{t}\} &= \mathbf{t}, \\ E\{\mathbf{n}\} &= \mathbf{0}, \\ E\{\mathbf{l}\} &= E\{\mathbf{t}\} + E\{\mathbf{n}\} = \mathbf{t}. \end{aligned} \tag{5}$$

In contrast to the expectation in a probabilistic sense, the operator M describes a homogeneous, isotropic average over the sphere which gives the mean global behavior of the gravitational field. \mathbf{t} , \mathbf{s} and \mathbf{l} are all functionals of the disturbing potential. Therefore, applying the operator M to \mathbf{t} , \mathbf{s} and \mathbf{l} gets zero. Thus, we write for the spatial average M

$$\begin{aligned} M\{\mathbf{s}\} &= 0, \\ M\{\mathbf{t}\} &= 0, \\ M\{\mathbf{l}\} &= 0, \\ M\{\mathbf{n}\} &= n. \end{aligned} \tag{6}$$

In Eq. 5, we can see that in general the observations \mathbf{l} are not centered, but in a global view with the definition of a total average operator \bar{E}

$$\bar{E} = EM, \tag{7}$$

which is an average over the probability distribution and the global distribution (sphere), they can be considered as centered quantities

$$\begin{aligned} \bar{E}\{\mathbf{s}\} &= EM\{\mathbf{s}\} = 0, \\ \bar{E}\{\mathbf{t}\} &= EM\{\mathbf{t}\} = 0, \\ \bar{E}\{\mathbf{l}\} &= EM\{\mathbf{t}\} + EM\{\mathbf{n}\} = 0. \end{aligned} \tag{8}$$

To be able to distinguish between different forms of covariance matrices in the following sections, we write covariance matrices that are derived from the total average \bar{E} with \bar{C} instead of C . Consequently, the covariance matrices of the centered quantities defined by the total average \bar{E} are

$$\begin{aligned} \bar{C}_{ss} &= \bar{E}\{\mathbf{s}\mathbf{s}^T\} = EM\{\mathbf{s}\mathbf{s}^T\} = M\{\mathbf{s}\mathbf{s}^T\}, \\ \bar{C}_{tt} &= \bar{E}\{\mathbf{t}\mathbf{t}^T\} = EM\{\mathbf{t}\mathbf{t}^T\} = M\{\mathbf{t}\mathbf{t}^T\}, \\ \bar{C}_{nn} &= \bar{E}\{\mathbf{n}\mathbf{n}^T\} = EM\{\mathbf{n}\mathbf{n}^T\} = E\{\mathbf{n}\mathbf{n}^T\} = C_{nn}. \end{aligned} \tag{9}$$

By considering the fact that \mathbf{t} and \mathbf{s} are uncorrelated to \mathbf{n} , we write by using Eq. 4

$$\begin{aligned} \bar{C}_{ll} &= \bar{E}\{\mathbf{l}\mathbf{l}^T\} \\ &= \bar{E}\{(\mathbf{t} + \mathbf{n})(\mathbf{t} + \mathbf{n})^T\} \\ &= \bar{E}\{\mathbf{t}\mathbf{t}^T\} + \bar{E}\{\mathbf{t}\mathbf{n}^T\} + \bar{E}\{\mathbf{n}\mathbf{t}^T\} + \bar{E}\{\mathbf{n}\mathbf{n}^T\} \end{aligned}$$

$$\begin{aligned} &= \bar{C}_{tt} + \underbrace{\bar{C}_{tn}}_{=0} + \underbrace{\bar{C}_{nt}}_{=0} + C_{nn} \\ &= \bar{C}_{tt} + C_{nn}, \end{aligned} \tag{10}$$

$$\begin{aligned} \bar{C}_{sl} &= \bar{E}\{\mathbf{s}\mathbf{l}^T\} \\ &= \bar{E}\{(\mathbf{s})(\mathbf{t} + \mathbf{n})^T\} \\ &= \bar{E}\{\mathbf{s}\mathbf{t}^T\} + \bar{E}\{\mathbf{s}\mathbf{n}^T\} \\ &= \bar{C}_{st} + \underbrace{\bar{C}_{sn}}_{=0}. \end{aligned} \tag{11}$$

Applying these expressions, the fundamental formula for least-squares collocation with noise is obtained from Eq. 1

$$\bar{\mathbf{s}} = \bar{C}_{st} (\bar{C}_{tt} + C_{nn})^{-1} \mathbf{l}. \tag{12}$$

For consistency with the following sections and in contrast to Moritz (1980) we retain the bar over all quantities with inclusion of the global average operator \bar{E} , and write for the corresponding error covariance matrix \bar{E}_{ss} according to Eq. 2

$$\bar{E}_{ss} = \bar{C}_{ss} - \bar{C}_{st} (\bar{C}_{tt} + C_{nn})^{-1} \bar{C}_{st}^T. \tag{13}$$

This description of least-squares collocation by Moritz (1980, Chapter 14) has been established as standard procedure in the literature (see Tscherning 2015; Arabelos and Tscherning 2009; Hofmann-Wellenhof and Moritz 2006; Rieser 2015) and we follow this notation because in our opinion it is the most consistent and detailed description. However, it should be kept in mind that these definitions are only valid for centered observations \mathbf{l} and a centered output \mathbf{s} , because this was set as a requirement (Eq. 3) and is used in the definitions of the covariance matrices (Eqs. 9–11). Furthermore, the covariance matrices as defined in this section assume a normal distribution of gravitational functionals and describe an average part of the Earth's surface. Accordingly, these covariance matrices are mainly independent of the location on the Earth (homogeneous) as well as of the direction (isotropic), and as a consequence may not be optimal for local gravity field collocation (Tscherning 1999). Note, that most of the covariance matrices in Moritz (1980) are calculated from signal degree variances, but the discussion in this paragraph holds also for analytical covariance matrices which are calculated by empirical covariance fitting, e.g., from a Tscherning–Rapp model (Tscherning and Rapp 1974). While the latter do not consider a global view, they use the same assumptions, namely centered and normally distributed observations, for a target regional area, therefore resulting in homogeneous and isotropic covariance functions as well.

2.2 The remove–compute–restore (RCR) approach

For many applications, LSC is combined with a remove–compute–restore (RCR) approach (Forsberg and Tscherning 1981; Forsberg 1984). According to the name, RCR means that a part $\hat{\mathbf{l}}$ of the signal is removed from the observations \mathbf{l} before the computation

$$\Delta \mathbf{l} = \mathbf{l} - \hat{\mathbf{l}}. \tag{14}$$

Accordingly, the collocation Γ is performed only with the residuals of the input signal $\Delta \mathbf{l}$

$$\Delta \mathbf{s} = \Gamma \Delta \mathbf{l}, \tag{15}$$

and afterwards, the removed part $\hat{\mathbf{s}}$ is restored again

$$\mathbf{s} = \Delta \mathbf{s} + \hat{\mathbf{s}}, \tag{16}$$

to yield the output \mathbf{s} of the collocation. The main reason for using RCR in collocation is that LSC with residuals is more accurate than it would be with the full signal content. For more detailed background, we refer to Hofmann-Wellenhof and Moritz (2006, Chapter 11) or Rieser (2015, Chapter 4). Usually, the remove and restore steps describe different functionals of the gravity field, and the RCR thereby implicitly includes a field transformation. Moreover, because a field transformation moves signal energy between different degrees in the frequency domain an error in the remove step may not be consistently restored after a field transformation. This might even be the case when remove and restore steps are calculated consistently. Therefore, we see the need to model the accuracy of the remove step consistently in LSC. Only some of the LSC approaches take the accuracy of the reduction model into account (e.g., Haagmans and van Gelderen 1991; Pail et al. 2010; Sansò 2013) while other approaches do not (e.g., Forsberg and Tscherning 1981; Hofmann-Wellenhof and Moritz 2006; Rieser 2015).

In general, the corresponding covariance matrices in all these approaches are calculated either from signal degree variances (Heiskanen and Moritz 1967, Chapter 7.3; Moritz 1980, Chapter 10) or from empirical covariance fitting (Tscherning and Rapp 1974). Those approaches that include the accuracy of a reduction model directly in the calculation, additionally introduce the covariance matrix of a satellite-only model to the method (e.g., Haagmans and van Gelderen (1991)). Since all of these LSC approaches are formulated differently and use various notations, we do not go into further detail but point out only the differences of our approach to the existing ones in the following sections.

2.3 Residual least-squares collocation

Although observations \mathbf{l} and output \mathbf{s} of a LSC as functionals of the disturbing gravity field T of the Earth are centered globally (Heiskanen and Moritz 1967, Chapter 2.19), it is not possible to automatically assume the same for regional gravity field modeling. However, the definition of LSC according to Sect. 2.1 is only valid if the observations and the output are centered over the target area (Eq. 3). We propose rather to use covariance matrices from a purely stochastic point of view and thereby follow the standard definition of a covariance with an expectation value in a mathematical sense E (Eqs. 17–19). As a result, we are no longer limited to the requirements of Eq. 3. The gravity functionals \mathbf{t} and \mathbf{s} are furthermore regarded as statistical quantities in a formal sense. As they are defined as true signal content of the gravity field, repeated error-free measurements at one point always give the same result (see Eq. 5). Considering this, we write for the covariance matrices $\mathbf{C}_{\mathbf{s}\mathbf{s}}$, $\mathbf{C}_{\mathbf{t}\mathbf{t}}$ and $\mathbf{C}_{\mathbf{l}\mathbf{l}}$

$$\mathbf{C}_{\mathbf{s}\mathbf{s}} = E\{(\underbrace{\mathbf{s} - E\{\mathbf{s}\}}_{=\mathbf{s}})(\underbrace{\mathbf{s} - E\{\mathbf{s}\}}_{=\mathbf{s}})^T\} = \{\mathbf{0}\}, \tag{17}$$

$$\mathbf{C}_{\mathbf{t}\mathbf{t}} = E\{(\underbrace{\mathbf{t} - E\{\mathbf{t}\}}_{=\mathbf{t}})(\underbrace{\mathbf{t} - E\{\mathbf{t}\}}_{=\mathbf{t}})^T\} = \{\mathbf{0}\}, \tag{18}$$

$$\mathbf{C}_{\mathbf{l}\mathbf{l}} = E\{(\underbrace{\mathbf{l} - E\{\mathbf{l}\}}_{=\mathbf{t}})(\underbrace{\mathbf{l} - E\{\mathbf{l}\}}_{=\mathbf{t}})^T\} = E\{\mathbf{nn}^T\} = \mathbf{C}_{\mathbf{nn}}, \tag{19}$$

which differs from the equivalent formulation in Moritz (1980) (Eqs. 9, 10). The covariance of the uncorrelated observations that is named $\mathbf{C}_{\mathbf{nn}}$ in Moritz (1980) is hereinafter called $\mathbf{C}_{\mathbf{l}\mathbf{l}}$. We consider this notation as more consistent, because it describes the accuracy of the observations. Note at this point, that \mathbf{t} and \mathbf{l} are not centered (Eq. 5). Now, we assume that we can calculate an unbiased GGM without systematic errors that is able to describe the full signal content of the Earth's gravity field. From this model we derive different gravity field functionals \mathbf{t} at the input points. Since this variable is not error-free, we denote the quantity $\hat{\mathbf{l}}$ and write for its expectation value E

$$E\{\hat{\mathbf{l}}\} = \mathbf{t}. \tag{20}$$

We use the hat operator for quantities that are derived from an introduced model in order to distinguish them from measurements and error-free quantities. Since we assumed that $\hat{\mathbf{l}}$ does not contain systematic errors, the difference $\Delta \mathbf{l}$

$$\Delta \mathbf{l} = \mathbf{l} - \hat{\mathbf{l}}, \tag{21}$$

is centered and describes a remove step (see Sect. 2.2). By analogy, we write $\hat{\mathbf{s}}$ as the result of the same model as an approximation of the true gravity signal \mathbf{s} and obtain

$$\Delta \mathbf{s} = \mathbf{s} - \hat{\mathbf{s}}. \tag{22}$$

The resulting covariance matrices $\mathbf{C}_{\hat{\mathbf{I}}}$, $\mathbf{C}_{\hat{\mathbf{s}}}$ and $\mathbf{C}_{\hat{\mathbf{s}}\hat{\mathbf{s}}}$ of our estimated values $\hat{\mathbf{I}}$ and $\hat{\mathbf{s}}$ are defined by

$$\begin{aligned} \mathbf{C}_{\hat{\mathbf{I}}} &= E\{(\hat{\mathbf{I}} - E\{\hat{\mathbf{I}}\})(\hat{\mathbf{I}} - E\{\hat{\mathbf{I}}\})^T\} \\ &= E\{(\hat{\mathbf{I}} - \mathbf{t})(\hat{\mathbf{I}} - \mathbf{t})^T\}, \end{aligned} \tag{23}$$

$$\begin{aligned} \mathbf{C}_{\hat{\mathbf{s}}} &= E\{(\hat{\mathbf{s}} - E\{\hat{\mathbf{s}}\})(\hat{\mathbf{s}} - E\{\hat{\mathbf{s}}\})^T\} \\ &= E\{(\hat{\mathbf{s}} - \mathbf{s})(\hat{\mathbf{s}} - \mathbf{s})^T\}, \end{aligned} \tag{24}$$

$$\begin{aligned} \mathbf{C}_{\hat{\mathbf{s}}\hat{\mathbf{s}}} &= E\{(\hat{\mathbf{s}} - E\{\hat{\mathbf{s}}\})(\hat{\mathbf{s}} - E\{\hat{\mathbf{s}}\})^T\} \\ &= E\{(\hat{\mathbf{s}} - \mathbf{s})(\hat{\mathbf{s}} - \mathbf{s})^T\}. \end{aligned} \tag{25}$$

They are used in the following to form the covariance matrices $\mathbf{C}_{\Delta \mathbf{I} \Delta \mathbf{I}}$, $\mathbf{C}_{\Delta \mathbf{s} \Delta \mathbf{I}}$ and $\mathbf{C}_{\Delta \mathbf{s} \Delta \mathbf{s}}$. For the transcription of $\mathbf{C}_{\Delta \mathbf{I} \Delta \mathbf{I}}$ we use Eqs. 4, 19, 21 and 23 and the fact that the random noise \mathbf{n} is uncorrelated to a signal.

$$\begin{aligned} \mathbf{C}_{\Delta \mathbf{I} \Delta \mathbf{I}} &= E\{(\Delta \mathbf{I} - \underbrace{E\{\Delta \mathbf{I}\}}_{=0})(\Delta \mathbf{I} - \underbrace{E\{\Delta \mathbf{I}\}}_{=0})^T\} \\ &= E\{\Delta \mathbf{I} \Delta \mathbf{I}^T\} \\ &= E\{((\mathbf{t} + \mathbf{n}) - \hat{\mathbf{I}})((\mathbf{t} + \mathbf{n}) - \hat{\mathbf{I}})^T\} \\ &= E\{((\mathbf{t} - \hat{\mathbf{I}}) + \mathbf{n})((\mathbf{t} - \hat{\mathbf{I}}) + \mathbf{n})^T\} \\ &= E\{(\mathbf{t} - \hat{\mathbf{I}})(\mathbf{t} - \hat{\mathbf{I}})^T\} + \underbrace{E\{(\mathbf{t} - \hat{\mathbf{I}})\mathbf{n}^T\}}_{=0} \\ &\quad + \underbrace{E\{\mathbf{n}(\mathbf{t} - \hat{\mathbf{I}})^T\}}_{=0} + E\{\mathbf{n}\mathbf{n}^T\} \\ &= \mathbf{C}_{\hat{\mathbf{I}}} + \mathbf{C}_{\mathbb{I}} \end{aligned} \tag{26}$$

$\Delta \mathbf{I}$ contains the uncertainty of the observations \mathbf{I} as well as the uncertainty of observations $\hat{\mathbf{I}}$ synthesized from a GGM. Correspondingly, we can divide the covariance matrix $\mathbf{C}_{\Delta \mathbf{I} \Delta \mathbf{I}}$ into the covariance of the model accuracy $\mathbf{C}_{\hat{\mathbf{I}}}$, and the covariance $\mathbf{C}_{\mathbb{I}}$ that describes the observation noise according to Eq. 19. Again applying the fact that the random noise \mathbf{n} is uncorrelated to \mathbf{s} and $\hat{\mathbf{s}}$, we write analogously for $\mathbf{C}_{\Delta \mathbf{s} \Delta \mathbf{I}}$ and $\mathbf{C}_{\Delta \mathbf{s} \Delta \mathbf{s}}$

$$\begin{aligned} \mathbf{C}_{\Delta \mathbf{s} \Delta \mathbf{I}} &= E\{(\Delta \mathbf{s} - \underbrace{E\{\Delta \mathbf{s}\}}_{=0})(\Delta \mathbf{I} - \underbrace{E\{\Delta \mathbf{I}\}}_{=0})^T\} \\ &= E\{\Delta \mathbf{s} \Delta \mathbf{I}^T\} \\ &= E\{(\mathbf{s} - \hat{\mathbf{s}})((\mathbf{t} + \mathbf{n}) - \hat{\mathbf{I}})^T\} \\ &= E\{(\mathbf{s} - \hat{\mathbf{s}})((\mathbf{t} - \hat{\mathbf{I}}) + \mathbf{n})^T\} \end{aligned}$$

$$\begin{aligned} &= E\{(\mathbf{s} - \hat{\mathbf{s}})(\mathbf{t} - \hat{\mathbf{I}})^T\} + \underbrace{E\{(\mathbf{s} - \hat{\mathbf{s}})\mathbf{n}^T\}}_{=0} \\ &= \mathbf{C}_{\hat{\mathbf{s}}}, \end{aligned} \tag{27}$$

$$\begin{aligned} \mathbf{C}_{\Delta \mathbf{s} \Delta \mathbf{s}} &= E\{(\Delta \mathbf{s} - \underbrace{E\{\Delta \mathbf{s}\}}_{=0})(\Delta \mathbf{s} - \underbrace{E\{\Delta \mathbf{s}\}}_{=0})^T\} \\ &= E\{\Delta \mathbf{s} \Delta \mathbf{s}^T\} \\ &= E\{(\mathbf{s} - \hat{\mathbf{s}})(\mathbf{s} - \hat{\mathbf{s}})^T\} \\ &= \mathbf{C}_{\hat{\mathbf{s}}\hat{\mathbf{s}}}, \end{aligned} \tag{28}$$

with $\mathbf{C}_{\hat{\mathbf{s}}}$ being the covariance of the introduced model that describes the uncertainties and correlations between the positions and functionals of the input to those of the output. Analogously, the covariance $\mathbf{C}_{\hat{\mathbf{s}}\hat{\mathbf{s}}}$ describes the uncertainties and the correlations of $\hat{\mathbf{s}}$ among different output positions (and functionals).

Thus, we can rewrite the definition of LSC from Eq. 12 with $\Delta \mathbf{I}$ and $\Delta \mathbf{s}$ instead of \mathbf{I} and \mathbf{s} and use the findings from Eqs. 21, 26 and 27, resulting in a notation of LSC that uses only residuals as input

$$\begin{aligned} \Delta \mathbf{s} &= \mathbf{C}_{\Delta \mathbf{s} \Delta \mathbf{I}} (\mathbf{C}_{\Delta \mathbf{I} \Delta \mathbf{I}})^{-1} \Delta \mathbf{I} \\ &= \mathbf{C}_{\hat{\mathbf{s}}} (\mathbf{C}_{\mathbb{I}} + \mathbf{C}_{\hat{\mathbf{I}}})^{-1} (\mathbf{I} - \hat{\mathbf{I}}). \end{aligned} \tag{29}$$

After restoring the subtracted signal part $\hat{\mathbf{s}}$ we define the residual least-squares collocation (RLSC)

$$\mathbf{s} = \mathbf{C}_{\hat{\mathbf{s}}} (\mathbf{C}_{\mathbb{I}} + \mathbf{C}_{\hat{\mathbf{I}}})^{-1} (\mathbf{I} - \hat{\mathbf{I}}) + \hat{\mathbf{s}}. \tag{30}$$

Instead of centered observations and a centered output which are used as requirements in Sect. 2.1, we introduce the assumption that it is possible to describe the observations \mathbf{I} and the output \mathbf{s} by means of an unbiased model ($\hat{\mathbf{I}}$ and $\hat{\mathbf{s}}$). In this way, the input $(\mathbf{I} - \hat{\mathbf{I}})$ of RLSC stays centered. We have two key factors of RLSC in comparison with other LSC methods: (1) the input consists only of residuals, and (2) the covariance matrices $\mathbf{C}_{\mathbb{I}}$ and $\mathbf{C}_{\hat{\mathbf{I}}}$ describe the accuracy of the input \mathbf{I} and $\hat{\mathbf{I}}$ directly. With these considerations, we differ from previous LSC approaches (e.g., Moritz 1980; Haagmans and van Gelderen 1991; Pail et al. 2010; Sansò 2013; Rieser 2015), which always include signal covariance matrices in LSC, while in our approach the covariance matrices contain only the uncertainties of input and output. For example, Haagmans and van Gelderen (1991) also include a reduction step with full covariance information in LSC, but at the same time they use a third covariance matrix inside the brackets of Eq. 30 that describes the covariance of the gravity signal itself (equal to $\tilde{\mathbf{C}}_{\mathbf{t}\mathbf{t}}$ from Sect. 2.1). The reason for the difference at this point is that we assume the existence of a high-quality GGM, whose uncertainties can be fully described by a variance-covariance matrix (no systematic errors), which other approaches do not.

The interpretation of Eq. 30 is quite different from the definitions in Sect. 2.1 where the covariance matrices in the collocation describe the signal content instead of the error characteristics. Nevertheless, RLSC is consistent with the theory of Moritz (1980), which can be demonstrated by the following thought experiment. If the model $\hat{\mathbf{l}}$ in Eq. 30 becomes worse, then the elements of the covariance matrix $\mathbf{C}_{\hat{\mathbf{l}}}$ that describe its uncertainties will become larger. This is also valid for an extreme case where we do not subtract a model at all, so that $\hat{\mathbf{l}}$ becomes zero. In this case, the covariance $\mathbf{C}_{\hat{\mathbf{l}}}$ describes the full signal content of the observations \mathbf{l} which is basically the same idea as in Moritz (1980). However, the covariance $\mathbf{C}_{\hat{\mathbf{l}}}$ is still regarded as the uncertainty of the bad (or missing) model instead of the covariance of the signal content (as it is in Sect. 2.1). Even with $\hat{\mathbf{l}} = \mathbf{0}$ there is a difference in the approaches, since in general the expectation value E is not equal to the total average \bar{E} (Eq. 7). However, it is possible to use the total average \bar{E} as an approximation of the expectation value E , which means that for $\hat{\mathbf{l}} = \mathbf{0}$ we can approximate

$$\begin{aligned} \mathbf{C}_{\hat{\mathbf{l}}} &\approx \bar{\mathbf{C}}_{\mathbf{tt}}, \\ \mathbf{C}_{\hat{\mathbf{s}}\hat{\mathbf{l}}} &\approx \bar{\mathbf{C}}_{\mathbf{st}}. \end{aligned} \tag{31}$$

With this approximation our formulation of least-squares collocation with errors (Eq. 30) becomes identical to standard LSC from Moritz (1980) (Eq. 12) including the RCR approach (Eqs. 14, 16). Accordingly, we write for the error covariance matrix $\mathbf{E}_{\mathbf{ss}}$ of the output \mathbf{s} in Eq. 30 and refer to Moritz (1980, Chapter 14) for an analogous and detailed derivation

$$\mathbf{E}_{\mathbf{ss}} = \mathbf{C}_{\hat{\mathbf{s}}\hat{\mathbf{s}}} - \mathbf{C}_{\hat{\mathbf{s}}\hat{\mathbf{l}}} (\mathbf{C}_{\mathbf{ll}} + \mathbf{C}_{\hat{\mathbf{l}}})^{-1} \mathbf{C}_{\hat{\mathbf{l}}\hat{\mathbf{s}}}^T. \tag{32}$$

Note that, by definition there is no difference between \mathbf{E} and \mathbf{C} in our approach since both describe error covariance matrices. Nevertheless, we retain this notation because it clarifies that $\mathbf{E}_{\mathbf{ss}}$ refers to the covariance of the output \mathbf{s} instead of the true gravity signal \mathbf{s} or the model $\hat{\mathbf{s}}$.

2.4 Inclusion of a GGM and a topographic gravity model into RLSC

To calculate RLSC from Eq. 30 we require estimates of the input $\hat{\mathbf{l}}$ and the output $\hat{\mathbf{s}}$ as well as the related covariance matrices for the input $\mathbf{C}_{\hat{\mathbf{l}}}$, the output $\mathbf{C}_{\hat{\mathbf{s}}\hat{\mathbf{s}}}$ and the combination $\mathbf{C}_{\hat{\mathbf{s}}\hat{\mathbf{l}}}$. All of these can be derived from the normal equation system related to a GGM

$$\mathbf{N}_{\hat{\mathbf{l}}\hat{\mathbf{l}}}^m \hat{\mathbf{x}}_f^m = \mathbf{q}_f^m. \tag{33}$$

Here, $\mathbf{N}_{\hat{\mathbf{l}}\hat{\mathbf{l}}}^m$ is the normal equation matrix, \mathbf{q}_f^m is the right-hand side, and $\hat{\mathbf{x}}_f^m$ are the estimated Spherical Harmonic (SH)

coefficients. The superscript ‘m’ refers to quantities that are derived from a GGM. In the following we continue to use superscripts to clarify the origin of covariance matrices and vectors. In contrast, the subscripts are continuously applied to describe the corresponding functionals and their positions with the subscript ‘f’ standing for the frequency domain of the SH coefficients. For more details about the normal equation system describing the SH coefficients we refer to Fecher et al. (2015). Next, the normal equation matrix $\mathbf{N}_{\hat{\mathbf{l}}\hat{\mathbf{l}}}^m$ is inverted

$$\mathbf{C}_{\hat{\mathbf{l}}\hat{\mathbf{l}}}^m = (\mathbf{N}_{\hat{\mathbf{l}}\hat{\mathbf{l}}}^m)^{-1}, \tag{34}$$

to obtain the covariance matrix $\mathbf{C}_{\hat{\mathbf{l}}\hat{\mathbf{l}}}^m$ of the SH coefficients, which is used to solve the normal equation system and estimate the SH coefficients $\hat{\mathbf{x}}_f^m$

$$\hat{\mathbf{x}}_f^m = \mathbf{C}_{\hat{\mathbf{l}}\hat{\mathbf{l}}}^m \mathbf{q}_f^m. \tag{35}$$

Afterwards, we write the transformations of the SH coefficients to different functionals and point positions in the space domain with the design matrices $\mathbf{A}_{\mathbf{to}}^{\text{from}}$.

$$\begin{aligned} \hat{\mathbf{l}}^m &= \mathbf{A}_l^f \hat{\mathbf{x}}_f^m, \\ \hat{\mathbf{s}}^m &= \mathbf{A}_s^f \hat{\mathbf{x}}_f^m, \end{aligned} \tag{36}$$

and for the calculation of the covariance matrices

$$\begin{aligned} \mathbf{C}_{\hat{\mathbf{l}}\hat{\mathbf{l}}}^m &= \mathbf{A}_l^f \mathbf{C}_{\hat{\mathbf{l}}\hat{\mathbf{l}}}^m \mathbf{A}_l^{fT}, \\ \mathbf{C}_{\hat{\mathbf{s}}\hat{\mathbf{l}}}^m &= \mathbf{A}_s^f \mathbf{C}_{\hat{\mathbf{l}}\hat{\mathbf{l}}}^m \mathbf{A}_l^{fT}, \\ \mathbf{C}_{\hat{\mathbf{s}}\hat{\mathbf{s}}}^m &= \mathbf{A}_s^f \mathbf{C}_{\hat{\mathbf{l}}\hat{\mathbf{l}}}^m \mathbf{A}_s^{fT}. \end{aligned} \tag{37}$$

Here, the covariance $\mathbf{C}_{\hat{\mathbf{l}}\hat{\mathbf{l}}}^m$ describes the uncertainties and correlations of the GGM at the input points, $\mathbf{C}_{\hat{\mathbf{s}}\hat{\mathbf{s}}}^m$ the covariance at the output points, and $\mathbf{C}_{\hat{\mathbf{s}}\hat{\mathbf{l}}}^m$ their cross correlations. The square root of the main diagonal of $\mathbf{C}_{\hat{\mathbf{l}}\hat{\mathbf{l}}}^m$ gives the standard deviations of the GGM parameters at the input points in terms of the respective functional. Note that as the result of a GGM, $\hat{\mathbf{l}}^m$ is a representative of the gravity field up to a certain spherical harmonic degree N , but does not consider the full frequency spectrum of \mathbf{l} . However, we can use $\hat{\mathbf{l}}^m$ from a GGM, because it centers the difference $\Delta\mathbf{l}$ (in the degrees up to N)

$$\Delta\mathbf{l} = \mathbf{l} - \hat{\mathbf{l}}^m, \tag{38}$$

as introduced in Eq. 14. When a GGM is considered, there are two possibilities: either a GGM from a satellite-only solution that describes the gravity field up to degrees around 200–280 (e.g., GOCO05s; Mayer-Gürr et al. 2015) is used, or a GGM with much higher spatial resolution that already contains terrestrial information like EGM2008 (Pavlis et al. 2012), EIGEN-6c4 (Förste et al. 2014) or XGM2016 (Pail et al. 2018). In both cases, the approximation of the true gravity

field \mathbf{t} by $\hat{\mathbf{I}}$ can be improved by additionally considering the information in the frequencies above the maximum degree of the GGM. In general, large parts of the gravity signal beyond a GGM's resolution are related to the topography (Forsberg and Tscherning 1981; Hirt et al. 2013; Rexer et al. 2016), which is why we use an additional model for the topographic gravity effect above the maximum degree N of the GGM and calculate its effect $\hat{\mathbf{I}}^t$ (with 't' standing for topography) at the input points

$$\hat{\mathbf{I}} = \hat{\mathbf{I}}^m + \hat{\mathbf{I}}^t, \tag{39}$$

and the output points

$$\hat{\mathbf{s}} = \hat{\mathbf{s}}^m + \hat{\mathbf{s}}^t. \tag{40}$$

The same requirements that apply for the definition of $\hat{\mathbf{I}}^m$ also apply for $\hat{\mathbf{I}}^t$, so that the resulting $\Delta\mathbf{I}$ is normally distributed and centered (up to the maximum degree of the topographic gravity model)

$$\Delta\mathbf{I} = \mathbf{I} - \hat{\mathbf{I}}^m - \hat{\mathbf{I}}^t. \tag{41}$$

From a practical point of view it is also important that $\hat{\mathbf{I}}^m$ and $\hat{\mathbf{I}}^t$ can be considered as independent of each other so that the variance propagation from Eq. 39 yields

$$\mathbf{C}_{\hat{\mathbf{I}}} = \mathbf{C}_{\hat{\mathbf{I}}}^m + \mathbf{C}_{\hat{\mathbf{I}}}^t, \tag{42}$$

with $\mathbf{C}_{\hat{\mathbf{I}}}^t$ being the covariance of the topographic gravity model that describes the models uncertainties and correlations. This is analogous to the character of $\mathbf{C}_{\hat{\mathbf{I}}}^m$ for the GGM, and the same is valid for the covariance matrices $\mathbf{C}_{\hat{\mathbf{s}}}$ and $\mathbf{C}_{\hat{\mathbf{s}}}$

$$\begin{aligned} \mathbf{C}_{\hat{\mathbf{s}}} &= \mathbf{C}_{\hat{\mathbf{s}}}^m + \mathbf{C}_{\hat{\mathbf{s}}}^t, \\ \mathbf{C}_{\hat{\mathbf{s}}} &= \mathbf{C}_{\hat{\mathbf{s}}}^m + \mathbf{C}_{\hat{\mathbf{s}}}^t. \end{aligned} \tag{43}$$

As we use the topographic gravity model only in the degrees above the maximum degree N of the GGM, we regard the two models as uncorrelated and write for their degree n

$$\begin{aligned} n^m &\in \{2, N\}, \\ n^t &\in \{N + 1, N_{\max}\}, \end{aligned} \tag{44}$$

where N_{\max} is the maximum degree of $\hat{\mathbf{I}}^t$. Usually, there is neither a normal equation system available for the degrees above a GGM nor another source for a covariance matrix that describes the accuracy of the topographic gravity model. Therefore, without the possibility of deriving direct accuracy or covariance information for the topographic gravity model, we must use the total average $\bar{\mathbf{E}}$ for the derivation of a covariance matrix. The resulting covariance is an approximation for

the accuracy and the correlations of the topographic gravity model and is derived under the assumptions mentioned in Sect. 2.1. This covariance can for example be calculated from the residuals $\Delta\mathbf{I}$, because the topography is usually associated with the largest source of uncertainties in $\Delta\mathbf{I}$. The approach of empirical covariance fitting is quite common in regional geoid modeling and is described in Tscherning and Rapp (1974). Note that the resulting covariance matrices are designed to describe a finite dimensional space and therefore disregard the gravity signal above degree N_{\max} . Adopting this approach our notation changes as follows, again marking the covariance matrices derived from the total average $\bar{\mathbf{E}}$ with a bar, as in Sect. 2.1.

$$\begin{aligned} \mathbf{C}_{\hat{\mathbf{I}}}^t &\approx \bar{\mathbf{C}}_{\hat{\mathbf{I}}}^t \\ \mathbf{C}_{\hat{\mathbf{s}}\hat{\mathbf{I}}}^t &\approx \bar{\mathbf{C}}_{\hat{\mathbf{s}}\hat{\mathbf{I}}}^t \\ \mathbf{C}_{\hat{\mathbf{s}}\hat{\mathbf{s}}}^t &\approx \bar{\mathbf{C}}_{\hat{\mathbf{s}}\hat{\mathbf{s}}}^t \end{aligned} \tag{45}$$

By inserting $\mathbf{C}_{\hat{\mathbf{s}}\hat{\mathbf{I}}}$, $\mathbf{C}_{\hat{\mathbf{I}}}$, $\hat{\mathbf{I}}$ and $\hat{\mathbf{s}}$ from the previous equations into Eq. 30, we obtain the final formulation of RLSC including the GGM and the topographic gravity model

$$\mathbf{s} = \underbrace{(\mathbf{C}_{\hat{\mathbf{s}}\hat{\mathbf{I}}}^m + \bar{\mathbf{C}}_{\hat{\mathbf{s}}\hat{\mathbf{I}}}^t)}_{\text{Part 1}} \underbrace{(\mathbf{C}_{\mathbf{I}\mathbf{I}} + \mathbf{C}_{\hat{\mathbf{I}}}^m + \bar{\mathbf{C}}_{\hat{\mathbf{I}}}^t)^{-1}}_{\text{Part 2}} \underbrace{(\mathbf{I} - \hat{\mathbf{I}}^m - \hat{\mathbf{I}}^t)}_{\text{Part 3}} + \underbrace{\hat{\mathbf{s}}^m + \hat{\mathbf{s}}^t}_{\text{Part 4}}. \tag{46}$$

Since Eq. 46 is very important in the following sections, we look at its various parts in more detail. Part 3 contains the residual input to RLSC subject to the condition that it is centered. Here, the remove step is performed by reducing $\hat{\mathbf{I}}^m$ and $\hat{\mathbf{I}}^t$ from the observations \mathbf{I} . Part 2 describes the uncertainties of part 3 accordingly. Every quantity from the input (\mathbf{I} , $\hat{\mathbf{I}}^m$, $\hat{\mathbf{I}}^t$) has its own covariance matrix ($\mathbf{C}_{\mathbf{I}\mathbf{I}}$, $\mathbf{C}_{\hat{\mathbf{I}}}^m$, $\bar{\mathbf{C}}_{\hat{\mathbf{I}}}^t$). Similarly, we have the covariance matrices between input and output uncertainties in part 1, except that the covariance between the accuracy of the observations and the output \mathbf{s} is missing because the two are assumed to be uncorrelated (Eq. 27). Finally, part 4 describes the restore step in the output functional ($\hat{\mathbf{s}}^m$, $\hat{\mathbf{s}}^t$).

The approach taken from Eq. 46 uses the full covariance information of a GGM up to a certain degree N , and topographic information above, from degree $N + 1$ up to degree N_{\max} . The approach therefore delivers several advantages compared to the approach of Moritz (1980):

1. The observations \mathbf{I} themselves do not have to be centered. Instead, we use the condition that GGM and topographic gravity model have the same offset as the observations \mathbf{I} so that $\mathbf{I} - \hat{\mathbf{I}}^m - \hat{\mathbf{I}}^t$ is centered.
2. The covariance matrices $\mathbf{C}_{\hat{\mathbf{s}}\hat{\mathbf{I}}}^m$ and $\mathbf{C}_{\hat{\mathbf{I}}}$ are neither homogeneous nor isotropic but fit perfectly to a target area and can benefit from the continuously improving quality of (high-resolution) GGMs.

3. This approach uses only residuals as input for LSC, because it can be shown that this yields the best results (see Sect. 2.2).
4. RLSC can give a realistic formal error estimate, because with the inclusion of the GGM uncertainties all the stochastic information is included in the resulting error covariance matrix \mathbf{E}_{ss} , which is calculated (analogously to Eq. 46) by inserting \mathbf{C}_{ll}^m , \mathbf{C}_{sl}^m and \mathbf{C}_{ss}^m into Eq. 32

$$\begin{aligned} \mathbf{E}_{ss} &= \mathbf{C}_{\text{ss}} - \mathbf{C}_{\text{sl}} (\mathbf{C}_{\text{ll}} + \mathbf{C}_{\text{ll}}^t)^{-1} \mathbf{C}_{\text{sl}}^T \\ &= (\mathbf{C}_{\text{ss}}^m + \bar{\mathbf{C}}_{\text{ss}}^t) - (\mathbf{C}_{\text{sl}}^m + \bar{\mathbf{C}}_{\text{sl}}^t) \\ &\quad \times (\mathbf{C}_{\text{ll}} + \mathbf{C}_{\text{ll}}^m + \bar{\mathbf{C}}_{\text{ll}}^t)^{-1} (\mathbf{C}_{\text{sl}}^m + \bar{\mathbf{C}}_{\text{sl}}^t)^T. \end{aligned} \tag{47}$$

In comparison with the existing literature that has already included accuracy information from a satellite-only model (e.g., Haagmans and van Gelderen 1991; Pail et al. 2010; Sansò 2013) our approach still maintains the advantages 1 and 2. Point 4 is only advantageous in comparison with approaches that do not include all stochastic parts in LSC (e.g., Forsberg and Tscherning 1981; Hofmann-Wellenhof and Moritz 2006; Rieser 2015).

3 Data and simulation concept

We show the benefit of including full covariance matrices from a high-resolution GGM in collocation by a comparison between RLSC (Eq. 46) and a comparable approach without GGM covariance matrices, which we refer to as standard LSC. We derive standard LSC

$$\bar{\mathbf{s}} = \bar{\mathbf{C}}_{\text{sl}}^t (\mathbf{C}_{\text{ll}} + \bar{\mathbf{C}}_{\text{ll}}^t)^{-1} (\mathbf{1} - \hat{\mathbf{I}}^m - \hat{\mathbf{I}}^t) + \hat{\mathbf{s}}^m + \hat{\mathbf{s}}^t, \tag{48}$$

from the approach by Moritz (1980) (Eq. 12), but include an RCR approach for the GGM and the topographic gravity model that is analogous to Eq. 46. Standard LSC is thereby equivalent to RLSC (Eq. 46) except that the two covariance matrices \mathbf{C}_{ll}^m and \mathbf{C}_{sl}^m are missing, because the GGM is either assumed to be error-free or its noise component is implicitly included in the model covariance function, which is used to fit the empirical covariance function (Tscherning and Rapp 1974). In case of an error-free GGM the corresponding error covariance matrix $\bar{\mathbf{E}}_{\text{ss}}$ results in accuracy estimates of $\bar{\mathbf{s}}$ that are overly optimistic

$$\bar{\mathbf{E}}_{\text{ss}} = \bar{\mathbf{C}}_{\text{ss}}^t - \bar{\mathbf{C}}_{\text{sl}}^t (\mathbf{C}_{\text{ll}} + \bar{\mathbf{C}}_{\text{ll}}^t)^{-1} \bar{\mathbf{C}}_{\text{sl}}^{tT}. \tag{49}$$

The comparison of the two methods works best within a synthetic test case scenario that allows us to compute the residuals of the two methods by knowing the pre-defined truth. Moreover, it makes it possible to evaluate and assess the

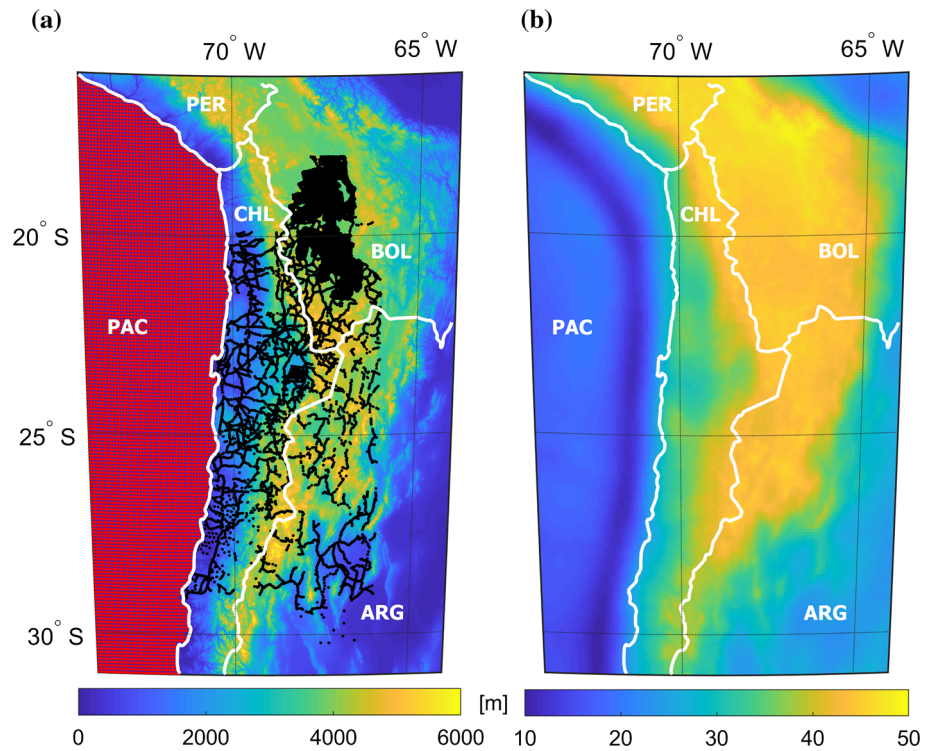
formal error estimate of the stochastic part of the collocation (compare RLSC: Eq. 47 and standard LSC: Eq. 49). To obtain realistic results from a synthetic test case, we add noise to the observations and to the GGM (as shown below).

The synthetic test case is calculated for one of the most common challenges of regional geoid modeling, i.e., the calculation of the geoid from gravity anomalies given at selected input points. As the calculation should be an evaluation test for a real geoid computation, we use the input positions of actual gravity observations for our synthetic test case. Output is a regular grid of geoid heights in the target area, the South American Andes. This is a useful test area for the study since the Andes are one of the most demanding regions worldwide in terms of gravity signal variations, heterogeneous data distribution, and topographic effects. Also, we have access to the actual terrestrial database for this area (Hosse et al. 2014) and can therefore realistically simulate the data distribution on land.

The terrestrial gravity observation points are inhomogeneously distributed in an area between longitude $[-72^\circ$ to $-66^\circ]$ and latitude $[-29^\circ$ to $-18^\circ]$ that is the northern part of Chile (CHL), north-western Argentina (ARG) and south-western Bolivia (BOL, Fig. 1a). Furthermore, we add altimetry observations to cover the ocean region of the test area. The altimetry observations are given as a regular grid with $5'$ spacing in the Pacific Ocean (PAC) bordered by the -74° longitude meridian and the -31° parallel. Altimetric gravity data on a regular grid are available from various ocean products, e.g., DTU13 (Andersen et al. 2015) or Sandwell and Smith (2009) and can be found for download at the corresponding websites. The distribution of the input points in Fig. 1a is displayed together with the terrain height. The image shows the Pacific Ocean to the West and the main ridge of the Andes from north to south. The test case includes areas with quite dense terrestrial observations, while others show large data gaps. Overall, there are 14,613 gravity anomaly input points with 7814 from terrestrial observations and 6799 altimetry grid points. As output, geoid heights \mathbf{N} are estimated for the whole study area as a regular $5'$ grid, which results in 21,901 output points (Fig. 1b).

As a GGM we use the XGM2016 (Pail et al. 2018), because we have its full normal equation system available that allows the calculation of the covariance matrices \mathbf{C}_{ll}^m , \mathbf{C}_{sl}^m and \mathbf{C}_{ss}^m (Eq. 37), as well as input and output functionals $(\hat{\mathbf{I}}^m, \hat{\mathbf{s}}^m)$ in Eq. 36. The XGM2016 is a combined gravity field model up to degree 719 which uses relative regional weighting for the combination of terrestrial and satellite information. Compared to the GOCO05c model (Fecher et al. 2017), the XGM2016 includes an improved terrestrial data set provided by the National Geospatial-Intelligence Agency (NGA). In our opinion the XGM2016 is one of the most consistently calculated high-resolution GGMs, and its good

Fig. 1 LSC input points and pre-defined truth of the test scenario with borders as white lines. **a** Terrain heights with the distribution of the input points with altimetry observations (red dots) and terrestrial measurements (black dots). **b** Regular 5' resolution grid of geoid heights that are the pre-defined truth \mathfrak{s} for the synthetic test case



performance in comparison with other high-resolution gravity field models such as EGM2008 (Pavlis et al. 2012), EIGEN-6c4 (Förste et al. 2014) and GOCO05c (Fecher et al. 2017) is demonstrated in Pail et al. (2018). In a post-analysis of the variance–covariance matrix of XGM2016, however, we found out that the accuracy estimates in the higher degrees (beyond the resolution of the satellite data) underestimate the true noise behavior. The regionally varying weights of XGM2016 have been computed empirically from comparison of satellite and low-pass filtered ground data (Pail et al. 2018). This procedure ensures an adequate relative weighting of satellite and ground data, but implicitly disregards signal content in the high degrees. In a new version of XGM2016, which shall be released soon, we will take this omission error into account by means of scaling the error estimates by their high-frequency signal content. From this analysis, we consider a factor of 3 as a reasonable value to calibrate the error estimates in the area of our synthetic test case. Therefore, we scale the XGM2016 accuracy estimates in Sects. 4.1 and 4.2 by a factor of 3 and hence must increase the elements of the covariance matrices $C_{\hat{\mathbf{I}}\hat{\mathbf{I}}}^m$, $C_{\hat{\mathbf{S}}\hat{\mathbf{S}}}^m$ and $C_{\hat{\mathbf{I}}\hat{\mathbf{S}}}^m$ by a factor of 9. However, in Sect. 4.3 we present results with the original XGM2016 accuracy and thus investigate the impact of the accuracy of the GGM.

For the definition of the true gravity signal, we choose a XGM2016 and EIGEN-6c4 combination model [‘GOCE-OGMOC’, Gruber and Willberg (2019)] up to degree 2190 and calculate \mathfrak{s} and \mathfrak{t} from it. The main reason for using this model is that we can be sure it does not contain sys-

tematic errors relative to the XGM2016 model because the long wavelength parts are identical. The geoid heights \mathfrak{s} that we use as pre-defined truth, and to which we subsequently compare our results, are presented in Fig. 1b. In the target area, the geoid heights vary from 10 m in the Atacama Trench up to almost 50 m in the plateau of Bolivia. The true gravity anomalies \mathfrak{t} are used to calculate the simulated gravity observations \mathbf{I} by adding white noise \mathbf{n} which is calculated from a random noise vector \mathbf{e}^1 and the accuracy of the observations σ^1

$$\mathbf{I} = \mathfrak{t} + \mathbf{n} = \mathfrak{t} + \sigma^1 \mathbf{e}^1. \tag{50}$$

σ^1 is also used in the covariance matrix $C_{\mathbf{I}\mathbf{I}}$ of the observations where we assume the accuracies of different observations \mathbf{I} to be uncorrelated and therefore obtain the diagonal matrix $C_{\mathbf{I}\mathbf{I}}$

$$C_{\mathbf{I}\mathbf{I}} = \sigma^1 \mathbf{I}. \tag{51}$$

We must consider this as a simplification because we assume that we know the accuracy σ^1 of the input observations which is not guaranteed in reality.

For $\hat{\mathbf{I}}^t$ and $\hat{\mathbf{S}}^t$ we use a spherical harmonic synthesis from the topographic gravity model dV_ELL_Earth2014 (Rexer et al. 2016) from degree $N + 1$ to N_{\max} . Note that it is not necessary for $\hat{\mathbf{I}}^t$ (or $\hat{\mathbf{S}}^t$) to contain all remaining gravity signals above the degree N of the GGM provided it is without systematic error and independent of $\hat{\mathbf{I}}^m$ (conditions in the

Table 1 Overview of all quantities, their definition and source in our synthetic test case scenario

Quantity	Description	Source	Equations
\mathbf{t}	Pre-defined truth synthesized in input functional	GOCE-OGMOC	–
\mathbf{s}	Pre-defined truth synthesized in output functional	GOCE-OGMOC	–
$\mathbf{C}_{\hat{\mathbf{I}}}^m$	GGM: error covariance function for input points	XGM2016	37
$\mathbf{C}_{\hat{\mathbf{S}}}^m$	GGM: error covariance function for input and output	XGM2016	37
$\mathbf{C}_{\hat{\mathbf{S}}}^m$	GGM: error covariance function for output points	XGM2016	37
$\hat{\mathbf{I}}^m$	GGM: synthesized in input functional (remove step)	XGM2016	36
$\hat{\mathbf{S}}^m$	GGM: synthesized in output functional (restore step)	XGM2016	36
N	Maximum degree of the GGM	XGM2016	44
\mathbf{I}^n	Colored noise of GGM at input points (synthetic case only)	White noise and XGM2016	56
\mathbf{s}^n	Colored noise of GGM at output points (synthetic case only)	White noise and XGM2016	56
$\boldsymbol{\kappa}^n$	Combined colored noise of GGM (synthetic case only)	White noise and XGM2016	54
$\bar{\mathbf{C}}_{\hat{\mathbf{I}}}^t$	Topo. gravity: error covariance function for input points	Fit to empirical covariance	45
$\bar{\mathbf{C}}_{\hat{\mathbf{S}}}^t$	Topo. gravity: error covariance function for input and output	Fit to empirical covariance	45
$\bar{\mathbf{C}}_{\hat{\mathbf{S}}}^t$	Topo. gravity: error covariance function for output points	Fit to empirical covariance	45
$\hat{\mathbf{I}}^t$	Topo. gravity: synthesized in input functional (remove step)	dV_ELL_Earth2014	39
$\hat{\mathbf{S}}^t$	Topo. gravity: synthesized in output functional (restore step)	dV_ELL_Earth2014	40
N_{\max}	Maximum degree of the topographic gravity model	dV_ELL_Earth2014	44
σ^l	Assumed accuracy of input observations	Accuracy of observations	50
$\mathbf{C}_{\hat{\mathbf{I}}}$	Error covariance function of observations, diagonal matrix	Accuracy of observations	51
\mathbf{e}^l	White noise vector (synthetic case only)	White noise	50
\mathbf{e}^m	White noise vector (synthetic case only)	White noise	54

definition of Sect. 2.4). An overview of all quantities of the synthetic test case can be found in Table 1.

Finally, we add noise to the GGM. Since the XGM2016 model uses regional varying weighting, colored noise that actually describes the regionally varying accuracy of the model is added in terms of a (random) realization based on the variance–covariance information. For the calculation of this covariance, we combine the observations \mathbf{I} and the output \mathbf{s} in one vector $\boldsymbol{\kappa}$

$$\boldsymbol{\kappa} = \begin{pmatrix} \mathbf{I} \\ \mathbf{s} \end{pmatrix}, \tag{52}$$

and propagate the variance–covariance matrix of the GGM $\mathbf{C}_{\hat{\mathbf{I}}}^m$ to the combined covariance matrix $\mathbf{C}_{\hat{\boldsymbol{\kappa}}}^m$ of input and output by attaching the three formulas of Eq. 37 to give

$$\mathbf{C}_{\hat{\boldsymbol{\kappa}}}^m = \mathbf{A}_{\boldsymbol{\kappa}}^f \mathbf{C}_{\hat{\mathbf{I}}}^m \mathbf{A}_{\boldsymbol{\kappa}}^{fT}, \tag{53}$$

where $\mathbf{A}_{\boldsymbol{\kappa}}^f$ is the design matrix for the transformation from SH coefficients to the input and output points $\boldsymbol{\kappa}$. We obtain the colored noise $\boldsymbol{\kappa}^n$ of input and output by multiplying a random vector \mathbf{e}^m with white noise characteristics and the Cholesky decomposition of the combined covariance matrix $\mathbf{C}_{\hat{\boldsymbol{\kappa}}}^m$

$$\boldsymbol{\kappa}^n = \text{chol}(\mathbf{C}_{\hat{\boldsymbol{\kappa}}}^m) \mathbf{e}^m = \text{chol} \begin{pmatrix} \mathbf{C}_{\hat{\mathbf{I}}}^m & \mathbf{C}_{\hat{\mathbf{S}}}^{mT} \\ \mathbf{C}_{\hat{\mathbf{S}}}^m & \mathbf{C}_{\hat{\mathbf{S}}}^m \end{pmatrix} \mathbf{e}^m, \tag{54}$$

which is defined by

$$\mathbf{X} = \text{chol}(\mathbf{X}) \text{chol}(\mathbf{X})^T, \tag{55}$$

where \mathbf{X} is a positive definite matrix (e.g., covariance matrix). Consequently, we obtain the noise of the GGM for the input \mathbf{I}^n and the output \mathbf{s}^n analogously to the definition in Eq. 52 by

$$\boldsymbol{\kappa}^n = \begin{pmatrix} \mathbf{I}^n \\ \mathbf{s}^n \end{pmatrix}, \tag{56}$$

and add them correspondingly to $\hat{\mathbf{I}}^m$ and $\hat{\mathbf{S}}^m$. Thus, for a synthetic test case we adjust the formula of RLSC (Eq. 46) with the inclusion of the observation noise \mathbf{n} (Eq. 50) and the noise of the XGM2016 model \mathbf{I}^n and \mathbf{s}^n (Eqs. 54, 56)

$$\mathbf{s} = (\mathbf{C}_{\hat{\mathbf{S}}}^m + \bar{\mathbf{C}}_{\hat{\mathbf{S}}}^t) (\mathbf{C}_{\hat{\mathbf{I}}} + \mathbf{C}_{\hat{\mathbf{I}}}^m + \bar{\mathbf{C}}_{\hat{\mathbf{I}}}^t)^{-1} ((\mathbf{t} + \mathbf{n}) - (\hat{\mathbf{I}}^m + \mathbf{I}^n) - \hat{\mathbf{I}}^t) + (\hat{\mathbf{S}}^m + \mathbf{s}^n) + \hat{\mathbf{S}}^t, \tag{57}$$

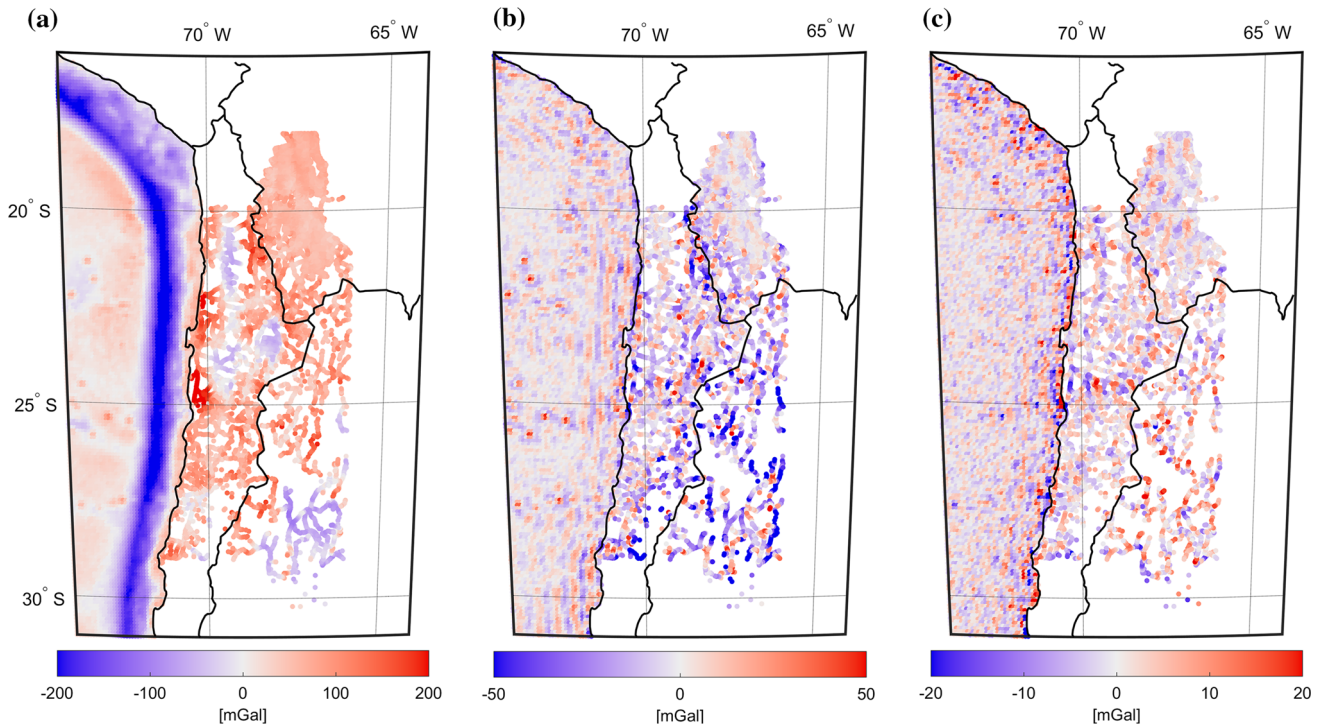


Fig. 2 LSC remove step for the gravity anomalies: **a** terrestrial observations with $\sigma_n = 1$ mGal, **b** observations after reduction of XGM2016 model, **c** LSC input $\Delta \mathbf{l}$ after reducing XGM2016 and topographic gravity

and analogously, for standard LSC from Eq. 48

$$\bar{s} = \bar{\mathbf{C}}_{\hat{s}}^t (\mathbf{C}_{ll} + \bar{\mathbf{C}}_{ll}^t)^{-1} ((\mathbf{t} + \mathbf{n}) - (\hat{\mathbf{I}}^m + \mathbf{I}^n) - \hat{\mathbf{I}}^t) + (\hat{s}^m + \mathbf{s}^n) + \hat{s}^t. \tag{58}$$

In both cases, the stochastic part of the collocation does not change, so that the calculation of the error covariance matrices \mathbf{E}_{ss} (Eq. 47) and $\bar{\mathbf{E}}_{\bar{s}\bar{s}}$ (Eq. 49) remain unchanged in the synthetic test case.

The effect of the remove step in Eqs. 57 and 58 is presented in Fig. 2, where the observations always include a white noise of $\sigma^1 = 1$ mGal (see Eq. 50). The XGM2016 model up to degree $N = 719$ contains the colored noise that is calculated from the Cholesky decomposition (Eq. 54), and the topographic gravity reduction is used from $N + 1$ to 2190. Figure 2a shows the original, noisy observations \mathbf{l} . We reduce the observations \mathbf{l} first by the high-resolution XGM2016 model $(\hat{\mathbf{I}}^m + \mathbf{I}^n)$ (Fig. 2b) and afterwards also by the gravity signal that is related to the topography, resulting in the residual input vector $\mathbf{l} - (\hat{\mathbf{I}}^m + \mathbf{I}^n) - \hat{\mathbf{I}}^t$ (Fig. 2c). Note that the color scale decreases significantly between Fig. 2a and Fig. 2c. This is also apparent in Table 2, which shows the mean value and the standard deviation of the corresponding data sets in Fig. 2. Regarding its standard deviation (SD), the signal is reduced by about 80% by subtracting the XGM2016 model and more than 90% in combination with the topography. With a mean value of only 0.2 mGal the condition

of a centered LSC input is almost fulfilled in this case. In our numerical simulation, the final LSC input contains the noise of the observations and the GGM as well as the inaccuracy of the topographic gravity model. These three effects are modeled in the related error covariance matrices of our approach (Eq. 57). The inaccuracy of the topographic gravity model thereby also includes density anomalies in the spectral range from $N + 1$ to N_{\max} , which are contained in the residual observations. These anomalies are not adequately represented in the topographic gravity model, because it assumes a constant topographic density (Rexer 2017, Chapter 3.2).

Currently we do not have accuracy information for the topographic gravity model (see Sect. 2.4) and this kind of information is not available for any of the topographic gravity models (Rexer et al. 2016; Grombein et al. 2016). However, because we assume the largest part of the LSC input results from differences between the topographic gravity model and the observations in the high frequencies (as they contain also the effect of density anomalies), we calculate a Model Covariance Function (MCF) that fits the LSC input. This is considered to be a standard approach in LSC which is used for the calculation with signal degree variances (Moritz 1980, Chapter 12) as well as for empirical covariance fitting with the most common approach by Tscherning and Rapp (1974). The result is an isotropic and homogeneous covariance matrix for the spectral range above degree 719 that fits

Table 2 Consistent numerical analysis of the LSC remove step in Fig. 2

Signal description	Notation	Mean value (mGal)	SD (mGal)	Figures
Observations	$\mathbf{l} = \mathbf{t} + \mathbf{n}$	10.2	78.7	2a
Reduced by XGM2016 only	$\mathbf{l} - (\hat{\mathbf{l}}^m + \mathbf{l}^n)$	-3.3	15.2	2b
Reduced by XGM2016 + topographic gravity	$\mathbf{l} - (\hat{\mathbf{l}}^m + \mathbf{l}^n) - \hat{\mathbf{l}}^t$	0.2	5.5	2c

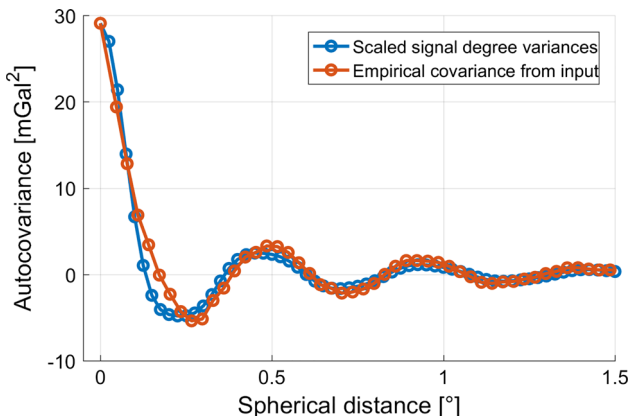


Fig. 3 Empirical covariance function that is calculated from the LSC residuals in the target area (red) and the scaled covariance from signal degree variances (blue) as it is used for LSC. Both covariance functions are shown dependent on the spherical distance between two points

to our input residuals. In general, we calculate the covariance matrices $\bar{\mathbf{C}}_{\hat{\mathbf{l}}\hat{\mathbf{l}}}^t$ and $\bar{\mathbf{C}}_{\hat{\mathbf{s}}\hat{\mathbf{s}}}^t$ from signal degree variances and refer to Moritz (1980) for more details. However, global signal degree variance models describe an average Earth, but the South American Andes are not an average area in terms of gravity signal (due to large topographic masses). Thus, we have to use a scale factor to fit model degree variances (blue, Fig. 3) to the Empirical Covariance Function (ECF) of the LSC input residuals (red). In Fig. 3, we calculate signal degree variances, according to our data simulation, from the difference between the GOCE-OGMOC and the dV_ELL_Earth2014 model from degree 720 to 2190 and scale them by a factor of 4.25. Figure 3 then shows the ECF and MCF in dependence of the spherical distance between two points. In this case the correlation length amounts to only 0.12°.

4 Results of the synthetic test scenario

Section 3 describes the method, the parameters and the sources that are used to evaluate RLSC (Eq. 57) in comparison with standard LSC (Eq. 58). Both methods use the RCR concept where a GGM and the topographic gravity are removed before the collocation, and their effects are restored (to the output functional) afterwards. For the calculation we

set the degree N of the GGM first and use the topographic gravity model always from degree $N + 1$ to $N_{\max} = 2190$. The results of \mathbf{s} (or $\bar{\mathbf{s}}$) are compared with the assumed truth \mathbf{s} , and the difference indicates the accuracy of the collocation result under these pre-defined conditions. In terms of numerical classification we define the Root Mean Square (RMS) over a target area with n^{points} points as a quality criterion for the LSC result \mathbf{s} (or $\bar{\mathbf{s}}$)

$$\text{RMS} = \sqrt{\frac{\sum_{\text{points}} (\mathbf{s} - \bar{\mathbf{s}})^2}{n^{\text{points}}}} \tag{59}$$

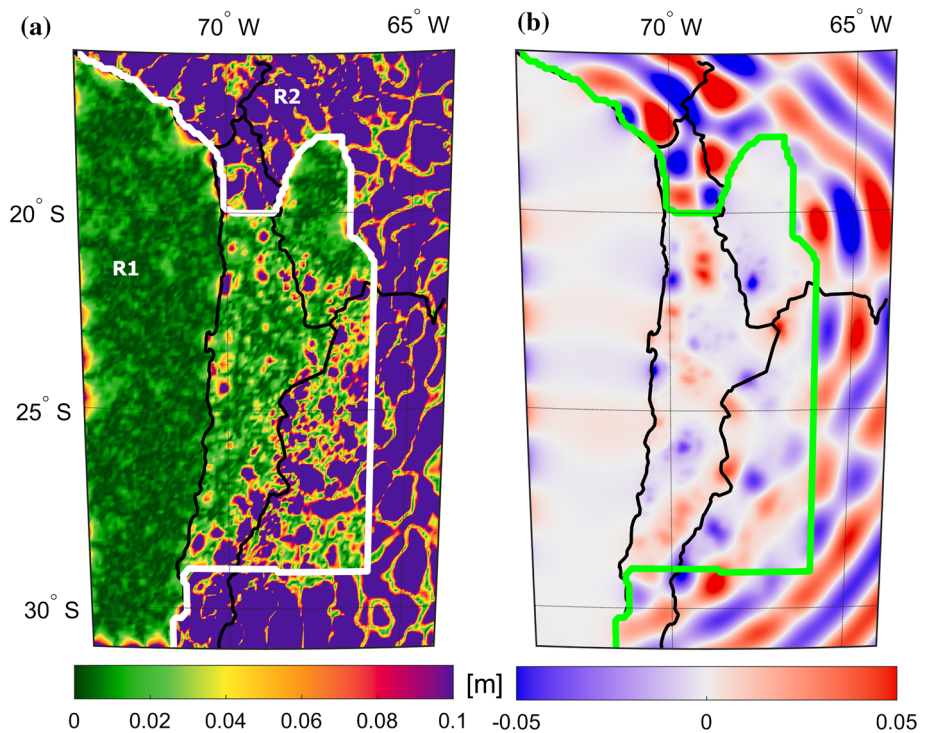
We use an equivalent formula to characterize the Mean estimated standard deviation (MSD), which describes the stochastic accuracies and is derived from \mathbf{E}_{ss} (or $\bar{\mathbf{E}}_{\text{ss}}$) with $\text{diag}(\mathbf{X})$ giving the main diagonal of a square matrix \mathbf{X}

$$\text{MSD} = \sqrt{\frac{\sum_{\text{points}} \text{diag}(\mathbf{E}_{\text{ss}})}{n^{\text{points}}}} \tag{60}$$

4.1 Simulation with satellite-only model resolution

At first we compare LSC for calculations with the XGM2016 model but use the model only up to degree 200 (case A). Consequently, RLSC resembles other approaches in which covariance functions from satellite-only global gravity fields are included to LSC (e.g., Pail et al. 2010; Sansò 2013). However, the actual computation of the covariance matrices in our case is still different (Eq. 37). Standard LSC in case A is similar to LSC approaches that do not account for the accuracy of the GGM (e.g., Rieser 2015; Hofmann-Wellenhof and Moritz 2006). The main reason why it is so common to use a GGM up to degree of 180–250 in LSC is the high accuracy of GGMs in this frequency range (Gruber et al. 2011), which is mainly due to the GOCE mission (Drinkwater et al. 2003). Thus, in the first case we use the XGM2016 model with $n^m \in \{2, 200\}$ for all quantities with the superscript ‘m’, and $n^t \in \{201, 2190\}$ accordingly. The accuracy of the input observations σ_n is assumed to be 1 mGal. For the calculations in Sects. 4.1 and 4.2, the accuracy of the XGM2016 model is multiplied by a factor of 3 (see Sect. 3). It is added

Fig. 4 Case A: Geoid height residuals with the XGM2016 model up to degree 200. Presented is **a** the absolute difference between the pre-defined truth \mathfrak{s} and the RLSC result \mathfrak{s} , **b** the difference between the result of standard LSC $\bar{\mathfrak{s}}$ and RLSC \mathfrak{s}



as described in Sect. 3 but limited to degree 200 in case A. An overview of all quantities is given in Table 1.

The collocation result \mathfrak{s} of RLSC from Eq. 57 in case A is presented as an absolute geoid height difference (residuals) to the pre-defined truth \mathfrak{s} in Fig. 4a. In Fig. 4 and the following images, we separate a region with terrestrial data coverage (R1, left side) from an area without ground data (R2, right side) by a white line, because we see large differences between these two regions. For the interpretation we focus mainly on the region R1. In Fig. 4a, we see a high correlation between the LSC residuals and the positions of the input observations (see Fig. 1a): in the Pacific Ocean and the bulge in the north we have dense observations and therefore only small residuals mainly below 1 cm. In region R2, the residuals amount to more than 10 cm which is also the case for large parts of R1 in the Argentinian area (southeast). We conclude that the number of terrestrial observations in this area is not dense enough to describe the geoid height signals above degree 200. The RMS (Eq. 59) of the region R1 accounts for 6.0 cm, and is obviously significantly larger in R2.

In case A, the RLSC results \mathfrak{s} (Fig. 4a) and standard LSC $\bar{\mathfrak{s}}$ (Eq. 58) show almost the same RMS (Table 3) and only small differences among each other. The difference $\bar{\mathfrak{s}}$ minus \mathfrak{s} in Fig. 4b shows maximum values of about ± 5.0 cm, but these values occur to a large extent in areas without observations. In areas with dense gravity observations (e.g., Pacific Ocean) the differences between the two methods are of the order of just a few millimeters. The reason for the differences being

so small is the fact that the extracted variances from $\mathbf{C}_{\text{II}}^{\text{m}}$ and $\mathbf{C}_{\text{SI}}^{\text{m}}$ of the GGM are insignificantly small compared to the corresponding variances of the topographic gravity in $\bar{\mathbf{C}}_{\text{II}}^{\text{t}}$ and $\bar{\mathbf{C}}_{\text{SI}}^{\text{t}}$. Therefore, $\bar{\mathbf{C}}_{\text{II}}^{\text{m}}$ and $\bar{\mathbf{C}}_{\text{SI}}^{\text{m}}$ from RLSC do not have an essential effect on the summation in Eq. 57.

$$\begin{aligned} \text{diag}(\mathbf{C}_{\text{II}}^{\text{m}}) &\ll \text{diag}(\bar{\mathbf{C}}_{\text{II}}^{\text{t}}) \\ \text{diag}(\mathbf{C}_{\text{SI}}^{\text{m}}) &\ll \text{diag}(\bar{\mathbf{C}}_{\text{SI}}^{\text{t}}) \end{aligned} \quad (61)$$

This is demonstrated in Fig. 5 which shows the variances that are extracted from $\bar{\mathbf{C}}_{\text{II}}^{\text{t}}$ (Fig. 5a) and $\mathbf{C}_{\text{II}}^{\text{m}}$ (Fig. 5b). The variances from the topographic gravity in $\bar{\mathbf{C}}_{\text{II}}^{\text{t}}$ are in the order of 1000 times larger than the variances of the GGM in $\mathbf{C}_{\text{II}}^{\text{m}}$. We can conclude that in case A the additional benefit of adding the covariance matrices $\mathbf{C}_{\text{II}}^{\text{m}}$ and $\mathbf{C}_{\text{SI}}^{\text{m}}$ to LSC is small. This is also the explanation why LSC approaches often ignore the accuracy of a satellite-only resolution GGM completely (e.g., Hofmann-Wellenhof and Moritz 2006; Rieser 2015).

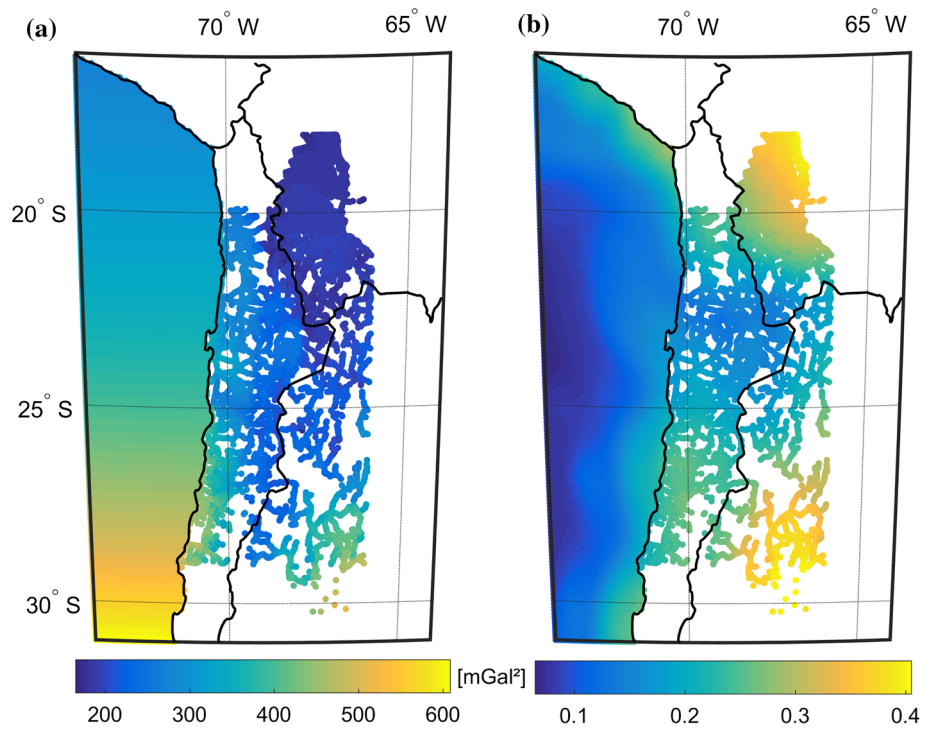
4.2 Simulation with full GGM resolution

However, this changes in case B where we use the full degree $N = 719$ of the XGM2016 model for reduction ($n^{\text{m}} \in \{2, 719\}$) and thus apply the topographic gravity for $n^{\text{t}} \in \{720, 2190\}$. In principle, the procedure remains the same, but we would like to emphasize that this set-up increases all matrix elements in $\mathbf{C}_{\text{II}}^{\text{m}}$, $\mathbf{C}_{\text{SI}}^{\text{m}}$ and $\mathbf{C}_{\text{SS}}^{\text{m}}$, and therefore also the noise of the XGM2016 model (see Eq. 54).

Table 3 Overview of the three synthetic test cases and the numerical results for region R1

Case	Sections	N	Signal	Method	RLSC (cm)	Standard LSC (cm)	Figures
A	4.1	200	Residuals	RMS	6.0	6.1	4
		200	Formal error	MSD	5.2	5.2	–
B	4.2	719	Residuals	RMS	3.9	6.9	6
		719	Formal error	MSD	3.6	2.2	7
C	4.3	719	Residuals	RMS	2.9	3.3	8
		719	Formal error	MSD	2.6	2.2	–

Fig. 5 Case A: Comparison of the extracted variances that are used in RLSC. **a** Variances extracted from the covariance matrix \hat{C}_{Π}^t of the topographic gravity model which depends only on latitude and height. **b** Regional varying variance elements from the covariance matrix C_{Π}^m of the XGM2016 model (to degree 200)

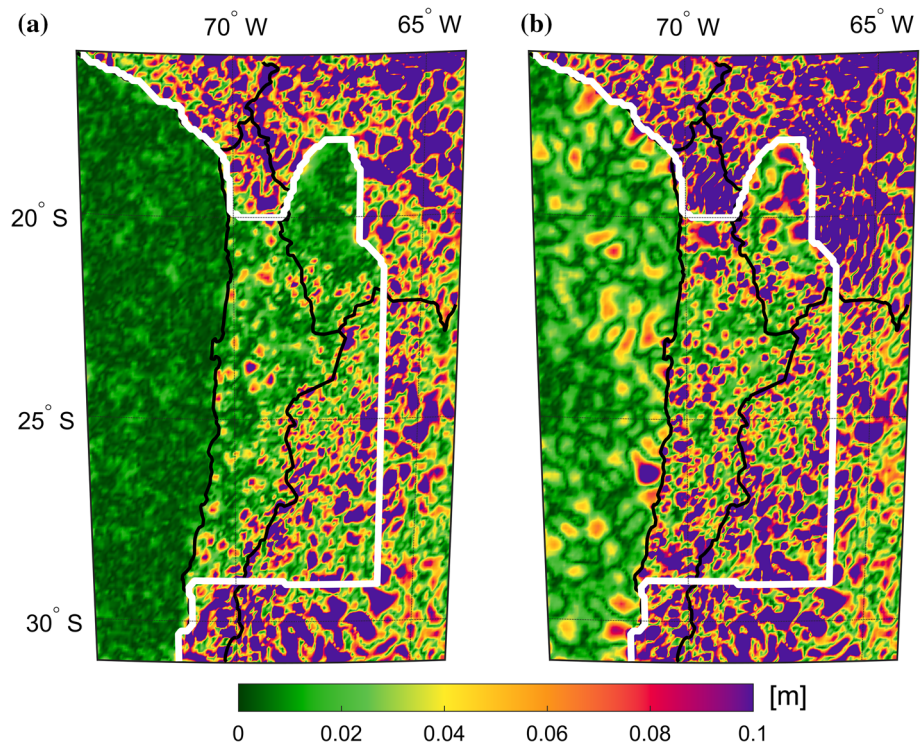


The results of a collocation with XGM2016 to full degree (case B) are visualized in Fig. 6, where we show again the absolute differences to the pre-defined truth \mathfrak{s} . From this point, we retain the form in which we present RLSC with GGM covariance (Eq. 57) on the left-hand side (Fig. 6a) and standard LSC (Eq. 58) on the right-hand side (Fig. 6b). It is obvious that RLSC performs much better in case B. In Fig. 6a, we again see a high correlation with the distribution of the input points. In areas with dense terrestrial observation, e.g., the Pacific Ocean or the bulge in the north, the residuals are mainly below 1 cm. The residuals over the well-covered Chilean area are much smaller than on the Argentinian side, which also results from the corresponding point distributions. In the region R2 the residuals are largest and often above 10 cm. In Fig. 6b, we have in general much larger residuals, so that even areas with dense gravity observations show residuals of at least 2 cm. The higher residuals primarily result from the noise of the GGM since standard LSC regards the noisy XGM2016 model as error-free and therefore fully reflects its error in the result. The RMS of standard LSC in

region R1 accounts for 6.9 cm, while the one of RLSC is only 3.9 cm (Table 3).

In summary, RLSC and standard LSC perform very similarly with a satellite-only resolution GGM in case A, but when using a high-resolution GGM as in case B, there are significant improvements when including the GGM covariance (Table 3, Fig. 6). Furthermore, the benefit of including a high-resolution GGM itself is demonstrated when we compare the RLSC result in case B (Fig. 6a) with the result in case A (Fig. 4a). Even with the much higher error from the GGM in case B, the RMS for RLSC in region R1 is reduced from 6.0 to 3.9 cm. This improvement results at least partly from the area with sparse terrestrial measurements in Argentina that has clearly higher residuals in case A (Fig. 4a). However, even areas with small data gaps which are common in mountainous areas and the edges of observed areas benefit highly from the inclusion of a high-resolution GGM in RLSC. The latter is for example visible at the southern end of the Pacific Ocean where case A clearly shows edge effects while case B does not. Standard LSC, on the

Fig. 6 Case B: Geoid height residuals with the XGM2016 model that is the absolute difference between the pre-defined truth \mathfrak{s} and **a** the RLSC result \mathfrak{s} , **b** the standard LSC result $\bar{\mathfrak{s}}$



other hand, performs worse in case B, and its RMS increases due to the noise \mathbf{I}^n of the GGM from 6.1 cm in case A to 6.9 cm in case B. We conclude that, in contrast to standard LSC, RLSC is able to handle the noise in the GGM and gives good results in areas with a sufficient number of observations.

Figure 7 shows the formal error of case B, which is derived from the error covariance matrix $\mathbf{E}_{\mathfrak{ss}}$ or respectively $\bar{\mathbf{E}}_{\mathfrak{ss}}$ as square root of the main diagonal elements (Eq. 60). The difference between Fig. 7a and Fig. 7b results from the neglected covariance matrices $\mathbf{C}_{\mathfrak{ll}}^m$ and $\mathbf{C}_{\mathfrak{sl}}^m$ in Eq. 58, and since covariance matrices are positive definite, the estimated error for standard LSC (Fig. 7b) is always smaller than the one from RLSC (Fig. 7a). The corresponding MSD (Eq. 60) in region R1 is 3.6 cm for RLSC and 2.2 cm for standard LSC. Thus, we see that the residuals and the formal errors agree much better (see Table 3) for RLSC (Figs. 6a + 7a) than for standard LSC (Figs. 6b + 7b). We again point out the Pacific Ocean and the bulge in Bolivia where in both cases the dark green values of Fig. 7b do not fit to the corresponding error in Fig. 6b. In contrast, we see that for RLSC essentially all peaks in the residuals (Fig. 6a) are indicated by higher values in Fig. 7a as well, which demonstrates that the formal error of RLSC fits much better to its residuals. We conclude that standard LSC cannot realistically represent the formal error since the accuracy of the GGM is not included. Therefore, the result of $\bar{\mathbf{E}}_{\mathfrak{ss}}$ is always too optimistic. The consistent calculation of $\mathbf{E}_{\mathfrak{ss}}$ is considered as a main advantage of RLSC.

4.3 Simulation with a different XGM2016 accuracy

To analyze the behavior of RLSC in dependence of the accuracy of the GGM, we repeat the computations with the original XGM2016 accuracy, i.e., without multiplying it by a factor of 3. Therefore, we recalculate case B with the original XGM2016 covariance matrices $\mathbf{C}_{\mathfrak{ll}}^m$, $\mathbf{C}_{\mathfrak{sl}}^m$ and $\mathbf{C}_{\mathfrak{ss}}^m$ and name it case C. Note, that this will generally improve the results since the downscaling of the covariance matrices also decreases the noise \mathbf{I}^n and \mathfrak{s}^n of the GGM which is used in the RCR step.

Figure 8 shows again the resulting absolute geoid height differences between the results of RLSC and standard LSC to the pre-defined truth \mathfrak{s} . At first glance the two images in Fig. 8 look similar. As in case B, in general we have small errors in the Pacific Ocean, medium errors in the land areas with observations, and the largest errors in region R2. But nevertheless, we see that the result of RLSC (Fig. 8a) is better than standard LSC (Fig. 8b). The RMS from region R1 amounts to 2.9 cm (Fig. 8a) and 3.3 cm (Fig. 8b), respectively. Especially, the dark green area in the Pacific which indicates residuals below 1 cm is more uniform in Fig. 8a. Also, for RLSC the bulge in the north shows mainly residuals below 1 cm, while for standard LSC it shows much higher residuals.

Table 3 summarizes the RMS and MSD values of the three synthetic test cases in region R1, from which the following conclusions can be drawn. Generally, in all three test cases RLSC performs better than standard LSC. However,

Fig. 7 Case B: Formal error of the geoid height calculation. This derives **a** from \mathbf{E}_{ss} for RLSC, **b** from $\bar{\mathbf{E}}_{ss}$ for standard LSC, as the square root of the main diagonal

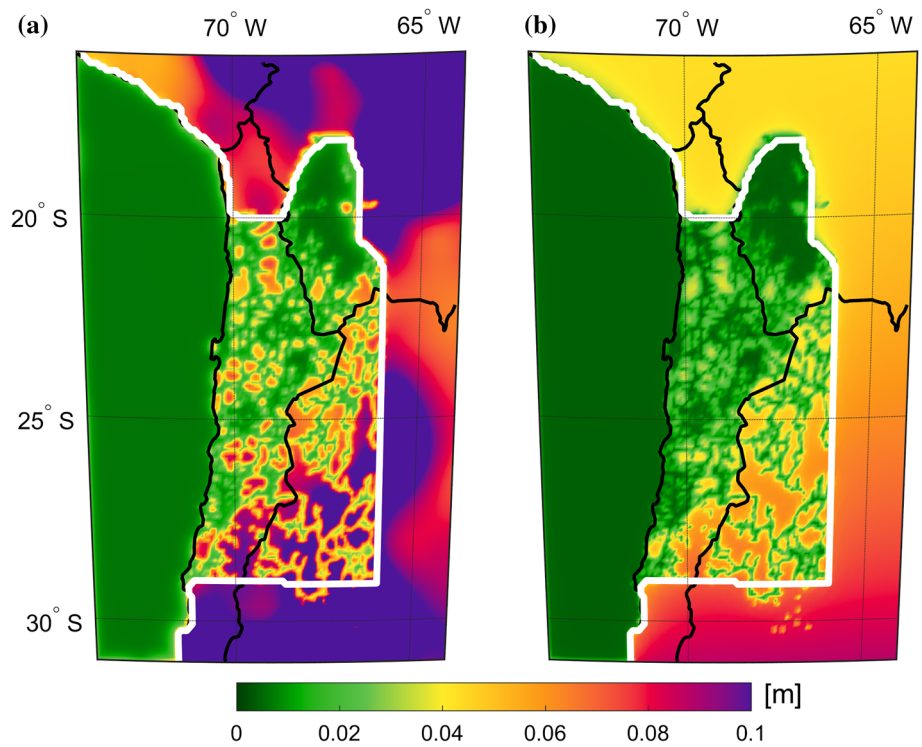
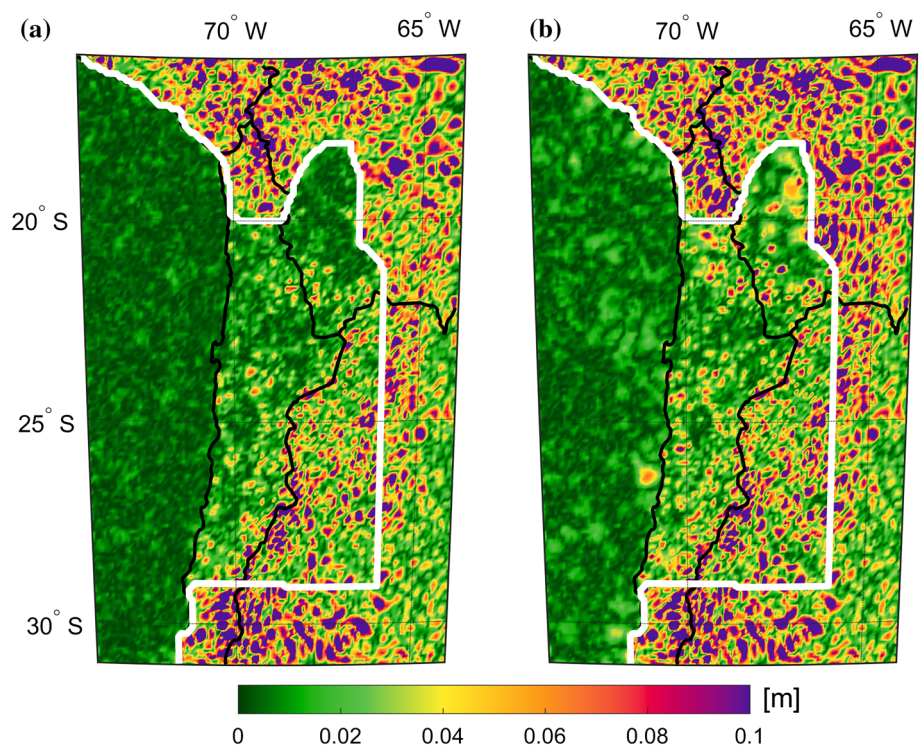


Fig. 8 Case C: Geoid height residuals with the original XGM2016 accuracy. Presented is the absolute difference between the pre-defined truth s and **a** the RLSC result \hat{s} , **b** the standard LSC result \bar{s}



the benefit in case A is negligibly small. With the given point distribution in the target area we see a benefit from including a high-resolution GGM in RLSC which decreases the RMS from 6.0 cm (case A) to 3.9 cm (case B). This benefit is particularly apparent in areas with sparse or medium-dense data distributions and at the edges of the terrestrial observa-

tions. The inclusion of a high-resolution GGM without using RLSC yields with 6.9 cm the worst result among the three cases. Figure 6b demonstrates this even more clearly than the RMS comparison. As expected, the inclusion of a higher quality GGM (case C) gives better results in both of the LSC methods, but still favors RLSC. In contrast to standard LSC,

in all three cases the accuracy of RLSC is well approximated by the formal error estimates. In case B and C the MSD of the formal error differs by only 0.3 cm from the RMS of the residuals (Table 3).

5 Conclusion and outlook

In this paper, we derive and evaluate an approach named residual least-squares collocation that includes several adaptations to previous LSC methods. Principally, we use only residuals as input to RLSC and the stochastic properties of all inputs in the RCR step are separately described by a corresponding covariance matrix. As a result, this adapted formulation only uses error covariance matrices instead of covariance matrices that describe the gravity signal as used in Moritz (1980), Pail et al. (2010), Sansò (2013) or Haagmans and van Gelderen (1991).

We derive the formulation of RLSC from the basics of Moritz (1980) but use the mere stochastic expectation operator E instead of the total average operator \bar{E} for the definition of the covariance matrices. On this basis, for the first time we include a full covariance matrix of a high-resolution GGM in regional geoid modeling. The method also allows us to use covariance matrices that are tailored to a target area. It was already formulated by Tscherning (1999) that the use of isotropic covariance functions does not yield the optimal result in estimating the non-isotropic functionals of the Earth's disturbing gravity field T . Therefore, we derive covariance functions directly from the normal equation system of the high-resolution GGM (here: XGM2016) and use them for the collocation. In general, these location-dependent and non-isotropic covariance matrices fit better to a target area than covariance matrices derived purely from signal degree variances (Moritz 1980; Heiskanen and Moritz 1967) or empirical covariance fitting (Tscherning and Rapp 1974), which both describe only an average part of the Earth (or respectively an average part of a target area). Furthermore, similar to the LSC methods in Pail et al. (2010) or Sansò (2013) RLSC offers the advantage that all stochastic effects are included in a consistent way directly in LSC, which should lead to a realistic accuracy estimation of the output quantities. The downside of the presented approach is that the computation of the covariance matrices for the input and the output points (C_{ii}^m , C_{si}^m and C_{ss}^m) is very CPU-intensive. For the calculation we exploited the LRZ supercomputing system SuperMUC phase 2 where we used 80 Haswell nodes (Xeon E5-2697 v3). These nodes have 28 cores each with a peak performance of 41.6 GFlops/s, which results in a computation time less than an hour. Additionally, it is necessary to have access to the full normal equation system of the GGM which is frequently not available to the public.

For an optimum evaluation of the benefit of the RLSC method we formulate a synthetic test case with a pre-defined truth. To obtain realistic results from it we add noise to the GGM and to the terrestrial gravity observations. However, a number of assumptions must be included in the scenario. In particular, we assume that the variance–covariance information of the XGM2016 model is correct, since we use it to derive the noise of the GGM. Furthermore, we band-limit the gravity signal to degree 2190. In a case where we use real gravity data, we would have to extend the topographic gravity reduction to higher frequencies. Nevertheless, the simulation of three different test cases yields meaningful results and allows us to evaluate RLSC compared to a standard LSC. We see that regional gravity modeling can benefit from the inclusion of a high-resolution GGM with RLSC. In our test case, the numerical advantage of this is an RMS reduction from 6.0 cm (case A) to 3.9 cm (case B) for RLSC where the RMS values are largely affected by the areas with sparse ground data distribution. In areas with a good data coverage RLSC gives residuals mainly below 1 cm in all of the three test cases. In general, by including a high-resolution GGM in RLSC, we obtain better results especially in areas with sparse observations or close to data gaps. In our opinion, this constitutes a big advantage, because terrestrial gravity measurements are often inhomogeneously distributed and data gaps are almost inevitable especially in mountainous regions. Furthermore, it is shown that the stochastic error estimates of the RLSC approach provide realistic uncertainty estimates, which becomes very important when real gravity data is used.

An additional advantage of the inclusion of a high-resolution GGM in LSC and thus working with rather high-frequency residuals is, that it can significantly reduce the amount of terrestrial data that is needed for the calculation. As shown in Sect. 3, the correlation length when using XGM2016 and a topographic gravity model in the remove step is only 0.12° . Therefore, it is possible to reduce the amount of data that is included to RLSC locally and for example use only those observations for the calculation that are within a specified distance from the output. Considering this, we regard the calculation of height reference stations for the International Height Reference System (IHRF; more information in Ihde et al. 2017 or Sánchez and Sideris 2017) as a predestined application for RLSC. The high-resolution GGM could be used as the basis of a worldwide height unification, and terrestrial observations would be used for the local refinement around a height reference station. The unique advantage of RLSC in this context is that terrestrial data coverage would not be needed in an area as large as about 200 km around an IHRF station, which is the current default for a satellite-only GGM. Furthermore, IHRF stations will be distributed globally, so that numerous IHRF stations can either benefit from the in general good quality of high-resolution GGMs over oceans that results from satellite altimetry, or are set to areas

with little terrestrial data coverage where RLSC appears to perform best. Finally, a correct stochastic accuracy estimation is very important for the calculation of potential values at the IHRF stations.

The next step will be to validate the performance of the presented approach within the IAG Joint Working Group (JWG, 2.2.2: the 1 cm geoid experiment) with real measurements. JWG 2.2.2 aims to assess the calculation of gravity potential values at IHRF stations from different calculation methods, and therefore enables another comparison of RLSC to other regional gravity field determination methods. In any case, with continuously improving high-resolution GGMs and especially with the announcement of the Earth Gravitational Model 2020 (EGM2020) by the NGA, we see the impact of high-resolution GGMs for regional geoid modeling even increasing in the future.

Acknowledgements A large part of the investigations presented in this paper was conducted in the framework of the project 'Optimally combined regional geoid models for the realization of height systems in developing countries' funded by the German Research Foundation (DFG Project No. PA 1543/14-1). We also acknowledge the provision of computer resources by the Leibniz Supercomputing Centre (LRZ; Address: Boltzmannstrasse 1, 85748 Garching, Germany).

References

- Andersen O, Knudsen P, Stenseng L (2015) The DTU13 MSS (mean sea surface) and MDT (mean dynamic topography) from 20 years of satellite altimetry. In: Jin S, Barzaghi R (eds) IGFS 2014. International association of geodesy symposia, vol 144. Springer, Cham, pp 111–120. https://doi.org/10.1007/1345_2015_182
- Arabelos DN, Tscherning CC (2009) Error-covariances of the estimates of spherical harmonic coefficients computed by LSC, using second-order radial derivative functionals associated with realistic GOCE orbits. *J Geod* 83(5):419–430. <https://doi.org/10.1007/s00190-008-0250-9>
- Drinkwater MR, Floberghagen R, Haagmans R, Muzi D, Popescu A (2003) GOCE: ESA's first earth explorer core mission. In: Beutler GB et al (eds) Earth gravity field from space—from sensors to earth sciences, space sciences series of ISSI, vol 17, pp 419–432. Springer, Dordrecht. https://doi.org/10.1007/978-94-017-1333-7_36
- Fecher T, Pail R, Gruber T (2015) Global gravity field modeling based on GOCE and complementary gravity data. *Int J Appl Earth Obs Geoinf* 35A:120–127. <https://doi.org/10.1016/j.jag.2013.10.005> (ISSN 0303-2434)
- Fecher T, Pail R, Gruber T, the GOCO Consortium (2017) GOCO05c: a new combined gravity field model based on full normal equations and regionally varying weighting. *Surv Geophys* 38(3):571–590. <https://doi.org/10.1007/s10712-016-9406-y>
- Forsberg R (1984) A study of terrain reductions, density anomalies and geophysical inversion methods in gravity field modelling. Reports of the Department of Geodetic Science and Surveying, No. 355, Ohio State University, Columbus
- Forsberg R, Tscherning CC (1981) The use of height data in gravity field approximation by collocation. *J Geophys Res* 86(B9):7843–7854. <https://doi.org/10.1029/JB086iB09p07843>
- Förste C, Bruinsma SL, Abrikosov O, Lemoine JM, Marty JC, Flechtner F, Balmino G, Barthelmes F, Biancale R (2014): EIGEN-6C4 the latest combined global gravity field model including GOCE data up to degree and order 2190 of GFZ Potsdam and GRGS Toulouse. GFZ Data Services. <https://doi.org/10.5880/icgem.2015.1>
- Gerlach C, Fecher T (2012) Approximations of the GOCE error variance–covariance matrix for least-squares estimation of height datum offsets. *J Geod Sci* 2(4):247–256. <https://doi.org/10.2478/v10156-011-0049-0>
- Grombein T, Seitz K, Heck B (2016) The rock–water–ice topographic gravity field model RWI_TOPO_2015 and its comparison to a conventional rock-equivalent version. *Surv Geophys* 37(5):937–976. <https://doi.org/10.1007/s10712-016-9376-0>
- Gruber T, Willberg M (2019) Signal and error assessment of GOCE-based high resolution gravity field models. In: International symposium gravity, geoid and height systems 2, *J Geod Sci* (accepted)
- Gruber T, Visser P, Ackermann C, Hosse M (2011) Validation of GOCE gravity field models by means of orbit residuals and geoid comparisons. *J Geod* 85(11):845–860. <https://doi.org/10.1007/s00190-011-0486-7>
- Haagmans RHN, van Gelderen M (1991) Error variances–covariances of GEM-TI: their characteristics and implications in geoid computation. *J Geophys Res* 96(B12):20011–20022. <https://doi.org/10.1029/91JB01971>
- Heiskanen WA, Moritz H (1967) Physical geodesy. Freeman and Company, San Francisco
- Hirt C, Claessens SJ, Fecher T, Kuhn M, Pail R, Rexer M (2013) New ultra-high resolution picture of Earth's gravity field. *Geophys Res Lett* 40(16):4279–4283. <https://doi.org/10.1002/grl.50838>
- Hofmann-Wellenhof B, Moritz H (2006) Physical geodesy. Springer, Wien ISBN 10 2-211-33544-7
- Hosse M, Pail R, Horwath M, Holzrichter N, Gutknecht BD (2014) Combined regional gravity model of the andean convergent subduction zone and its application to crustal density modelling in active plate margins. *Surv Geophys* 35(6):1393–1415. <https://doi.org/10.1007/s10712-014-9307-x>
- Ihde J, Sánchez L, Barzaghi R, Drewes H, Förste C, Gruber T, Liebisch G, Marti U, Pail R, Sideris M (2017) Definition and proposed realization of the international height reference system (IHRF). *Surv Geophys* 38(3):549–570. <https://doi.org/10.1007/s10712-017-9409-3>
- Krarpup T (1969) A contribution to the mathematical foundation of physical geodesy. In: Borre K (ed) Mathematical foundation of geodesy—selected papers of Torben Krarpup. Springer, Berlin. <https://doi.org/10.1007/3-540-33767-9>
- Mayer-Gürr T, and the GOCO consortium (2015) The new combined satellite only model GOCO05s. EGU General Assembly, Vienna. <https://doi.org/10.13140/RG.2.1.4688.6807>
- Moritz H (1980) Advanced physical geodesy. Herbert Wichmann, Karlsruhe ISBN 3-87907-106-3
- Pail R, Reguzzoni M, Sansò F, Kühtreiber N (2010) On the combination of global and local data in collocation theory. *Stud Geophys Geod* 54(2):195–218. <https://doi.org/10.1007/s11200-010-0010-1>
- Pail R, Fecher T, Barnes D, Factor JF, Holmes SA, Gruber T, Zingerle P (2018) Short note: the experimental geopotential model XGM2016. *J Geod* 92(4):443–451. <https://doi.org/10.1007/s00190-017-1070-6>
- Pavlis NK, Holmes SA, Kenyon SC, Factor JK (2012) The development and evaluation of the Earth Gravitational Model 2008 (EGM2008). *J Geophys Res* 117:B04406. <https://doi.org/10.1029/2011JB008916>
- Rexer M (2017) Spectral solutions to the topographic potential in the context of high-resolution global gravity field modelling. Dissertation, Technical University of Munich
- Rexer M, Hirt C, Claessens S, Tenzer R (2016) Layer-based modelling of the Earth's gravitational potential up to 10-km scale in spherical harmonics in spherical and ellipsoidal approximation. *Surv Geophys* 37(6):1035–1074. <https://doi.org/10.1007/s10712-016-9382-2>

- Rieser D (2015) GOCE gravity gradients for geoid and Moho determination applying the Least Squares Collocation approach. Dissertation, Graz University of Technology
- Sánchez L, Sideris MG (2017) Vertical datum unification for the international height reference system (IHRs). *Geophys J Int* 209(2):570–586. <https://doi.org/10.1093/gji/ggx025>
- Sandwell DT, Smith WHF (2009) Global marine gravity from retracked Geosat and ERS-1 altimetry: ridge segmentation versus spreading rate. *J Geophys Res* 114:B01411. <https://doi.org/10.1029/2008JB006008>
- Sansò F (1986) Statistical methods in physics geodesy. In: Suenkel H (ed) *Mathematical and numerical techniques in physical geodesy. Lecture notes in earth sciences, vol 7*. Springer, Berlin, pp 49–155. <https://doi.org/10.1007/BFb0010132>
- Sansò F (2013) The local modelling of the gravity field by collocation. In: Sansò F, Sideris MG (eds) *Geoid determination: theory and methods*. Springer, Heidelberg. <https://doi.org/10.1007/978-3-540-74700-0>
- Tapley BD, Bettadpur S, Watkins M, Reigber C (2004) The gravity recovery and climate experiment: mission overview and early results. *Geophys Res Lett* 31(9):L09607. <https://doi.org/10.1029/2004GL019920>
- Tscherning CC (1999) Construction of anisotropic covariance functions using Riesz-representers. *J Geod* 73(6):332–336. <https://doi.org/10.1007/s001900050250>
- Tscherning CC (2015) Least-squares collocation. In: Grafarend E (ed) *Encyclopedia of geodesy*. Springer, Cham. https://doi.org/10.1007/978-3-319-02370-0_51-1
- Tscherning CC, Rapp RH (1974) Closed covariance expressions for gravity anomalies, geoid undulations, and deflections of the vertical implied by anomaly degree variance models. Reports of the Department of Geodetic Science, No. 208, Ohio State University, Columbus

P.4 Publication IV: Integration of airborne gravimetry data filtering into residual least-squares collocation - example from the 1 cm geoid experiment

Reference

Willberg, M., Zingerle, P., Pail, R. Integration of airborne gravimetry data filtering into residual least-squares collocation: example from the 1 cm geoid experiment. *J Geod* 94, 75 (2020). doi 10.1007/s00190-020-01396-2

Copyright

This work originally has been published in *Journal of Geodesy*, available at <https://link.springer.com/> and is an open access publication. The publication will be available under the license of Creative Commons. The Copyrights remain with the authors.

Abstract

Low-pass filters are commonly used for the processing of airborne gravity observations. In this paper for the first time, we include the resulting correlations consistently in the functional and stochastic model of residual least-squares collocation (RLSC). We demonstrate the necessity of removing high-frequency noise from airborne gravity observations, and derive corresponding parameters for a Gaussian low-pass filter. Thereby, we intend an optimal combination of terrestrial and airborne gravity observations in the mountainous area of Colorado. We validate the combination in the frame of our participation in 'the 1 cm geoid experiment'. This regional geoid modeling inter-comparison exercise allows the calculation of a reference solution, which is defined as the mean value of 13 independent height anomaly results in this area. Our result performs among the best and with 7.5 mm shows the lowest standard deviation to the reference. From internal validation we furthermore conclude that the input from airborne and terrestrial gravity observations is consistent in large parts of the target area, but not necessarily in the highly mountainous areas. Therefore, the relative weighting between these two data sets turns out to be a main driver for the final result, and is an important factor in explaining the remaining differences between various height anomaly results in this experiment.

Declaration of own contribution

(MW: Martin Willberg; PZ: Philipp Zingerle; RP: Roland Pail)

MW had the idea to contribute to the 1 cm geoid experiment, prepared the gravity observations and performed initial results, where high-frequency noise was detected in the airborne observations. Accordingly, MW and PZ formulated the methodology section which handles high-frequency noise consistently in the RLSC approach. MW performed most of the calculations and created the results in the paper. The coauthors supported MW in analysis and interpretation, and provided detailed comments and corrections to the manuscript from MW. MW created figures and tables for the paper, whereby PZ had the idea for the figures 2 and 3.

The overall own contribution of MW for *P-IV* is estimated at 87 %, which is the average value of the percentage values estimated for the six criteria listed in the table below (Tab. P.4).

Criteria	Estimated own contribution
Computation and results	90 %
Ideas and study design	75 %
Analysis and interpretation	80 %
Text	90 %
Figures	85 %
Tables	100 %
Total	87 %

Tab. P.4 – Criteria and estimated contribution share of Martin Willberg for *P-IV*

Confirmation by the authors

We hereby confirm the correctness of the declaration of own contribution for the publication

Willberg, M., Zingerle, P., Pail, R. (2020) Integration of airborne gravimetry data filtering into residual least-squares collocation: example from the 1 cm geoid experiment. J Geod 94, 75.
doi: <https://doi.org/10.1007/s00190-020-01396-2>

Philipp Zingerle

Institute for Astronomical and Physical Geodesy, Technical University of Munich, Germany

Signature:  Date: *21.10.2020*

Roland Pail

Institute for Astronomical and Physical Geodesy, Technical University of Munich, Germany

Signature:  Date: *20.10.2020*



Integration of airborne gravimetry data filtering into residual least-squares collocation: example from the 1 cm geoid experiment

Martin Willberg¹ · Philipp Zingerle¹ · Roland Pail¹

Received: 8 November 2019 / Accepted: 1 July 2020
© The Author(s) 2020

Abstract

Low-pass filters are commonly used for the processing of airborne gravity observations. In this paper, for the first time, we include the resulting correlations consistently in the functional and stochastic model of residual least-squares collocation. We demonstrate the necessity of removing high-frequency noise from airborne gravity observations, and derive corresponding parameters for a Gaussian low-pass filter. Thereby, we intend an optimal combination of terrestrial and airborne gravity observations in the mountainous area of Colorado. We validate the combination in the frame of our participation in ‘the 1 cm geoid experiment’. This regional geoid modeling inter-comparison exercise allows the calculation of a reference solution, which is defined as the mean value of 13 independent height anomaly results in this area. Our result performs among the best and with 7.5 mm shows the lowest standard deviation to the reference. From internal validation we furthermore conclude that the input from airborne and terrestrial gravity observations is consistent in large parts of the target area, but not necessarily in the highly mountainous areas. Therefore, the relative weighting between these two data sets turns out to be a main driver for the final result, and is an important factor in explaining the remaining differences between various height anomaly results in this experiment.

Keywords Residual least-squares collocation · Regional geoid modeling · 1 cm geoid experiment · GRAV-D · Low-pass filter · Airborne gravimetry

1 Introduction

In this paper we adapt the residual least-squares collocation (RLSC, Willberg et al. 2019) so that correlations from low-pass-filtered airborne gravity observations are handled consistently. Simultaneously, we present our final result from an International Association of Geodesy (IAG) joint working group (JWG) which is designed to support the realization of the International Height Reference System (IHRs, Ihde et al. 2017). Within this JWG 2.2.2, called ‘the 1 cm geoid experiment’, different participating groups calculate height anomaly, geoid height and potential values by using identical terrestrial and airborne gravity observations. The main objective of this JWG is to increase the compatibility between different methods for regional geoid determination

by analyzing and quantifying differences between the results. Furthermore, the experiment should help to define common standards for the IHRs realization and verify the quality of the submitted results. Additional information about the purpose and benefit of the JWG is published in a summary paper (Wang et al. (2020), this issue).

The study area of ‘the 1 cm geoid experiment’ lies at the southern end of the Rocky Mountains in the United States of America; mainly in the states of Colorado and New Mexico. It was selected for its geoid slope validation survey from 2017 (GSVS17) where positions, gravity and deflections of the vertical are measured with very high accuracy at a line of 223 benchmarks along U.S. Highway 160. However, these measurements or their processing are not yet published, so they will function as reference values for the JWG results only in the future. Furthermore, the region has good coverage in terms of terrestrial and airborne gravity measurements, but is also intended to be a very challenging region for regional geoid determination, as it includes highly mountainous areas. Another major challenge within the JWG, and one main topic of this paper, is the optimal inclusion of airborne grav-

Martin Willberg
martin.willberg@tum.de

¹ Institute of Astronomical and Physical Geodesy, Technical University of Munich, Arcisstrasse 21, 80333 Munich, Germany

ity observations from the ‘Gravity for the Redefinition of the American Vertical Datum’ project (GRAV-D, GRAV-D Team 2018b). Within this project, the complete area of the United States is covered with equally distributed airborne observations in order to define a new gravity-based vertical datum, preferably with an accuracy of 1–2 cm (GRAV-D Team 2017).

For our calculation we include RLSC (Willberg et al. 2019) as a modified version of the standard least-squares collocation (LSC) by Moritz (1980). By including a remove–compute–restore (RCR) approach with a high-resolution global geopotential model (GGM) and a topographic gravity model, the input of RLSC consists only of residuals. As GGM, we include the XGM2018 model, an internal successor of XGM2016 (Pail et al. 2018). Both models provide a full variance–covariance information from regional varying weighting, which enables improved error-modeling in RLSC. However, XGM2018 provides a more realistic stochastic model for the GGM reduction (see discussion on this issue in Willberg et al. 2019). Additionally, accuracy estimation in RLSC benefits from the fact that individual covariance matrices contain stochastic information of all involved components. Detailed justification for the application of RLSC and a comparison between RLSC and standard LSC is published in Willberg et al. (2019). This contribution adapts RLSC to airborne gravimetry for the first time.

A crucial task thereby is to separate the target gravity signal from the observation noise which is normally implemented by a low-pass filter (e.g., Childers et al. 1999). While the variety of different filters for this purpose is huge, their purpose is very similar: to reduce the high-frequency noise from the airborne observations (details in Sect. 2). The application of a low-pass filter is necessary for platform-stabilized gravimeters (Childers et al. 1999; Olesen 2003) as well as strapdown gravimeters (Wei and Schwarz 1998; Becker 2016; Li 2011). Detailed descriptions of the two different measurement systems and the predominant error sources are given in Schwarz and Wei (1995). In general, both gravimeter types are used within the GRAV-D project, but in the target area (5th block mountain south, MS05), we only have airborne measurements from the platform-stabilized gravimeters Micro-g LaCoste TAGS S-137 (turn-key airborne gravimetry system) and TAGS S-211. Detailed documentation about the instrumentation and the flight lines from block MS05 is provided in GRAV-D Team (2018a).

The inclusion of a low-pass filter for the processing of airborne gravity data is the standard procedure. However, a low-pass filter will inevitably result in a significant correlation of the airborne observations along the track of the aircraft, which is usually not considered in airborne processing. As an example, Forsberg et al. (2000, 2014) and Hwang et al. (2007) assume low-pass filtered airborne observations

to be uncorrelated in LSC. Within this paper, for the first time, we derive an approach which includes correlations resulting from a low-pass filter consistently in the functional and stochastic model of RLSC. As a result of the modification, we have a more consistent error modeling and filter dependent covariance matrices. Taking these correlations into account seems of even higher significance when the airborne observations are combined with other measurements (e.g., terrestrial gravity observations).

We see another advantage of our presented approach in the fact that the combination of terrestrial and airborne gravity measurements is included in a direct, one-step LSC, which also contains field transformation and the downward continuation of airborne measurements. For the combination of different data sets, the one-step calculation allows the full exploitation of the much higher airborne resolution in along-track direction. For other approaches, which either calculate a regular grid before the downward continuation (Forsberg et al. 2000) or include a spectral method for the analysis of airborne measurements at flight height (Smith et al. 2013; Jiang and Wang 2016), the difference between along-track and across-track accuracy gets lost.

In summary, the main innovations of this paper include (1) a novel approach to include a low-pass filter to regional gravity field modeling in general, and RLSC in particular; (2) application of GRAV-D data with recommendations for its use; (3) the first application of RLSC to real gravity observations, as the theory paper on RLSC (Willberg et al. 2019) uses a synthetic simulation environment; (4) demonstration of the RLSC contribution to ‘the 1 cm geoid experiment’ and comparison of corresponding results.

This paper is structured as follows. In Sect. 2 we motivate the application of a low-pass filter for airborne observations. Next, in Sect. 3 a suitable filter is derived and included into the RLSC formalism, resulting in a rigorous formulation for the combination of filtered (airborne) and unfiltered (terrestrial) observations. The data sets and our calculation procedure from ‘the 1 cm geoid experiment’ are explained in Sect. 4, and its results are analyzed in Sect. 5. Additionally, we include comparisons of our results along GSVS17 in relation to the JWG mean value (Sect. 6). Lastly, we draw conclusions and give an outlook in Sect. 7.

2 Reasons for low-pass filter in airborne gravimetry

For optimal comparisons within ‘the 1 cm geoid experiment’ the input observations used by all contributing groups should be identical. Therefore, the airborne observations of block MS05 are provided as gravity measurements within the JWG. In contrast to the original GRAV-D airborne data available at the homepage of the National Geodetic Survey (2019, NGS),

the provided data is already corrected for the individual line bias by comparison with already existing models and cross-point validation. Furthermore, the data is provided with the uniform frequency of 1 Hz while the gravimeter Micro-g LaCoste TAGS S-211 originally records data at 20 Hz (GRAV-D Team 2018a).

As is well known, airborne gravity observations include in general higher noise levels than stationary terrestrial data. This results from the dynamics of the aircraft. Corrections have to be applied for Eötvös accelerations (Harlan 1968), the vertical acceleration (Zhong et al. 2015), and the off-level error of the instrument (LaCoste 1967; Swain 1996). The exact corrections that are applied to the observations are described in GRAV-D Team (2017), and a description of the underlying software with the use of the same notation can be found in Zhong et al. (2015). It is commonly assumed that the occurring noise shows up mainly in the short wavelengths, while the gravity signal dominates the longer wavelengths (e.g., Childers et al. 1999). Accordingly, the inclusion of a low-pass filter in along-track direction of airborne gravimetry is common practice.

Airborne observations from the GRAV-D project are already low-pass filtered with a time domain Gaussian filter (GRAV-D Team 2017, Chapter 2.2). However, its purpose was to preserve the amplitude of the gravity signal, and it leaves significant short-wavelength noise in the data (GRAV-D Team 2018a). Accordingly, the GRAV-D Team (2018a, Chapter 4.1) recommends using a second low-pass filter for the airborne observations in order to remove the short-wavelength noise. In this study, we assume that the first filter actually leaves the gravity signal untouched (as it was intended), because it allows us to neglect the first filter in the theoretical derivations (Sect. 3). As a consequence, in the following we call the GRAV-D observations provided within ‘the 1 cm geoid experiment’ as ‘original airborne observations’, although they already include the first low-pass filter, the line bias correction and the resampling to uniform 1 Hz frequency. Accordingly, in further usage of the expression “filter”, we are referring only to the second one. The GRAV-D Team (2018a, Chapter 4.1) also emphasizes that the low-pass filter should be included prior to a downward continuation, as it would otherwise amplify the noise. Since LSC implicitly includes a downward continuation, we apply a suitable low-pass filter before the LSC method (details in Sect. 3).

In general, we consider the characterization of the high-frequency noise as a sophisticated problem, because its amplitude and frequency distribution can change due to various reasons like wind conditions or flight velocity. An analysis of the most dominant error sources in airborne gravimetry and its assessment can be found in Schwarz and Wei (1995). However, we need to specify filter criteria in order to separate the noise and gravity signal. We demonstrate this in the following example: some of the flight lines

in MS05 are actually divided into two segments (GRAV-D Team 2018a). Accordingly, there is a total of seven flight segments, where the end of one flight line overlaps with the beginning of another. One of these flight segments has overlapping measurements over approximately 100 km which is significantly more than all other combinations. In Fig. 1, we present the overlapping segments of these two flight lines (FL) 103 (red) and 203 (blue) with its original gravity disturbances (bright solid lines) and the filtered observations (dark solid lines), respectively. Additionally, the dotted lines result from an approximation by available spherical harmonic (SH) coefficient models (details in Sect. 4). Therefore, in our case we include a combination of XGM2018 and the topographic gravity model $dV_ELL_Earth2014$, which is calculated according to Rexer et al. (2016), but continued to SH degree 5480 by including 1 arc-min topography information from Hirt and Rexer (2015). Note that the presented flight lines result from the same flight plan, which is why their horizontal offset is negligible. Their gravitational difference from the vertical offset is small and can be approximated by the difference between the two modeled observations (dotted lines).

In this section of the flight lines we see major anomalies due to the fast-changing topography, and the gravity disturbances change with about 100 mGal over a distance of only 50 km. The two close-up analyses in Fig. 1 display that there is basically no correlation between the high-frequency signals of FL103 and FL203, which indicates dominating noise in these frequencies. The modeled airborne observations contain gravity signals to SH degree 5480. Nevertheless, they appear very smooth in comparison to the original gravity observations, which is assumed to result from high-frequency noise in the observations as well. By including a Gaussian low-pass filter we reduce high frequencies in the observations, so that the modeled observations and the filtered observations approximately contain the same spectral signal content (Fig. 1). Details about the Gaussian filter are explained at a later stage in Sects. 3.1 and 3.3. Apart from the reduction of high-frequency noise and the recommendations by the GRAV-D team, we consider a low-pass filter necessary for the following reasons:

- (1) The original airborne observations are available with a frequency of 1 Hz, all in all resulting in 283,716 observations. Because there is a very high correlation between consecutive observations, we do not consider it reasonable to include all observations directly in the processing. However, decreasing the amount of observations is only possible if a low-pass filter is applied first, and otherwise we will create aliasing errors (details in Sect. 3.3).
- (2) Furthermore, decreasing the amount of airborne observations is necessary in order to prevent RLSC from containing numerically singular covariance matrices.

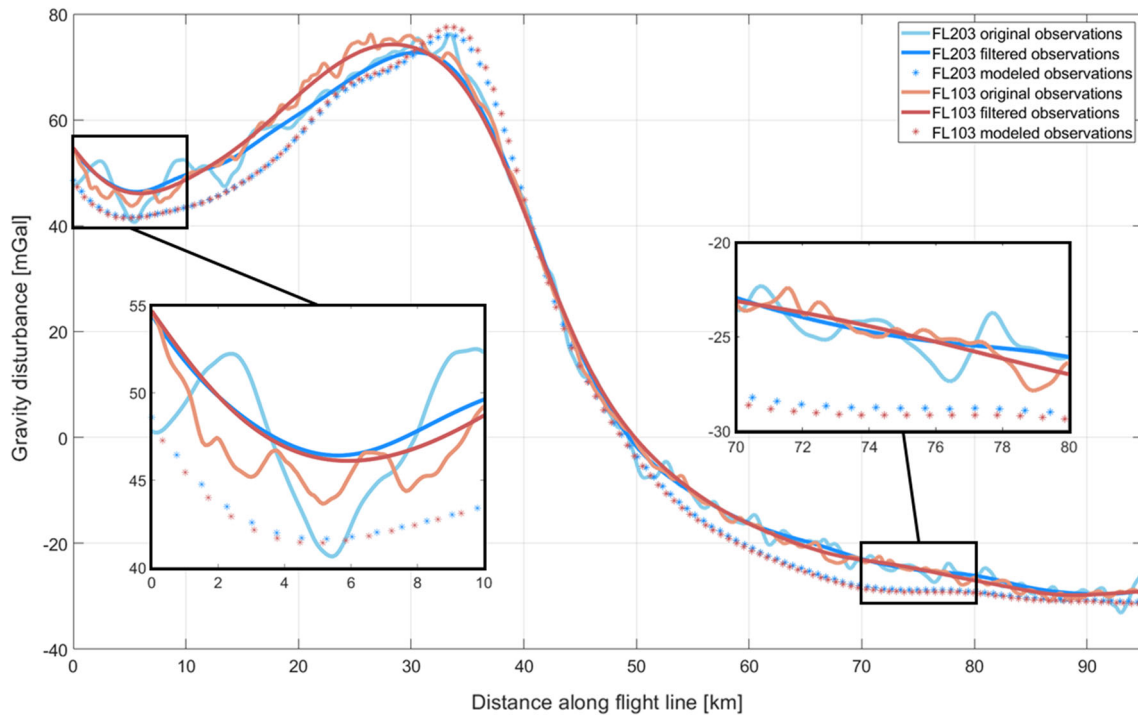


Fig. 1 Overlapping flight segments between the flight lines 103 (red) and 203 (blue). The gravity disturbances for the original observations, the filtered observations and the modeled observations are presented. Two parts of 10 km each are enlarged for more details

These would inevitably arise when airborne observations are included with a 1 Hz sampling frequency.

- (3) In the current implementation our RLSC approach for airborne observations is limited to the maximum SH degree 5480, as this is the highest available resolution for a topographic gravitational potential model (in our case: $dV_ELL_Earth2014$). Consequently, airborne gravity signals above this SH degree would result in a model error. It is commonly assumed that airborne observations do not include a significant gravity signal above SH degree 5480 (approx. 4 km in spatial resolution) due to signal attenuation with altitude. However, we have to consider the following: a few of the flight lines are located at 5200 m above the ellipsoid while the Rocky Mountains beneath the corresponding lines reach heights of more than 4000 m. Accordingly, the flight tracks can be quite close to the signal generating masses. At the same time, there might be significant errors in the topographic gravity model due to problems of Shuttle Radar Topography Mission (SRTM) in areas with fast-changing topography. Lastly, the limited spatial resolution of topographic elevation models in highly mountainous areas is another reason that might result in errors. Only by including a low-pass filter can we guarantee that these problems do not arise in (R)LSC.

3 Methodology

In this section, we show the attenuation of different low-pass filters in the frequency domain by using the recursion formulas by Jekeli (1981). Next, we derive a Gaussian low-pass filter that is suitable for airborne gravity data, include it consistently in the functional and stochastic model of RLSC, and explain its effect. Thereby, we also present a numerical example for the final covariance matrix. Lastly, we formulate the combination of filtered airborne and unfiltered terrestrial gravity observations.

3.1 A Gaussian low-pass filter

A normalized Gaussian weighting function w_G can be written as a function of the Euclidean distance d

$$w_G(d) = \alpha \exp\left(-\frac{d^2}{2\sigma^2}\right), \quad (1)$$

whereby the standard deviation of the Gaussian filter σ defines the smoothing effect. The weighting function $w_G(d)$ includes the normalization factor α so that the overall signal content is not amplified or weakened by the filter. This normalization factor α will be derived later on (cf. Eq. 9). Jekeli (1981) derives the weighting function w_G of a Gaussian filter

on the sphere in dependence of its spherical distance ψ

$$w_G(\psi) = \alpha \exp(-b(1 - \cos \psi)), \tag{2}$$

where b gives the smoothing effect which is defined by the radius of the Earth R

$$b = \frac{R^2}{\sigma^2}. \tag{3}$$

Note that Eqs. 1 and 2 can be derived from each other using simple trigonometry. Furthermore, Jekeli (1981) gives recursion formulas which are normalized on the unit sphere. They enable the formulation of the attenuation β , which results from a Gaussian filter per SH degree n in the frequency domain

$$\begin{aligned} \beta_0 &= 1, \\ \beta_1 &= \frac{1 + \exp(-2b)}{1 - \exp(-2b)} - \frac{1}{b}, \\ \beta_{n+1} &= -\frac{2n + 1}{b} \beta_n + \beta_{n-1}. \end{aligned} \tag{4}$$

We see that with decreasing β , the attenuation of the Gaussian filter increases when either the SH degree or the standard deviation σ becomes larger. Strictly speaking, the recursion formulas are only valid for points on the sphere, which is why Jekeli (1981) includes a spherical approximation for points on the ellipsoid. By analogy, we include the same approximation since we apply the filter to airborne observations with a relatively constant flight height above the ellipsoid. In the following, the standard deviation σ is replaced by the more intuitive half width at half maximum (HWHM)

$$\sigma = \frac{\text{HWHM}}{\sqrt{2 \ln(2)}}. \tag{5}$$

The HWHM of a Gaussian low-pass filter describes the distance after which the weighting function w_G decreases to half its maximum. Figure 2 presents the attenuation β per SH degree n (Eq. 4) that is evoked by different Gaussian filters with a HWHM between 1 and 5 km. While the HWHM of 5 km (green) basically erases all signals at SH degree 5000, the HWHM of 1 km (blue) attenuates only 20% of the signal at this SH degree.

3.2 Including the Gaussian filter into the functional model

The Gaussian weighting function defined in Eq. 1 can be formulated to describe the filter process in form of a functional model \mathbf{A}^G . It calculates filtered observations \mathbf{I}^G from

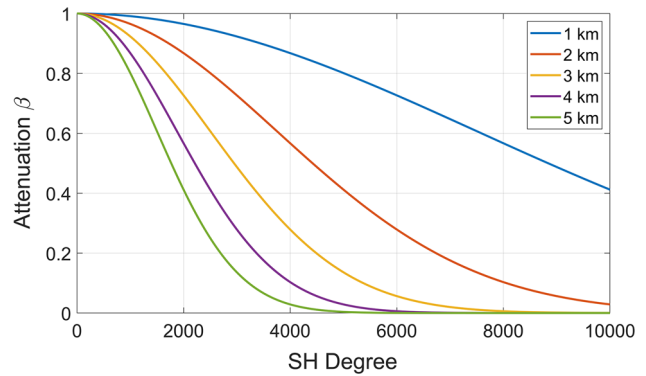


Fig. 2 Relationship between the SH degree n and the attenuation β of the Gaussian filter according to the recursion formulas by Jekeli (1981) in Eq. 4. Five different filters with the HWHM between 1 and 5 km are presented

the original airborne observations \mathbf{I}

$$\mathbf{I}^G = \mathbf{A}^G \mathbf{I}. \tag{6}$$

Note that number and position of the original observations \mathbf{I} and the filtered observations \mathbf{I}^G do not have to be identical. If there are, for example, less point positions in \mathbf{I}^G than there are in \mathbf{I} , the functional model \mathbf{A}^G will result in a reduction of the sampling frequency. This process is called downsampling in the following. In order to keep the signal content consistent before and after the filter process, \mathbf{A}^G is normalized so that the summation of one row in \mathbf{A}^G equals one

$$\sum_{j=1}^N a_{ij} = 1. \tag{7}$$

Therein, a_{ij} are the matrix elements of the functional model \mathbf{A}^G and N is the number of observations \mathbf{I} in one flight line. Consistently, \hat{a}_{ij} are the elements of the functional model before the normalization

$$\hat{a}_{ij} = \hat{w}_G(d_{ij}) = \exp\left(-\frac{d_{ij}^2}{2\sigma^2}\right), \tag{8}$$

with $\hat{w}_G(d_{ij})$ being the related Gaussian weighting function for the distance d_{ij} . The normalized Gaussian weighting function can be formulated by adding the normalization factor α_i

$$\alpha_i = \left(\sum_{k=1}^N \hat{a}_{ik}\right)^{-1}, \tag{9}$$

to Eq. 1

$$\mathbf{A}^G = \{w_G(d_{ij})\} = \left\{ \alpha_i \exp\left(-\frac{d_{ij}^2}{2\sigma^2}\right) \right\}. \tag{10}$$

We see that the elements of \mathbf{A}^G after the normalization are defined by the Gaussian weighting function $w_G(d_{ij})$. Note that the high-frequency noise of airborne observations occurs only in along-track direction, so that we use a 1-D Gaussian filter along individual flight lines. Accordingly, our approach differs from the 2-D filters in Jekeli (1981) or Huang et al. (2008), who apply and normalize their filters on the unit sphere or surface element, respectively. In the functional model \mathbf{A}^G , every row refers to a filtered observation whereas the columns refer to the original observations. Accordingly, one row in \mathbf{A}^G defines which original observations are used to calculate the corresponding filtered value. One column in \mathbf{A}^G describes to what extent a specific original observation will be included in different filtered values (Eq. 6). Visualizing the values of either one row or one column would look like a bell-shaped curve since the functional model \mathbf{A}^G is calculated from a (Gaussian) low-pass filter. Its shape is thereby defined by the combination of the filter radius in the Gaussian weighting function and the flight velocity at recording time. Note that in general the functional model is not symmetric since it is normalized only in one dimension.

3.3 Spectral limitation of airborne gravity data

In Sect. 2 we found that the very high frequencies in the airborne observations should be removed before the downward continuation. Furthermore, the total number of observations has to be reduced before LSC. We regard the functional model of a Gaussian filter \mathbf{A}^G , as a suitable tool to put these two aspects into practice.

The airborne gravity measurements are discrete observations of the continuous gravity field. According to the Nyquist–Shannon sampling theorem, a continuous signal with the maximum frequency f^{\max} can only be reconstructed from an equidistant sampling with a frequency higher than $2 f^{\max}$. Accordingly, simply reducing the sampling frequency of very high-frequency observations generally results in aliasing effects. In practice, a common approach to treat this issue is the use of a low-pass filter (Childers et al. 1999). It reduces the maximum frequency f^{\max} and therefore also the new sampling frequency that is needed to fulfill the Nyquist–Shannon sampling theorem. In the case that the equidistant sampling after the filter process is done with the frequency $2 f^s$, all frequencies below f^s could be restored while the frequencies above f^s are irretrievably lost.

We want to exploit these aspects in order to separate signal and noise in the airborne observations. For this purpose, we assume that the airborne observations mainly include noise above a specific SH degree μ and follow our three-step procedure in order to remove this noise by means of the Gaussian functional model \mathbf{A}^G . Additionally, Fig. 3 visualizes the three steps with their relationship in terms of SH degree and attenuation factor β (introduced in Eq. 4 and Fig. 2).

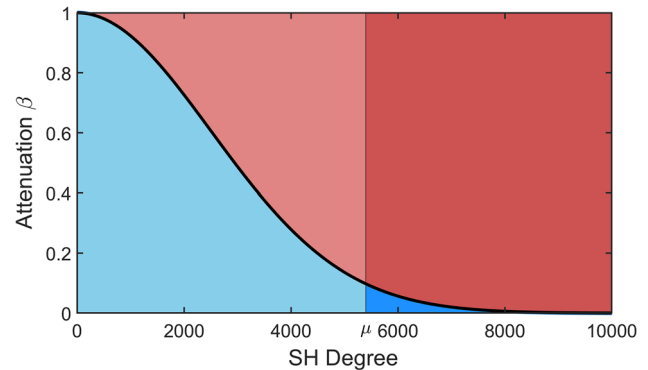


Fig. 3 Relationship between the SH degree and the attenuation β of the Gaussian filter with μ set to SH degree 5400. The red ‘areas’ are removed by the Gaussian filter. The two dark areas are assumed to mainly consist of noise, while the two brighter colored areas are dominated by signal

- (1) A Gaussian low-pass filter removes the two red parts in the frequency domain (Fig. 3). Thereby, it filters most of the noise, but also parts of the signal from the observations. The Gaussian filter radius is selected as a compromise between the preservation of the signal and the removal of the noise. In Fig. 3 we set it exemplary to $\text{HWHM} = 3$ km, as this keeps only 10% of the noise at SH degree μ .
- (2) Reducing the sampling frequency of the observations to SH degree μ irretrievably removes the previously filtered data above this SH degree (Fig. 3: dark red area). By doing this, the dark blue area is discarded as well, however it is still present in the filtered observations, thus causing a small aliasing effect. For the implementation we combine step 1 and 2, so that the functional model \mathbf{A}^G includes the low-pass filter and the downsampling process (refer to Sect. 3.2).
- (3) Lastly, the previously filtered signal representing SH degrees below μ (Fig. 3: light red area) can be restored from the filtered observations \mathbf{I}^G by means of a high-pass filter. This step works analogous to a deconvolution by multiplication with the inverse Gaussian functional model \mathbf{A}^S . It results in observations \mathbf{I}^S which are spectrally limited to SH degree μ

$$\mathbf{I}^S = (\mathbf{A}^S)^{-1} \mathbf{I}^G. \quad (11)$$

Here, the Gaussian functional model \mathbf{A}^S is a square matrix that describes the point positions of \mathbf{I}^G in both dimensions and is normalized according to Eq. 10. Note that the Gaussian functional models \mathbf{A}^G and \mathbf{A}^S are derived in the same way. They differ only in the corresponding point positions, and the normalization factor, as it is related to the input positions.

Applying these steps removes high-frequency noise and results in spectrally limited observations \mathbf{I}^S which could be inserted into LSC. In this case, the spectral limitation from step one to three could be interpreted as an airborne preprocessing. However, in the next section we include these three steps consistently within RLSC instead, thereby considering the correlations from the Gaussian filter between consecutive observations as well. Linking the described steps to the RLSC procedure, we insert the filtered observations \mathbf{I}^G (step 2) as input and apply a high-pass filter (step 3) implicitly within RLSC.

3.4 Adapting RLSC to include the Gaussian filter model

The RLSC formula for calculating an output \mathbf{s} from the input observations \mathbf{I} is given by Willberg et al. (2019)

$$\mathbf{s} = \mathbf{C}_{\hat{\mathbf{s}}\hat{\mathbf{I}}} (\mathbf{C}_{\mathbf{I}\mathbf{I}} + \mathbf{C}_{\hat{\mathbf{I}}\hat{\mathbf{I}}})^{-1} (\mathbf{I} - \hat{\mathbf{I}}) + \hat{\mathbf{s}}, \tag{12}$$

where $\mathbf{C}_{\mathbf{I}\mathbf{I}}$ is the covariance matrix of the observations, $\mathbf{C}_{\hat{\mathbf{I}}\hat{\mathbf{I}}}$ the covariance matrix of an unbiased reduction model $\hat{\mathbf{I}}$, and $\mathbf{C}_{\hat{\mathbf{s}}\hat{\mathbf{I}}}$ the cross-covariance matrix between input and output. In general, the hat-operator marks quantities which have been derived from external reference models (GGM, topographic gravity model). The positions and functionals of covariance matrices are defined by its subscript. In Eq. 12 a remove–compute–restore (RCR) approach analogous to Willberg et al. (2019) is already included,

$$\begin{aligned} \Delta\mathbf{I} &= \mathbf{I} - \hat{\mathbf{I}}, \\ \mathbf{s} &= \Delta\mathbf{s} + \hat{\mathbf{s}}, \end{aligned} \tag{13}$$

so that we reduce the observations \mathbf{I} with unbiased model observations $\hat{\mathbf{I}}$ before RLSC. The reduction model in the output functional $\hat{\mathbf{s}}$ is restored accordingly after RLSC. Note that the covariance function of the reduction model $\mathbf{C}_{\hat{\mathbf{I}}\hat{\mathbf{I}}}$ is contained consistently in Eq. 12. Following Eq. 6 we apply the Gaussian functional model \mathbf{A}^G to $\Delta\mathbf{I}$ and, due to linearity of this operator, correspondingly to both \mathbf{I} and $\hat{\mathbf{I}}$

$$\begin{aligned} \mathbf{A}^G \Delta\mathbf{I} &= \mathbf{A}^G \mathbf{I} - \mathbf{A}^G \hat{\mathbf{I}} \\ &= \mathbf{I}^G - \hat{\mathbf{I}}^G. \end{aligned} \tag{14}$$

The corresponding covariance functions of \mathbf{I}^G and $\hat{\mathbf{I}}^G$ are calculated from simple error propagation. From Eq. 6, we obtain the covariance matrix of filtered observations $\mathbf{C}_{\mathbf{I}\mathbf{I}}^G$

$$\mathbf{C}_{\mathbf{I}\mathbf{I}}^G = \mathbf{A}^G \mathbf{C}_{\mathbf{I}\mathbf{I}} (\mathbf{A}^G)^T, \tag{15}$$

and accordingly the covariance function of the model observations $\mathbf{C}_{\hat{\mathbf{I}}\hat{\mathbf{I}}}^G$

$$\mathbf{C}_{\hat{\mathbf{I}}\hat{\mathbf{I}}}^G = \mathbf{A}^G \mathbf{C}_{\hat{\mathbf{I}}\hat{\mathbf{I}}} (\mathbf{A}^G)^T. \tag{16}$$

Similarly, we obtain for the cross-covariance matrix $\mathbf{C}_{\hat{\mathbf{s}}\hat{\mathbf{I}}}^G$

$$\mathbf{C}_{\hat{\mathbf{s}}\hat{\mathbf{I}}}^G = \mathbf{C}_{\hat{\mathbf{s}}\hat{\mathbf{I}}} (\mathbf{A}^G)^T, \tag{17}$$

considering that the output model $\hat{\mathbf{s}}$ is not filtered, thus multiplying \mathbf{A}^G only once. From Eqs. 14 to 17, we conclude that the RLSC method with filtered observations

$$\mathbf{s} = \mathbf{C}_{\hat{\mathbf{s}}\hat{\mathbf{I}}}^G (\mathbf{C}_{\mathbf{I}\mathbf{I}}^G + \mathbf{C}_{\hat{\mathbf{I}}\hat{\mathbf{I}}}^G)^{-1} (\mathbf{I}^G - \hat{\mathbf{I}}^G) + \hat{\mathbf{s}}, \tag{18}$$

is identical to the standard formula for RLSC (Eq. 12) except that the covariance matrices \mathbf{C}^G , the observations \mathbf{I}^G and the model observations $\hat{\mathbf{I}}^G$ refer to filtered values instead of the original ones. Note that the output \mathbf{s} should contain an unfiltered signal, therefore we do not use superscripts for \mathbf{s} and $\hat{\mathbf{s}}$. In the case that airborne gravity observations are included in Eq. 18, their spectral limitation (Sect. 3.3, step 1 and 2) is already included in the filtered values \mathbf{I}^G and $\hat{\mathbf{I}}^G$. The deconvolution (step 3) happens within the multiplication of the inverted covariance matrices $\mathbf{C}_{\mathbf{I}\mathbf{I}}^G$ and $\mathbf{C}_{\hat{\mathbf{I}}\hat{\mathbf{I}}}^G$.

3.5 A noise covariance function for the observations

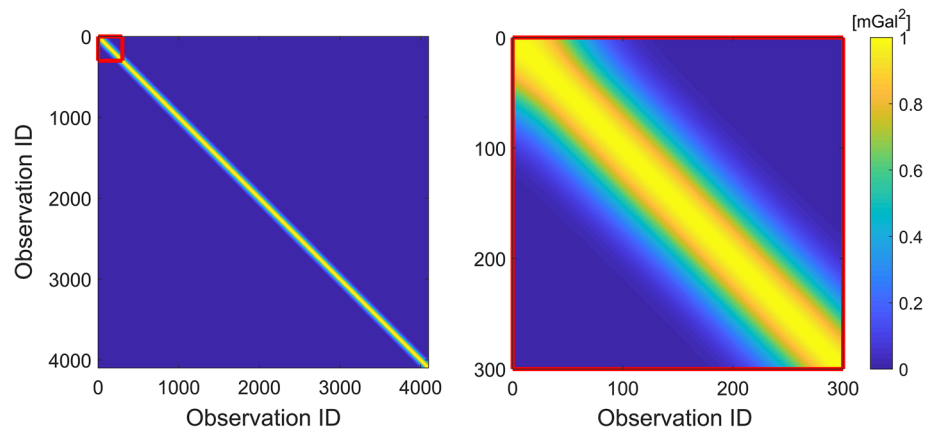
In LSC, the covariance function of the observation noise is often included as a diagonal matrix (Moritz 1980; Arabelos and Tscherning 2009) under the assumption that different observations are not correlated among each other. Obviously, this assumption does not hold for low-pass-filtered observations as they contain a strong correlation among consecutive measurement epochs. In this section, we derive a covariance function for the filtered observations $\mathbf{C}_{\mathbf{I}\mathbf{I}}^G$ in Eq. 15.

The covariance information of the unfiltered observations $\mathbf{C}_{\mathbf{I}\mathbf{I}}$ is in general unknown, which is one of the main reasons for applying the Gaussian low-pass filter in the first place. Thus, instead of propagating $\mathbf{C}_{\mathbf{I}\mathbf{I}}$ to $\mathbf{C}_{\mathbf{I}\mathbf{I}}^G$ we can define the variances $\sigma_{\mathbf{I}^G} \circ \sigma_{\hat{\mathbf{I}}^G}$ (from elementwise multiplication \circ) on the main diagonal of $\mathbf{C}_{\mathbf{I}\mathbf{I}}^G$. Thereby, we assume to know the accuracy of the observations after the filter process. In this case $\mathbf{C}_{\mathbf{I}\mathbf{I}}$ is introduced as identity matrix \mathbf{I} , and the row vector \mathbf{m} is included as factor to set the variances of $\mathbf{C}_{\mathbf{I}\mathbf{I}}^G$ to $\sigma_{\mathbf{I}^G} \circ \sigma_{\hat{\mathbf{I}}^G}$. We can write

$$\mathbf{C}_{\mathbf{I}\mathbf{I}}^G = (\mathbf{A}^G \mathbf{I} (\mathbf{A}^G)^T) \circ (\mathbf{m} \mathbf{m}^T), \tag{19}$$

$$\mathbf{m} = \sqrt{\frac{\sigma_{\mathbf{I}^G} \circ \sigma_{\hat{\mathbf{I}}^G}}{\text{diag}(\mathbf{A}^G (\mathbf{A}^G)^T)}}, \tag{20}$$

Fig. 4 Visualization of the covariance function \mathbf{C}_{\parallel}^G from FL103 whereby **a** presents the covariance function for all 4099 observations, while **b** is a zoom to the first 300 observations



whereby Eq. 20 uses elementwise division and $\text{diag}(\mathbf{X})$ defines the main diagonal of a square matrix \mathbf{X} . By including the identity matrix in Eq. 19 we assume an uncorrelated error for the airborne observations \mathbf{I} before the Gaussian filter process which, in general, is not the case. However, the simplification is justified in our case as the correlation of this error is assumed to be small in comparison to the correlation resulting from the Gaussian filter.

Exemplary, Fig. 4a shows the covariance function \mathbf{C}_{\parallel}^G (Eq. 19) of a single flight line (FL103) without downsampling. The main diagonal of \mathbf{C}_{\parallel}^G is defined by the variances $\sigma_{\mathbf{I}}^G \circ \sigma_{\mathbf{I}}^G$ of the filtered observations, which are equally set to 1 mGal^2 . The same information with more detail is presented in Fig. 4b which zooms to the first 300 observations. We can see a band matrix with very strong correlations among consecutive observations instead of the usual diagonal matrix (e.g., Forsberg et al. 2000, 2014; Hwang et al. 2007). Thus, Fig. 4b verifies that the reduction of the sampling frequency is reasonable in this case due to the very strong correlations among consecutive observations. Furthermore, this is necessary as in general the covariance matrix \mathbf{C}_{\parallel}^G without downsampling tends to be numerically singular for the same reason. The downsampling procedure we introduced in Sect. 3.2 would generally retain the structure of a band matrix in \mathbf{C}_{\parallel}^G , but the covariance would drop to zero much faster.

3.6 Combining filtered and unfiltered observations

In the Colorado experiment, we have a combination of terrestrial and airborne gravity observations, and all reasons we listed for applying a low-pass filter to the airborne observations (Sect. 2) are not valid for the terrestrial ones. Therefore, we present a formulation that applies the standard RLSC from Eq. 12 to the terrestrial observations, while the airborne observations are processed according to Eq. 18 with a Gaussian filter. In order to realize a consistent formulation, we keep naming the original observations \mathbf{I} , but now con-

sider them as a combination of terrestrial \mathbf{I}_{ter} and airborne \mathbf{I}_{air} observations

$$\mathbf{I} = \begin{bmatrix} \mathbf{I}_{\text{ter}} \\ \mathbf{I}_{\text{air}} \end{bmatrix}. \quad (21)$$

Similarly, we handle the reduction model $\hat{\mathbf{I}}$

$$\hat{\mathbf{I}} = \begin{bmatrix} \hat{\mathbf{I}}_{\text{ter}} \\ \hat{\mathbf{I}}_{\text{air}} \end{bmatrix}. \quad (22)$$

The combination of filtered and unfiltered measurements requires updating the functional model \mathbf{A}^G . We now name it \mathbf{A}^g , as it contains the Gaussian filter only for the airborne part

$$\mathbf{A}^g = \begin{bmatrix} \mathbf{I} & \mathbf{0} \\ \mathbf{0} & \mathbf{A}^G \end{bmatrix}. \quad (23)$$

\mathbf{A}^G is calculated according to Eq. 10 and \mathbf{I} is an identity matrix with a size that equals the number of terrestrial observations. We multiply the new functional model \mathbf{A}^g to the observations \mathbf{I} , the model observations $\hat{\mathbf{I}}$ and the covariance matrices $\mathbf{C}_{\hat{\mathbf{s}}}$ and $\mathbf{C}_{\hat{\mathbf{I}}}$. Accordingly, we obtain the RLSC formula for combined input quantities analogous to Eq. 18

$$\mathbf{s} = \mathbf{C}_{\hat{\mathbf{s}}} (\mathbf{A}^g)^T \left(\mathbf{C}_{\parallel}^g + \mathbf{A}^g \mathbf{C}_{\hat{\mathbf{I}}} (\mathbf{A}^g)^T \right)^{-1} \left(\mathbf{A}^g \mathbf{I} - \mathbf{A}^g \hat{\mathbf{I}} \right) + \hat{\mathbf{s}}. \quad (24)$$

In this form, the covariance matrix \mathbf{C}_{\parallel}^g defines the input observation accuracy. It is set up as a combination of an unfiltered terrestrial covariance matrix $\mathbf{C}_{\text{ter,ter}}$ and a filtered airborne covariance matrix $\mathbf{C}_{\text{air,air}}^G$

$$\mathbf{C}_{\parallel}^g = \begin{bmatrix} \mathbf{C}_{\text{ter,ter}} & \mathbf{0} \\ \mathbf{0} & \mathbf{C}_{\text{air,air}}^G \end{bmatrix}, \quad (25)$$

since the observation noise is not correlated between airborne and terrestrial measurements. The terrestrial part simplifies to $(\sigma_{\text{ter}}^2 \mathbf{I})$ in case the observations are uncorrelated and of equal accuracy. Thereby, σ_{ter}^2 is the variance of the terrestrial observations. The variance $\sigma_1^G \circ \sigma_1^G$ of the airborne observations is defined as main diagonal of \mathbf{C}_{\parallel}^G (Eq. 19). In the case they are of equal accuracy, $\sigma_1^G \circ \sigma_1^G$ can be replaced by the scalar values σ_{air}^2 as simplified variance of the airborne observations.

Analogous to Eq. 24, we derive the stochastic model for a combination of filtered and unfiltered observations. The error covariance matrix \mathbf{E}_{ss} of the output \mathbf{s} is based on the standard formula by Willberg et al. (2019)

$$\mathbf{E}_{\text{ss}} = \mathbf{C}_{\hat{\text{s}}\hat{\text{s}}} - \mathbf{C}_{\hat{\text{s}}\hat{\text{f}}} (\mathbf{A}^g)^T \left(\mathbf{C}_{\parallel}^g + \mathbf{A}^g \mathbf{C}_{\parallel}^G (\mathbf{A}^g)^T \right)^{-1} \mathbf{A}^g (\mathbf{C}_{\hat{\text{s}}\hat{\text{f}}})^T. \tag{26}$$

Therein, $\mathbf{C}_{\hat{\text{s}}\hat{\text{s}}}$ is the error covariance function for the model observations, which stays unfiltered as it refers only to the output functional.

4 Data and calculation

From Sect. 2, we conclude that the airborne gravity observations have to be low-pass-filtered in along-track direction. In Sect. 3 we derive a suitable concept to do so. Originally, there were 283,716 airborne gravity observations from the GRAV-D block MS05. They were corrected for their individual line biases and provided with a uniform sampling rate of 1 Hz. We chose a Gaussian low-pass filter with a HWHM of 3 km for its good compromise between removing noise and keeping gravity signal. Fig. 3 demonstrates that this HWHM removes approximately 90% of the noise above SH degree 5400. Additionally, Fig. 1 shows that the resulting frequencies in the filtered airborne observations are similar to the modeled observations.

A consequence of the low-pass filter is the very high correlation between consecutive observations (Fig. 4), which allows a significant reduction of the sampling frequency. However, this reduction is another benefit-risk assessment: a strong downsampling increases the numerical efficiency, but could also result in a loss of signal information. We exemplarily show this in Table 1 for five different sampling frequencies and three different filter lengths (given in HWHM). The table gives the mean error in mGal when all 283,716 filtered observations are reproduced from the downsampled observations with a simple spline interpolation. We interpret this value as a quality criterion for the signal loss due to the low-pass filter. Considering that the maximum error of a specific observation can be much higher than the average value,

Table 1 Overview of the benefit–risk assessment between HWHM and sampling frequency

Sampling HWHM \	1 Hz	1/8 Hz	1/16 Hz	1/32 Hz	1/64 Hz
1 km	singularity	bad κ	0,03	0,18	0,37
2 km	singularity	singularity	bad κ	0,05	0,22
3 km	singularity	singularity	singularity	0,02	0,14

Colored values are classified by their average signal loss [mGal], which indicates the ability to restore the filtered but non-downsampled signal again. Additionally, combinations are marked which result in covariance matrices with an especially high condition numbers ('bad κ ') or even numerical 'singularity'

we want to keep the average error well below 0.1 mGal. Furthermore, we mark combinations which are not feasible due to a very high condition number κ for the covariance matrix \mathbf{C}_{\parallel}^G respectively with 'bad κ ' or numerical 'singularity'. While for a higher sampling frequency or a larger filter length the condition number κ of the covariance matrix \mathbf{C}_{\parallel}^G increases, a smaller sampling frequency or shorter filter length increases the signal loss.

We conclude, that first, downsampling is needed in any case to prevent a numerical singular covariance matrix \mathbf{C}_{\parallel}^G . Secondly, the sampling frequency of 1/32 Hz is the best compromise for a HWHM of 3 km in the target area. Note that this sampling frequency is a main driver for the final filter characteristics. Together with the flight velocity, it defines the SH degree μ above which we assume mainly noise in the airborne observations (Fig. 3). By reducing the sampling frequency to 1/32 Hz, we result in a total number of 8976 filtered airborne observations. Thereby, two adjacent observations have an average distance of 3.4 km in along-track direction. The actual distance or spatial sampling, however, depends on the flight velocity of the aircraft and varies significantly in the target area. In general, the aircraft have been slowest in the mountainous areas of MS05 so that the shortest point distances are in those areas where it is most beneficial. Otherwise, we could have included a different downsampling method which we tested as well: it provides a constant spatial sampling and therefore results in a varying sampling frequency. However, in this case the filter method would model space-correlated noise in the airborne observations. Since the airborne gravity observation noise is mainly time-correlated instead, our method with constant sampling frequency stays preferable.

The 59,303 terrestrial observations are distributed in the area between longitude [35° to 40°] and latitude [− 110° to − 102°]. Their distribution is presented in Fig. 5 together with GSVS17, the area of the output grid and the borders of the surrounding states: Colorado (CO), New Mexico (NM), Utah (UT), Arizona (AZ), Oklahoma (OK) and Texas (TX). The database contains some duplicate point values which are deleted in order to prevent inconsistencies. All in all, there

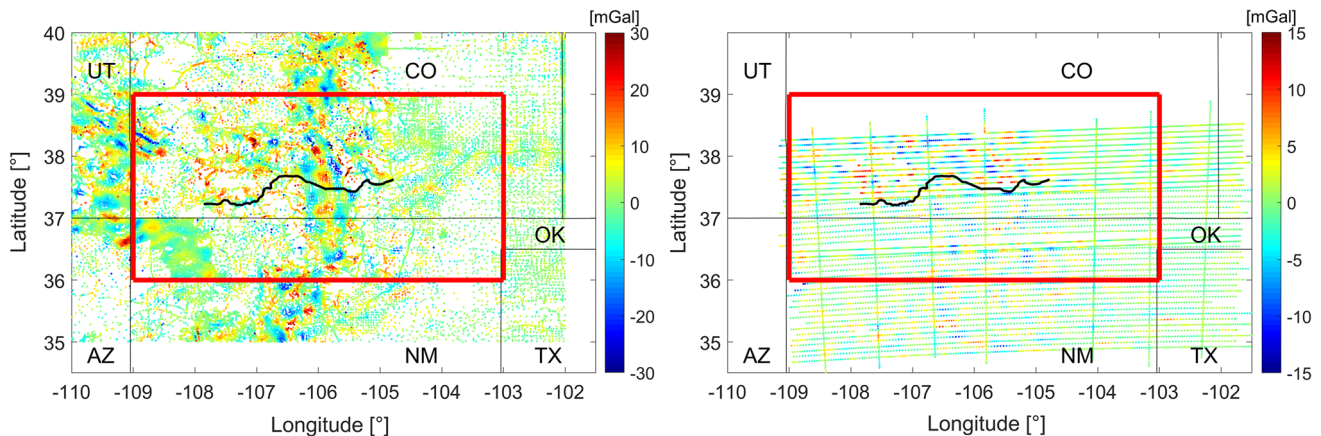


Fig. 5 Input residuals of RLSC: reduced gravity disturbances for **a** the terrestrial observations and **b** the airborne observations. The observations are removed by the XGM2018 model and the topographic gravity potential. The extent of the output grid is marked by a red box and GSVS17 by a black line

are densely measured regions in the target area, but also some observation gaps. The quality of the terrestrial observations is not well-defined as there is almost no metadata available. However, some additional information about the terrestrial data set can be found in Wang et al. ((2020), this issue). The topographic heights of the output area grid (red box in Fig. 5) are visualized in Fig. 6.

In RLSC we include an a priori assumption for the accuracy of the observations (Eq. 25 or Willberg et al. 2019) which is basically unknown for both the terrestrial and the airborne observations. GRAV-D Team (2018a) contains an error analysis for the airborne measurements, but we do not think it can give us reliable accuracies for the following reasons: (1) the derivation of the error is based on observations from different flight heights. Therefore, all values are continued to a mean height by standard free-air correction (GRAV-D Team 2017) which introduces assumptions and errors. (2) The quality assessment in GRAV-D Team (2018a) still contains the high-frequency noise which was reduced in Sect. 3. Lastly, (3) the crossover statistics cannot describe the overall accuracy accurately (GRAV-D Team 2018a), as they only assess measurement errors in the data lines (in our case: east-west), not the crossover lines (north-south).

For the filtered airborne observations we assume a uniform standard deviation of $\sigma_{\text{air}} = 1$ mGal, which seems reasonable according to Schwarz and Wei (1995), Childers et al. (1999), Novák et al. (2003) and Lu et al. (2017). While the airborne observations are well-distributed, terrestrial observations in general benefit from measuring the full gravity frequency spectrum on the Earth's surface. Therefore, we prefer a RLSC combination where both airborne and terrestrial observations have a similar influence on the overall result. In our case, this can be achieved by a uniform standard deviation of $\sigma_{\text{ter}} = 3$ mGal for the terrestrial observations, since their number is significantly higher, and they do not include corre-

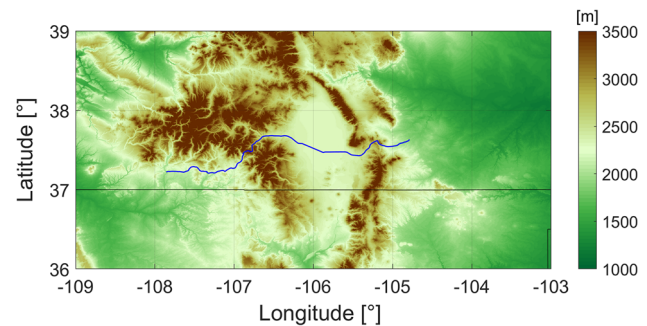


Fig. 6 Topographic heights in the area of the output grid and the location of GSVS17 in blue

lations or a downward continuation. At the present stage, our a priori accuracies are partly based on default values for the appropriate observation method. However, we verify these values with comparisons in Sect. 5.

A remove–compute–restore procedure is essential for RLSC and explained in detail in Willberg et al. (2019). In it, we include XGM2018 as high-resolution GGM to its maximum SH degree 760. The topographic gravitational potential model $dV_ELL_Earth2014$, or the ERTM2160 gravity model (Hirt et al. 2014) are added, respectively, in the frequencies above. Following aspects should be noted regarding the remove–compute–restore procedure:

- (1) Although, the maximum SH degree of XGM2018 is 760, its actual spectral resolution is defined by the maximum degree in spherical harmonics, which is 719. The same effect is visible in $dV_ELL_Earth2014$ where the maximum SH degree is 5480, but 5400 in spherical harmonics, respectively. For simplicity, we stick to the models actual spectral resolution, and as of now the corresponding SH degrees refer to spherical harmonics.

- (2) Furthermore, the reduction models for terrestrial and airborne data are not identical in our case. ERTM2160 is given in an approximately 250 m resolution grid format, therefore providing the very high-resolution information which we need for the reduction of terrestrial data on the Earth’s surface. However, $dV_ELL_Earth2014$ is calculated from SH synthesis which can be used for arbitrary point positions (e.g., airborne observations). In this case, the different reduction steps are justified as $dV_ELL_Earth2014$ and ERTM2160 are both calculated from the SRTM v4.1 topography model by Jarvis et al. (2008) in the target area. Accordingly, they contain identical signal information in the respective SH degrees.
- (3) Lastly, $dV_ELL_Earth2014$ and ERTM2160 are based on simplified density assumptions and cannot reflect lateral density variations. Deviations of the real density from these model assumptions are reflected in the residual input signals of RLSC. Accordingly, they are consistently collocated to the output quantities. This issue is not specific for the present RLSC method, but holds generally for all regional gravity field modeling methods that are using the RCR technique. Yang et al. (2018) demonstrate that the use of available lateral density maps does not necessarily improve the gravity modeling results.

The reduced gravity disturbances $\Delta \delta g$ which enter RLSC are presented in Fig. 5 and described in the following. For the terrestrial observations (Fig. 5a), we calculate from Eq. 13

$$\begin{aligned} \Delta \mathbf{g}_{\text{ter}} &= \mathbf{l}_{\text{ter}} - \hat{\mathbf{l}}_{\text{ter}} \\ &= \mathbf{g}_{\text{ter}} - \hat{\mathbf{g}}_{\text{ter}}(\text{XGM2018}) \\ &\quad - \hat{\mathbf{g}}_{\text{ter}}(dV_ELL_Earth2014) - \hat{\mathbf{g}}_{\text{ter}}(\text{ERTM2160}), \end{aligned} \tag{27}$$

with the SH degrees $n^{\text{XGM2018}} \in \{2, 719\}$ and $n^{dV_ELL_Earth2014} \in \{720, 2159\}$. ERTM2160 is applied from SH degree 2160 to its maximum resolution, which equals approximately 250 m. Correspondingly, we have for the airborne observations (Fig. 5b)

$$\begin{aligned} \Delta \mathbf{g}_{\text{air}}^G &= \mathbf{l}_{\text{air}}^G - \hat{\mathbf{l}}_{\text{air}}^G \\ &= \mathbf{g}_{\text{air}}^G - \hat{\mathbf{g}}_{\text{air}}^G(\text{XGM2018}) - \hat{\mathbf{g}}_{\text{air}}^G(dV_ELL_Earth2014), \end{aligned} \tag{28}$$

with $n^{\text{XGM2018}} \in \{2, 719\}$ and $n^{dV_ELL_Earth2014} \in \{720, 5400\}$. The reduction to different SH degrees is valid in our case since the gravity signal above SH degree 5400 is negligible at the position of the airborne observations. This is first due to signal attenuation with altitude, which significantly reduces the high-frequency gravity signal at flight height. Secondly, the low-pass filter removes approximately 90% of

the still remaining signal above SH degree 5400 (compare to Fig. 3).

In Eqs. 27 and 28 we apply globally unbiased models to a very high degree. Accordingly, we can safely assume that they do not have a significant bias in our study area, which is a requirement for calculating the height anomaly output $\Delta \zeta_{\text{out}}$ of RLSC (Eq. 13). The final height anomalies ζ_{out} are calculated by restoring the effect of the corresponding models (XGM2018, $dV_ELL_Earth2014$ and ERTM2160)

$$\begin{aligned} \zeta_{\text{out}} &= \Delta \mathbf{s}_{\text{out}} + \hat{\mathbf{s}}_{\text{out}} \\ &= \Delta \zeta_{\text{out}} + \hat{\zeta}_{\text{out}}(\text{XGM2018}) \\ &\quad + \hat{\zeta}_{\text{out}}(dV_ELL_Earth2014) + \hat{\zeta}_{\text{out}}(\text{ERTM2160}), \end{aligned} \tag{29}$$

with exactly the same SH degrees as in the terrestrial reduction. The subscript ‘out’ refers to specified output points on the Earth’s surface which are a combination of a regular $1' \times 1'$ grid and the GSVS17 points. The topographic heights of the output area are presented in Fig. 6, whereby the highest mountains reach more than 4000 m. The location of GSVS17, a west-east traverse of approximately 350 km through the mountains of Colorado, is added in blue. Note that the location of the grid is centered within the area of terrestrial observations, but significantly shifted in relation to the airborne observations (Fig. 5).

In the RLSC approach, we include the original full covariance information of XGM2018. The SH coefficients of XGM2018 and XGM2016 are very similar, but the corresponding covariance information of XGM2018 has been improved and is even more realistic now. The covariance matrices $\mathbf{C}_{\hat{\mathbf{l}}}$, $\mathbf{C}_{\hat{\mathbf{s}}}$ and $\mathbf{C}_{\hat{\mathbf{s}}\hat{\mathbf{s}}}$ of the reduction model (Eqs. 24, 26) are calculated from a model covariance function (MCF) that fits the reduced gravity disturbance input (Fig. 5). The approach is explained and justified in detail by Willberg et al. (2019).

We present our result in agreement with the reference potential value W_0 of the IHRS definition (Ihde et al. 2017) in the mean-tide system. Since output points within the JWG are specified on the Earth’s surface, we include the theory of Molodensky (Hofmann-Wellenhof and Moritz 2006) and prefer the calculation of height anomalies instead of geoid heights. Comparisons of the absolute potential values and geoid heights, which are also calculated within the JWG, are not discussed here, but presented in Sánchez et al. ((2020), this issue) and Wang et al. ((2020), this issue). However, we also include the calculation of gravity disturbances at the input positions (with a corresponding restore step) in order to compare them to the original measurements in Sect. 5.

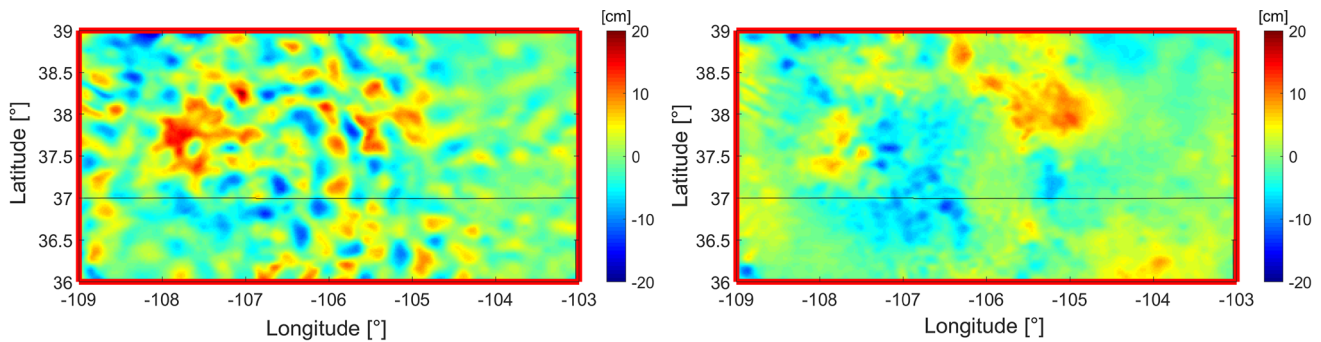


Fig. 7 Comparison of RLSC result against available models. **a** the height anomaly $\Delta \zeta_{\text{out}}$. **b** Difference to EGM2008 [$\zeta_{\text{out}} - \hat{\zeta}_{\text{out}}(\text{ERTM2160}) - \hat{\zeta}_{\text{out}}(\text{EGM2008})$]

5 Analysis of the RLSC grid

In this and the following section, we present and quantify our height anomaly result ζ_{out} (Eq. 29) related to ‘the 1 cm geoid experiment’. We refer to Wang et al. ((2020), this issue) for general conclusions and further results from the JWG. The high-resolution measurements along GSVS17 have not been published yet, therefore we include internal and external validation to verify our results. At first, in Fig. 7, we compare our result against available models to indicate main effects in the result. Fig. 7a shows the height anomaly $\Delta \zeta_{\text{out}}$ from RLSC (without restore step), which gives the improvement from the gravity measurements with respect to the prior models. As expected, we see a high correlation between the output residuals $\Delta \zeta_{\text{out}}$ and the input residuals in Fig. 5. The dominating effects are signals with a spatial extent of approximately 0.1° to 0.3° which corresponds to SH degrees between 720 and 2160. In these frequencies, the reduction model consists only of topography-derived gravity information. Thus, we assume that the signals in Fig. 7a are significant improvements due to the input gravity measurements. However, there is also one maximum on the left-hand side with a much larger spatial extent. The terrestrial input residuals (Fig. 5a) especially show a positive bias in this area which seems to be responsible for this maximum. The spatial extent of the red area in Fig. 7a indicates that XGM2018 and the terrestrial gravity observations are not consistent in this area.

Figure 7b presents the difference between the height anomaly result ζ_{out} and the corresponding height anomaly derived from EGM2008 (Pavlis et al. 2012). However, in this comparison we do not restore $\hat{\zeta}_{\text{out}}(\text{ERTM2160})$ in Eq. 29, because the resolution of ERTM2160 is not included in EGM2008. The presented difference is dominated by features with a spatial extent in the order of 100 km and can be attributed to the difference between EGM2008 and our three data sources: XGM2018, the terrestrial, and airborne gravity observations. Note that the dominating effects from Fig. 7a are not visible in Fig. 7b. We therefore conclude that EGM2008 represents the gravity field between

SH degree 720 and 2160 significantly better than the mere topographic gravitational model $dV_{\text{ELL_Earth2014}}$.

In a second step, we calculate gravity disturbances for the input points of RLSC and compare them to the original observations. We refer to the appropriate difference as output residuals, whereby their presentation in Fig. 8 is limited to the area of the output grid. The output residuals indicate the improvement of the combined RLSC solution with respect to the original gravity measurements. For the terrestrial output residuals in Fig. 8a, we see significant differences in the target area: In areas with topographic heights below 2500 m, e.g., east of -105° longitude or in the south–west corner, the output residuals are close to 0 mGal. In the mountainous areas of Colorado they often exceed ± 5 mGal. It is common for LSC methods to smooth the input gravity observations in regions with strongly varying gravity signals (e.g., mountains). In our case, this is the result of a homogeneous and isotropic covariance function above the maximum resolution of XGM2018, which consequently leads to high output residuals. However, the very inhomogeneous parts in Fig. 8a indicate that at least some of the output residuals are outliers or measurement errors in the gravity database.

At this point, we do not detect or exclude outliers in RLSC, as there is no beneficial metadata. Furthermore, individual data point selections will inevitably complicate the comparisons with other groups from ‘the 1 cm geoid experiment’. However, we acknowledge that an additional, individual data point inspection and corresponding outlier detection could be able to improve the final results. Once more, the area with an offset to XGM2018 stands out in the center of the mid left side, where a large area is dominated by positive output residuals and warm colors. Apparently, RLSC combines the differing data sets XGM2018 and terrestrial observations, thus resulting in residuals to XGM2018 (visible in Fig. 7) and to the terrestrial gravity observations, respectively (visible in Fig. 8). We see a possible reason for the bias in the inhomogeneous distribution of the terrestrial observations which are more often located in mountain valleys. The standard deviation of all terrestrial output residuals is 2.3 mGal,

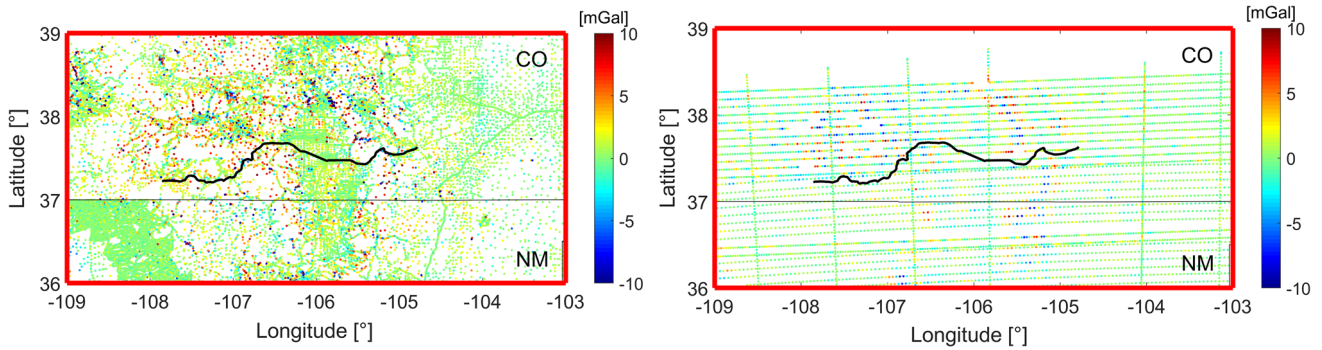


Fig. 8 Output residuals in terms of gravity disturbance, namely original observations—RLSC result for **a** the terrestrial gravity observations and **b** the airborne gravity observations

and its mean value is 0.3 mGal. The output residuals for the airborne gravity observations, in terms of the original observations, have a standard deviation of 1.6 mGal with a mean value of -0.1 mGal (Fig. 8b). The dominating effects are again short-wavelength effects in the mountainous regions of Colorado, once again affected from the smoothing effect of LSC. However, this time the output residuals are affected from the included low-pass filter as well. Furthermore, differences between terrestrial and airborne gravity observations are assumed to be a main contributor for the output residuals in Fig. 8. As there are no long wavelength signals visible in Fig. 8b, we conclude that XGM2018 and airborne gravity observations are consistent in the target area.

The residual’s standard deviations confirm that the scale of our a priori observation accuracy, $\sigma_{\text{ter}} = 3$ mGal and $\sigma_{\text{air}} = 1$ mGal respectively, are generally reasonable. However, the data sets seem to show a spectral dependence, as indicated by much higher residuals in the Colorado mountains. As a result of the equally weighted observation accuracies for a single data type, RLSC produces output accuracies depending on the data distribution and a priori accuracies only. Accordingly, the estimated accuracies cannot adequately represent the problems of suspicious areas that we see from the residuals.

Figure 9 shows the resulting 3σ confidence level for height anomalies in the target area which is derived from the error covariance matrix \mathbf{E}_{ss} in Eq. 26. The values depend on the accuracy assumptions for the gravity observations, their point distribution and the covariance information of XGM2018. The 3σ confidence level varies from approximately 1 cm in areas with very dense terrestrial observations to more than 5 cm in the very north where the solution is not supported by airborne observations (cf. Fig. 5). The availability of accuracy estimates is a main advantage of LSC approaches. However, in this case an iterative RLSC approach would be necessary to derive more realistic output accuracies. For example, we could use the residuals in Fig. 8 to derive individual input

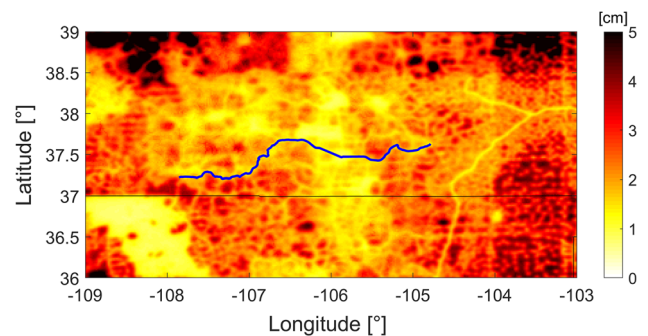


Fig. 9 3σ confidence level from RLSC for the height anomaly in the target area. GSVS17 is included with blue color

accuracies depending on the consistency of terrestrial and airborne data.

In summary, the terrestrial gravity observations show notable differences to XGM2018 and airborne gravity observations in the highly mountainous regions of Colorado, but a generally good consistency everywhere else. We assume that the height anomaly result ζ_{out} could be further improved by an outlier detection, or far-reaching data inspection in general. Additionally, an iterative RLSC approach could derive accuracy assumptions from the output residuals. This would result in a more selective weighting between the data sets and an improved accuracy estimation in general. However, we see these aspects as beyond the scope of this paper. Our focus is, first, on the derivation of a consistent methodology for low-pass filtering within RLSC, and second on the generation of a comparable result within ‘the 1 cm geoid experiment’.

6 Comparison along GSVS17

The height anomalies along GSVS17 have been computed by 13 different groups and are presented with different colors in Fig. 10a. The values at the 223 benchmarks are given as difference to the joint mean value of each individual point. As long as the real reference values along GSVS17 are not yet

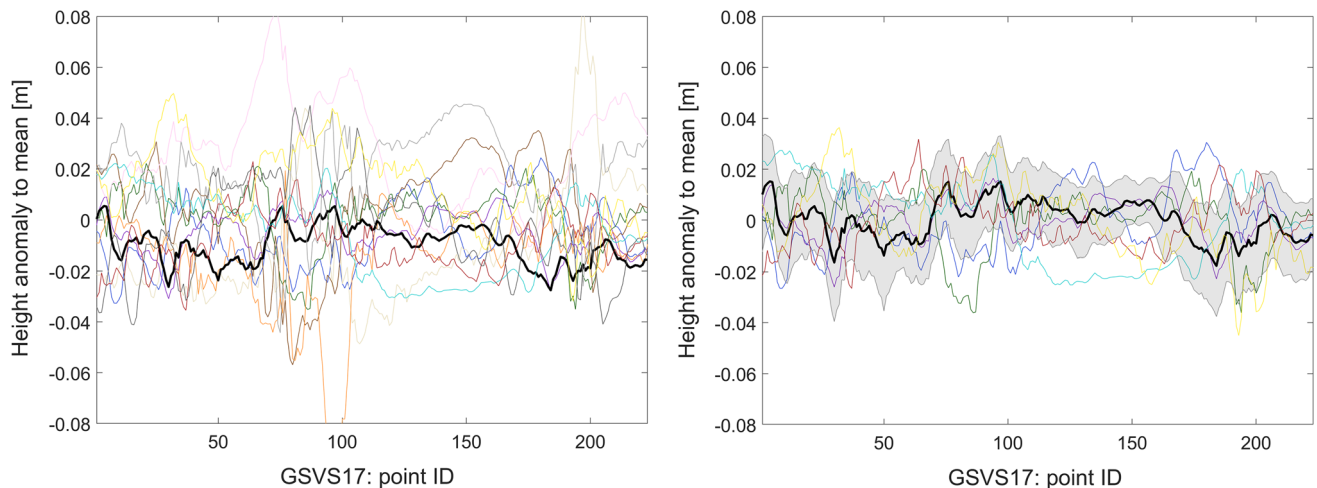


Fig. 10 Comparison of different height anomaly results as difference to the joint mean value along GSVS17. **a** Among all submissions within the JWG, our result (black) includes the smallest variations. **b** 7 selected

submissions with an individually corrected mean value, whereby our estimated confidence interval is additionally shown in gray color

available, we assume that the mean value of 13 independent calculation methods is significantly better than an individual solution. This notion is, for example, used analogously in meteorological literature (Evans et al. 2000; Ebert 2001). Therefore, we interpret the common mean value as a reference which is represented by zero in Fig. 10. However, it should be noted that this mean value is not necessarily without systematic effects, as they could be introduced by the input gravity observations, and thus reflected in all solutions. During several phases of the JWG the offset between different solutions was reduced (Wang et al. (2020), this issue), mainly by the adaptation of common standards, e.g., zero-degree term and tide system. The remaining difference in the mean value might result from differences in the processing strategies, the topographic reduction or the individual data handling, and cannot be solved by this paper. At the present stage, the absolute mean offsets of the different curves in Fig. 10a range from 0.1 to 2.7 cm, and the standard deviations from 7.5 to 2.4 cm. Our solution, which is highlighted by a black color, has a mean value of -1.0 cm, and with 7.5 mm the lowest standard deviation among all results. As a result, the variations in our solution are significantly reduced in comparison to most others (Fig. 10a).

In Fig. 10b, the remaining issue of the mean offset between different height anomaly solutions is ignored and individually corrected. Furthermore, we selected only seven out of the 13 solutions which are most consistent to the previously introduced mean value. Our height anomaly result (black line) is the only solution that varies only within ± 2 cm in relation to the joint mean value. The estimated 3σ confidence interval of our solution is additionally overlaid with gray color. We conclude that several of the other results are mainly

covered within this confidence level, in spite of the fact that our provided standard deviation is probably too optimistic in the mountainous parts of Colorado (see Sect. 5). Even when we reduce a mean offset and consider only the solutions in Fig. 10b, there are remaining variations of some centimeters between the different height anomaly results. Note that similar approaches might benefit from the comparison to a mean value as they are more likely to end up close together. However, our approach is the only RLSC approach, and the only one-step LSC method among the contributing groups.

One of the main reason for the remaining variations in Fig. 10 are the differences between terrestrial and airborne observations in the area. In order to quantify the spread resulting from different weighting between terrestrial and airborne observations, a series of additional test computations have been performed. In Fig. 11, the black line is again our height anomaly result ζ_{out} in reference to the mean, while other curves represent alternative solutions. We exemplary include the following four cases: (1) using only terrestrial observations and disregarding airborne data in blue, (2) using only airborne observations in red, (3) using a different airborne input accuracy in green, and (4) a solution without low-pass filter of airborne data in purple. In general, significant differences show up, especially between the terrestrial-only and the airborne-only result. In an extreme case (around point ID 110) two airborne flight lines are positioned above two opposing mountain flanks, while GSVS17 runs through the in-between valley with a distance of approximately 5 km to both of the flight lines. As a result, the two corresponding solutions differ by more than 8 cm, obviously measuring a different gravity signal. We conclude from the height anomaly results shown in Fig. 11 that rather large differ-

ences of several centimeters can be caused by the weighting of the individual data sets.

As an example, the green curve in Fig. 11 is calculated equally to the black one, but uses a different input accuracy for the airborne observations, namely $\sigma_{\text{air}} = 1.5$ mGal instead of 1 mGal. As a result, RLSC gives a lower relative weight to the airborne observations, which leads to a shift of the combined solution towards the terrestrial-only solution. An opposite effect is visible for the purple curve. It is a combined solution that includes unfiltered airborne observations with an 8 Hz sampling frequency and an accuracy assumption of $\sigma_{\text{air}} = 2$ mGal since the high-frequency noise is still included. The significantly increased number of airborne observations, and the fact that they are assumed to be uncorrelated, amplifies their relative weight in RLSC. Accordingly, this solution is shifted towards the airborne-only solution (red curve). This could be an indication that one of the main reasons for the height anomaly differences in Fig. 10a is the various treatment of terrestrial and airborne input data. Therefore, it is not only related to the different regional gravity modeling approaches used in this inter-comparison exercise.

In summary, our height anomaly ζ_{out} performs very well in a comparison among the JWG results and shows the smallest variations in regard to the joint mean value. We highlight differences in the available data sources, and conclude that their relative weighting will be one of the main drivers of the final performance. However, we emphasize that all data issues mentioned in ‘the 1 cm geoid experiment’ are not a problem of our gravity modeling approach, but rather mere inconsistencies in the available data sources. In order to solve these issues, a detailed data inspection of the original data sources would have to be done, which would go far beyond the scope of this study. However, solving some of the data issues could become easier once the high-quality observations from the GSVS17 project are released. At the present stage, we conclude that different scenarios of RLSC show consistent results in a simple comparison along the GSVS line. Furthermore, we demonstrate that our method provides the necessary flexibility for an adjustment in case a data set provides either benefits or problems in a target area.

7 Conclusion and outlook

In this paper, we use a low-pass filter for reducing high-frequency noise in airborne gravity observations from the GRAV-D project. Accordingly, we derive a novel concept in order to include the resulting correlations to regional gravity field modeling. In RLSC, the functional and stochastic model is adapted, whereby filtered observations and filtered covariance matrices are treated in a consistent manner. The approach is verified with a combination of filtered (airborne)

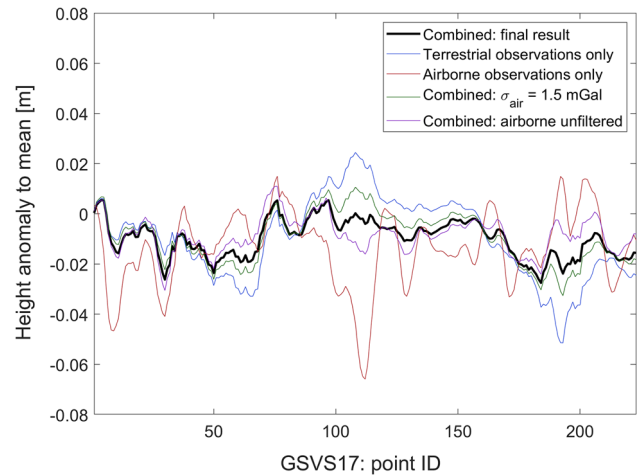


Fig. 11 Comparison of different internal height anomaly results along GSVS17. Solutions vary according to their relative weighting between terrestrial and airborne observation, and show differences of up to 8 cm

and unfiltered (terrestrial) observations in the frame of ‘the 1 cm geoid experiment’.

In the target area of Colorado, our calculated height anomaly grid displays significant improvements compared to already existing gravity models. They are visible as long wavelength differences to the EGM2008, and short to medium-wavelength deviations from the a priori topographic gravity model. The calculated output residuals for the gravity disturbance indicate a very good consistency of terrestrial and airborne data in areas with topographic heights below 2500 m, but reveal some issues in the highly mountainous regions of the Rocky Mountains. We even identified one region where the terrestrial observations differ significantly from the long wavelength part of XGM2018.

Within ‘the 1 cm geoid experiment’ the RLSC method performs very well in a comparison among 13 independent height anomaly results along the GSVS17 benchmarks. Since the actual results of GSVS17 are not yet available, the reference value which is used to evaluate the performance of our solution, is calculated from a common mean value. In general, the final height anomaly results deviate from the reference by a few centimeters. With a standard deviation of only 7.5 mm our solution shows the smallest variations with respect to the reference. Furthermore, it is the only result that always stays within ± 2 cm (in case the individual offsets are reduced).

Moreover, we analyzed the impact of the systematic differences between the available data sources on the final result. In a comparison along GSVS17, we tested four further data and processing scenarios, and could show that the relative weighting among the input data types can cause differences in the order of several centimeters in the height anomaly results. Consequently, RLSC can be individually adapted in

the case that there is additional information about the quality of the gravity observations. More generally, we conclude that a significant part of the differences in ‘the 1 cm geoid experiment’ might be related to a different treatment and relative weighting of the input data, and not only to various regional gravity field modeling methods. In this regard, it might be useful to check the internal weighting between our data sets again, as soon as the high-quality measurements along GSVS17 are available to the public.

One of the main advantages of the statistical method of (R)LSC is that it also provides variance–covariance information of the resulting quantities. The availability of realistic error estimates will be crucial for the realization of the IHRS. Due to restricted availability and heterogeneous quality of ground gravity data, it is to be expected that a similar accuracy of absolute potential values at the IHRS stations cannot be achieved. In this case, the provision of realistic error estimates in addition to the potential values themselves will be very important. The estimated standard deviations of height anomalies are, in our current solution, mainly dominated by the distribution of the gravity observations as well as the relative weighting of the input data sets. However, a constant weight of the two data sets, terrestrial and airborne observations, has been included. In an iterative RLSC approach, the post-fit residuals could be used to modify the a priori accuracy of the input data, and thus the relative weighting scheme. By this, the identified systematic differences between terrestrial and airborne data in certain areas could also be taken into account. Consequently, this would result in an even more realistic stochastic modeling and further improved error estimates for the output quantities. Since the main goal was to inter-compare the results with other study teams, this has not been applied in the present solution but will be part of further studies.

Summarizing, ‘the 1 cm geoid experiment’ helps for the scheduled IHRS definition and realization because it provides a meaningful accuracy benchmark in the case of a good data distribution in very difficult terrain. Within this JWG all contributing groups have proven their capability to calculate the height anomaly with an accuracy of some centimeters. In the end, IHRS should be defined by absolute potential values, but their derivation from the disturbing potential T , which is also needed for the height anomaly, is straightforward. Sánchez et al. ((2020), this issue) propose a globally distributed computation of potential values at IHRS reference stations due to common data restrictions. Thereby, for example, all institutions with a specific performance in terms of a reference could be allowed to contribute to the calculation of IHRS stations with their own method. Consequently, it will be extremely important to analyze, how much of the remaining deviations are caused by differences in the regional gravity modeling methods, and how much by the different treatment and relative weighting of input data.

The benefit of including covariance information from high-resolution GGMs in RLSC and the resulting advantage in terms of the calculation of IHRS reference stations is already explained in Willberg et al. (2019). With the consistent handling of airborne gravity data and by including a covariance propagation of the filter behavior, we can further enhance the stochastic modeling, which, as discussed above, will be very beneficial for the IHRS realization.

Acknowledgements Open Access funding provided by Projekt DEAL. A large part of the investigations presented in this paper was conducted in the framework of the project ‘Optimally combined regional geoid models for the realization of height systems in developing countries’ funded by the German Research Foundation (DFG project no. PA 1543/14-1). We also acknowledge the provision of computer resources by the Leibniz Supercomputing Centre (LRZ; Address: Boltzmannstrasse 1, 85748 Garching, Germany).

Author contributions MW designed the study. MW and PZ developed the theoretical formalism. MW performed the calculations and created the figures. MW wrote the manuscript with support of RP. All authors discussed the content of the final manuscript.

Data Availability Statement The data sets analyzed in this study are available within the IAG working group ‘the 1 cm geoid experiment’ and its availability is specified by a summary paper of this joint issue (Wang et al. (2020), this issue). The original airborne gravity data is available online (GRAV-D Team 2018b). The model coefficients of XGM2018 and the corresponding covariance information can be provided on request.

Open Access This article is licensed under a Creative Commons Attribution 4.0 International License, which permits use, sharing, adaptation, distribution and reproduction in any medium or format, as long as you give appropriate credit to the original author(s) and the source, provide a link to the Creative Commons licence, and indicate if changes were made. The images or other third party material in this article are included in the article’s Creative Commons licence, unless indicated otherwise in a credit line to the material. If material is not included in the article’s Creative Commons licence and your intended use is not permitted by statutory regulation or exceeds the permitted use, you will need to obtain permission directly from the copyright holder. To view a copy of this licence, visit <http://creativecommons.org/licenses/by/4.0/>.

References

- Arabelos DN, Tscherning CC (2009) Error-covariances of the estimates of spherical harmonic coefficients computed by LSC, using second-order radial derivative functionals associated with realistic GOCE orbits. *J Geod* 83(5):419–430. <https://doi.org/10.1007/s00190-008-0250-9>
- Becker D (2016) Advanced Calibration Methods for Strapdown Airborne Gravimetry. Dissertation, Technische Universität Darmstadt
- Childers VA, Bell RE, Brozena JM (1999) Airborne gravimetry: an investigation of filtering. *Geophysics* 64(1):61–69. <https://doi.org/10.1190/1.1444530>
- Ebert EE (2001) Ability of a poor man’s ensemble to predict the probability and distribution of precipitation. *Mon Wea Rev* 129:2461–2480. [https://doi.org/10.1175/1520-0493\(2001\)129<2461:AOAPMS>2.0.CO;2](https://doi.org/10.1175/1520-0493(2001)129<2461:AOAPMS>2.0.CO;2)

- Evans RE, Harrison MSJ, Graham RJ, Mylne KR (2000) Joint medium-range ensembles from the Met. Office and ECMWF systems. *Mon Wea Rev* 128:3104–3127. [https://doi.org/10.1175/1520-0493\(2000\)128<3104:JMREFT>2.0.CO;2](https://doi.org/10.1175/1520-0493(2000)128<3104:JMREFT>2.0.CO;2)
- Forsberg R, Olesen AV, Bastos L, Gidskehaug A, Meyer U, Timmen L (2000) Airborne geoid determination. *Earth Planets Space* 52:863–866. <https://doi.org/10.1186/BF03352296>
- Forsberg R, Olesen AV, Einarsson I, Manandhar N, Shreshta K (2014) Geoid of Nepal from airborne gravity survey. In: Rizos C, Willis P (eds) *Earth on the edge: science for a sustainable planet*. International association of geodesy symposia, 139, Springer, Berlin. https://doi.org/10.1007/978-3-642-37222-3_69
- GRAV-D Team (2017) GRAV-D General Airborne Gravity Data User Manual. Damiani TM, Youngman M, Johnson J (eds), Version 2.1. https://www.ngs.noaa.gov/GRAV-D/data_products.shtml. Accessed 15 Oct 2019
- GRAV-D Team (2018a) Block MS05 (Mountain South 05); GRAV-D airborne gravity data user manual. Youngman M, Johnson J (eds), Version BETA#2. https://www.ngs.noaa.gov/GRAV-D/data_ms05.shtml. Accessed 15 Oct 2019
- GRAV-D Team (2018b) Gravity for the Redefinition of the American Vertical Datum (GRAV-D) Project, Airborne Gravity Data; Block MS05. https://www.ngs.noaa.gov/GRAV-D/data_ms05.shtml. Accessed 15 Oct 2019
- Harlan RB (1968) Eötvös corrections for airborne gravimetry. *J Geophys Res* 73(14):4675–4679. <https://doi.org/10.1029/JB073i014p04675>
- Hirt C, Kuhn M, Claessens SJ, Pail R, Seitz K, Gruber T (2014) Study of the Earth's short-scale gravity field using the ERTM2160 gravity model. *Comput Geosci* 73:71–80. <https://doi.org/10.1016/j.cageo.2014.09.001>
- Hirt C, Rexer M (2015) Earth 2014: 1 arc-min shape, topography, bedrock and ice-sheet models—Available as gridded data and degree-10800 spherical harmonics. *Int J Appl Earth Obs Geoinf* 39:103–112. <https://doi.org/10.1016/j.jag.2015.03.001>
- Hofmann-Wellenhof B, Moritz H (2006) *Physical Geodesy*. Springer, Wien. ISBN 10 2-211-33544-7
- Huang J, Véronneau M, Mainville A (2008) Assessment of systematic errors in the surface gravity anomalies over North America using the GRACE gravity model. *Geophys J Int* 175(1):46–54. <https://doi.org/10.1111/j.1365-246X.2008.03924.x>
- Hwang C, Hsiao Y-S, Shih H-C, Yang M, Chen K-H, Forsberg R, Olesen AV (2007) Geodetic and geophysical results from a Taiwan airborne gravity survey: data reduction and accuracy assessment. *J Geophys Res* 112(B4):B04407. <https://doi.org/10.1029/2005JB004220>
- Ihde J, Sánchez L, Barzaghi R, Drewes H, Foerste C, Gruber T, Liebsch G, Marti U, Pail R, Sideris M (2017) Definition and proposed realization of the international height reference system (IHRs). *Surv Geophys* 38(3):549–570. <https://doi.org/10.1007/s10712-017-9409-3>
- Jarvis A, Reuter HI, Nelson A, Guevara E (2008) Hole-filled SRTM for the globe v4.1. Available from the CGIAR-SXI SRTM 90m database at: <http://srtm.csi.cgiar.org>
- Jekeli C (1981) Alternative methods to smooth the Earth's gravity field. Reports of the Department of Geodetic Science, No. 327, Ohio State University, Columbus, Ohio
- Jiang T, Wang YM (2016) On the spectral combination of satellite gravity model, terrestrial and airborne gravity data for local gravimetric geoid computation. *J Geod* 90(12):1405–1418. <https://doi.org/10.1007/s00190-016-0932-7>
- LaCoste LJ (1967) Measurement of gravity at sea and in the air. *Rev Geophys* 5(4):477–526. <https://doi.org/10.1029/RG005i004p00477>
- Li X (2011) Strapdown INS/DGPS airborne gravimetry tests in the Gulf of Mexico. *J Geod* 85:597–605. <https://doi.org/10.1007/s00190-011-0462-2>
- Lu B, Barthelmes F, Petrovic S, Förste C, Flechtner F, Luo Z, He K, Li M (2017) Airborne gravimetry of GEOHALO mission: data processing and gravity field modeling. *J Geophys Res: Solid Earth* 122:10586–10604. <https://doi.org/10.1002/2017JB014425>
- Moritz H (1980) *Advanced physical geodesy*. Herbert Wichmann, Karlsruhe. ISBN 3-87907-106-3
- National Geodetic Survey (2019) Homepage at https://www.ngs.noaa.gov/GRAV-D/data_products.shtml. Accessed 15 Oct 2019
- Novák P, Kern M, Schwarz K-P, Sideris MG, Heck B, Ferguson S, Hammada Y, Wei M (2003) On geoid determination from airborne gravity. *J Geod* 76(9–10):510–522. <https://doi.org/10.1007/s00190-002-0284-3>
- Olesen AV (2003) Improved airborne scalar gravimetry for regional gravity field mapping and geoid determination. Dissertation, Faculty of Science, University of Copenhagen
- Pail R, Fecher T, Barnes D, Factor JF, Holmes SA, Gruber T, Zingerle P (2018) Short note: the experimental geopotential model XGM2016. *J Geod* 92(4):443–451. <https://doi.org/10.1007/s00190-017-1070-6>
- Pavlis NK, Holmes SA, Kenyon SC, Factor JK (2012) The development and evaluation of the Earth Gravitational Model 2008 (EGM2008). *J Geophys Res* 117:B04406. <https://doi.org/10.1029/2011JB008916>
- Rexer M, Hirt C, Claessens S, Tenzer R (2016) Layer-based modelling of the earth's gravitational potential up to 10-km scale in spherical harmonics in spherical and ellipsoidal approximation. *Surv Geophys* 37(6):1035–1074. <https://doi.org/10.1007/s10712-016-9382-2>
- Sánchez L, Ågren J, Huang J, Wang YM, Mäkinen J, Pail R, Barzaghi R, Vergos GS, Ahlgren K, Liu Q (2020) Strategy for the implementation of the international height reference system. *J Geod* (**this issue**)
- Schwarz KP, Wei M (1995) Some unsolved problems in airborne gravimetry. In: Sünkel H, Marson I (eds) *Gravity and geoid*. International association of geodesy symposia, vol 113. Springer, Berlin. https://doi.org/10.1007/978-3-642-79721-7_15
- Smith DA, Holmes SA, Li X, Guillaume S, Wang YM, Bürki B, Roman DR, Damiani TM (2013) Confirming regional 1 cm differential geoid accuracy from airborne gravimetry: the geoid slope validation survey of 2011. *J Geod* 87(10–12):885–907. <https://doi.org/10.1007/s00190-013-0653-0>
- Swain CJ (1996) Horizontal acceleration corrections in airborne gravimetry. *Geophysics* 61(1):273–276. <https://doi.org/10.1190/1.1443948>
- Wang YM et al. (2020) Report on the 1-cm geoid experiment in Colorado. *J Geod* (**this issue**)
- Wei M, Schwarz KP (1998) Flight test results from a strapdown airborne gravity system. *J Geod* 72(6):323–332. <https://doi.org/10.1007/s001900050171>
- Willberg M, Zingerle P, Pail R (2019) Residual least-squares collocation: use of covariance matrices from high-resolution global geopotential models. *J Geod* 93(9):1739–1757. <https://doi.org/10.1007/s00190-019-01279-1>
- Yang M, Hirt C, Tenzer R, Pail R (2018) Experiences with the use of mass density maps in residual gravity forward modelling. *Stud Geophys Geod* 62:660–680. <https://doi.org/10.1007/s11200-017-0656-z>
- Zhong D, Damiani TM, Preaux SAM, Kingdon R (2015) Comparison of airborne gravity processing results by GravPRO and Newton software packages. *Geophysics* 80(4):G107–G118. <https://doi.org/10.1190/geo2014-0519.1>